

2-18
m-14

HYPERSONIC RESEARCH ENGINE PROJECT - PHASE II
AEROTHERMODYNAMIC INTEGRATION
MODEL DEVELOPMENT
TENTH INTERIM TECHNICAL DATA REPORT
DATA ITEM NO. 55-4.10
10 JUNE THROUGH 9 SEPTEMBER 1970
NASA CONTRACT NO. NAS1-6666

Document No. AP-70-6800

(NASA-CR-112058) HYPERSONIC RESEARCH
ENGINE PROJECT. PHASE 2:
AEROTHERMODYNAMIC INTEGRATION L.F. Jilly
(AiResearch Mfg. Co., Los Angeles, Calif.)
15 Oct. 1970 100 p

N72-25713

CSCL 21E G3/28
Unclas
30760



AIRESEARCH MANUFACTURING COMPANY

A DIVISION OF THE GARRETT CORPORATION

9851-9951 SEPULVEDA BLVD. • LOS ANGELES, CALIFORNIA 90009

TELEPHONE: SPRING 6-1010, ORCHARD 0-0131 • CABLE: GARRETTAIR LOS ANGELES

1. SUMMARY OF STATUS

1.1 OVERALL ENGINE DESIGN

The analytical effort expended during this reporting period was directed towards (1) completing the design of the combustor exit instrumentation assembly, (2) analyzing the coolant flow distribution of the cowl leading edge tip section, (3) determining effects of purge gas pressure on AIM performance analysis, and (4) analyzing heat transfer and associated stress problems related to the cowl leading edge tip section and the nozzle shroud assembly for test conditions at the Plumbrook facility.

1.2 HARDWARE STATUS

Fabrication of the various components of the AIM unit has progressed satisfactorily with the exception of the cowl leading edge section. Completion of all the components of the AIM unit is scheduled for the early part of the next reporting period.

The estimated percentages of completion of the various components of the AIM unit are as follows:

<u>Component</u>	<u>Percent Complete</u>	
	<u>Details</u>	<u>Subassembly</u>
Spike assembly	90	60
Inner shell	100	95
Nozzle plug	100	98
Cowl leading edge	90	75
Outer shell	90	50
Nozzle shroud	95	90
Outer cowl body	90	65

1.3 TESTS

1.3.1 Cowl Leading Edge Flow Test

Flow testing of the cowl leading edge tip section was performed. The tests have indicated that the pressure drop across the tip is much higher than anticipated, and hence the coolant-bypass orifice configuration must be modified to achieve the desired pressure drop.



1.3.2 Metal Joining Evaluation

A supplemental test program was undertaken to evaluate problems encountered in E-B welding Nickel-200 to itself and to other metals. Weld specimens were fabricated and subjected to tensile strength tests and low-cycle fatigue testing.



2. PROBLEM STATEMENT

The objective of the Aerothermodynamic Integration Model (AIM) is to verify the feasibility of integrating various analytical and experimental data obtained for the design of the Hypersonic Ramjet Engine, and to evaluate the overall engine performance of this design. The design of this model will be directed to evaluating aerodynamic characteristics without major concern for the structural life of the model.



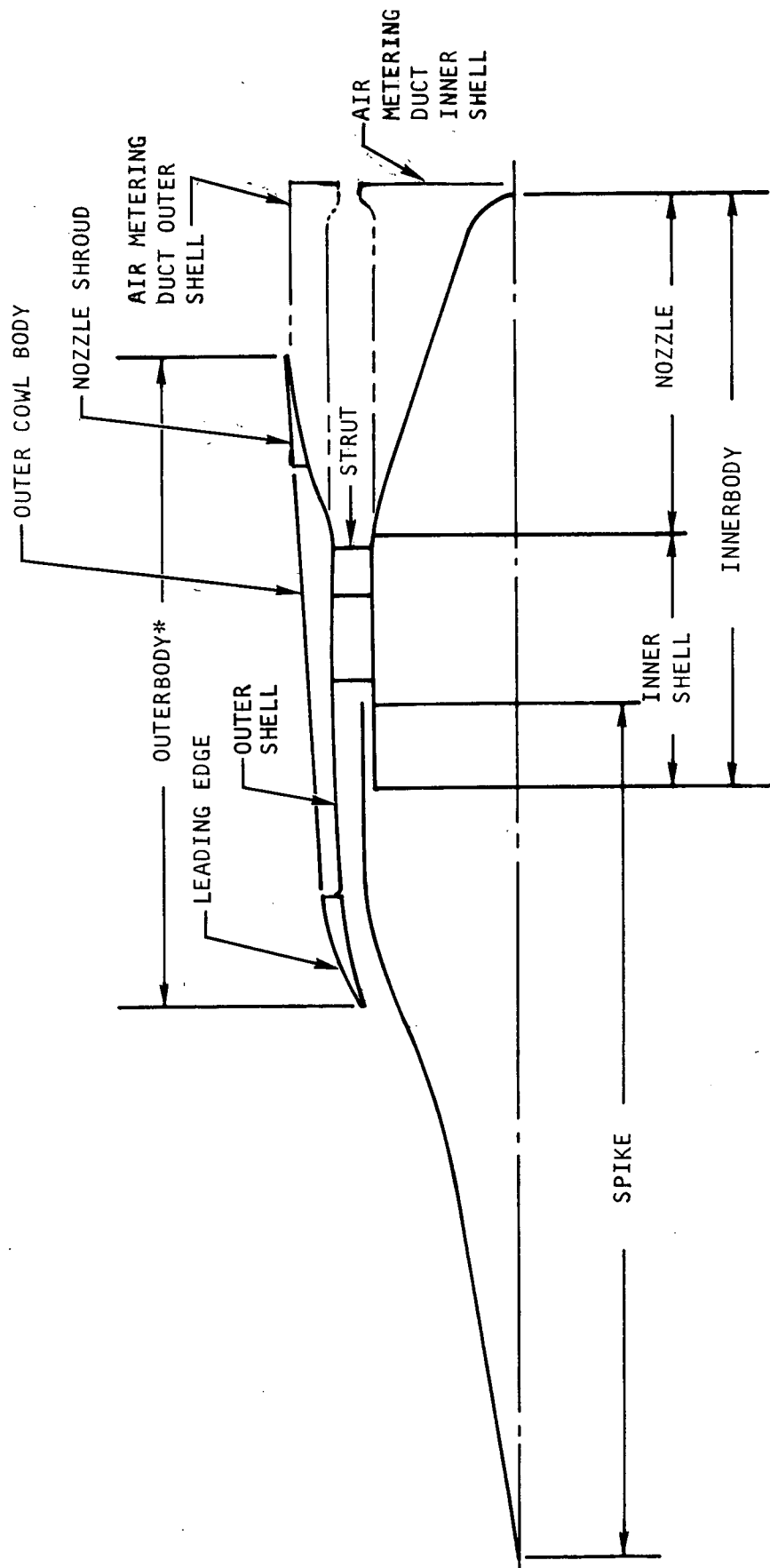
3. TOPICAL BACKGROUND

The Aerothermodynamic Integration Model (AIM) will be a water-cooled, ground-test model of the Hypersonic Research Engine.

The nomenclature used to describe the various aerodynamic surfaces of this engine is shown in Figure 3-1.

General design guides to be followed in the design of the AIM will be (1) the aerodynamic contours of the AIM will be those obtained from component testing wherever possible, (2) the surface temperature of the engine will be dictated by the maximum metal temperature allowable for structural integrity and by requirements of preventing boiling of the water used as the coolant, and (3) in order that the engine may be tested over the range from Mach 3 to 8, the inlet spike will be mechanized to permit translation.





*OUTERBODY = LEADING EDGE + OUTER SHELL + NOZZLE SHROUD + COWL

S-57176

Figure 3-1. Aerothermodynamic Integration Model Nomenclature

4. OVERALL APPROACH

The basic design concepts previously submitted were used in the component layout drawing. However, due to the diverse requirements imposed upon the design to satisfy the considerations of thermal analysis, structural design, mechanical design and manufacturing techniques, tests will be conducted to determine the internal aerodynamic performance over Mach number range of 4.0 to 7.0. The effects of varying inlet air total pressure and temperature, fuel-air ratio, inlet spike position, and combustion mode will be investigated. All tests will be conducted with clean air. The measured performance will have to be corrected to account for heat removed by the water-cooling system.

Tests will be performed in two series. The first will be oriented toward (1) evaluating the inlet-combustor interaction and stability, (2) evaluating the performance of the positive ignition system, (3) identifying conditions when autoignition is feasible, (4) demonstrating combustion mode transition, and (5) evaluating inlet and combustor performance.

The second series of tests will be performed to (1) determine overall engine performance, (2) determine engine operating characteristics with feasible variations in fuel equivalence ratio, and (3) determine nozzle performance for the purpose of substantiating the predicted overall engine performance, including chemical kinetic effects.



5. ANALYTICAL DESIGN

5.1 NITROGEN PURGE SYSTEM ANALYSIS

During testing of the AIM unit, the compartment bounded by the outer shell assembly and the outer cowl body must be purged to prevent damage to the components of the AIM by inflow of the tunnel hot gas. Furthermore, purging of this area is necessary to prevent accumulation of hydrogen. Pressurizing this cavity creates a force unbalance resulting from (1) the difference in area between the front and aft section of the unit, and (2) pressure differential created by the many obstacles within this cavity.

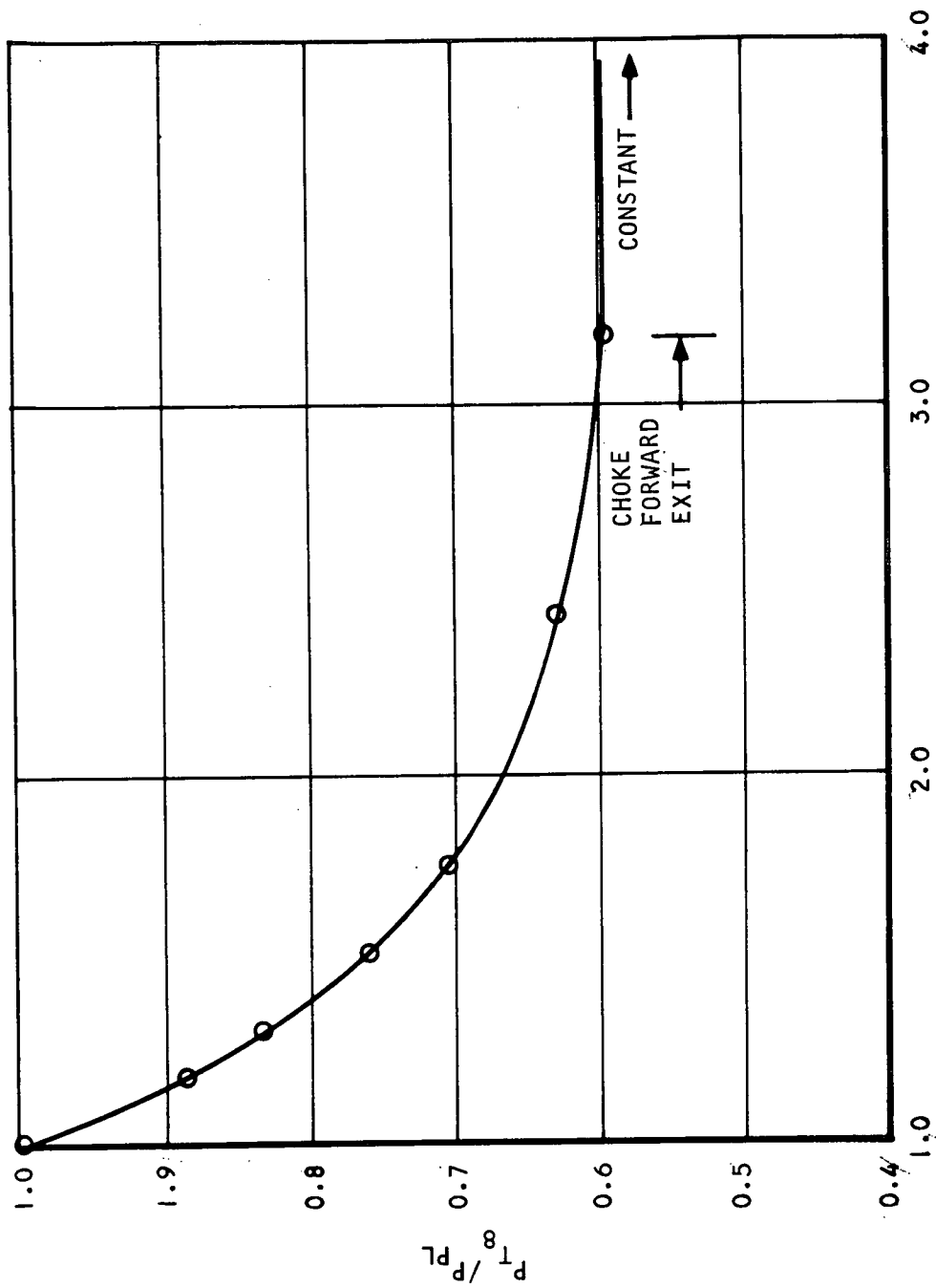
An analysis of the flow of nitrogen purge gas through the space between the AIM outer shell and the cowl was conducted to assess the drag force and pressure-drop characteristics. The cavity drag/internal pressure becomes constant when both fore and aft overboard exhaust slots are choked. This means that the internal drag is independent of external flow when both exit slots are choked, and furthermore, that the correction to the balance force can be obtained from a calibration under quiescent external conditions. A calibration analysis was given in Reference 5-1. The internal drag analysis is presented below.

Flow areas within the purge cavity were estimated from engine drawings. It was determined that three regions of flow restriction exist between the forward circumferential overboard exhaust slot and the plenum where nitrogen is dumped into the cavity from feed lines. This leads to a requirement for high plenum pressures to effectively choke the forward overboard exit. In contrast, there is virtually no blockage to flow between the dump plenum and the aft overboard slot.

Internal pressure losses were calculated with the simplifying assumption that friction and entrance losses are small and can be ignored in comparison with the dump losses along the flow path. Dump losses were then assumed to consume all of the dynamic pressure in the restricted area immediately upstream of a given area expansion. The resulting pressure loss curve of the flow from the plenum to the forward exit slot is given in Figure 5-1. Note that choking is predicted at a pressure ratio of approximately 3.2 between the plenum and the local exhaust static pressure near the forward exit.

The above losses indicate a choked-flow split for the configuration analyzed to be 34 percent of the flow through the forward slot and 66 percent through the rear slot.



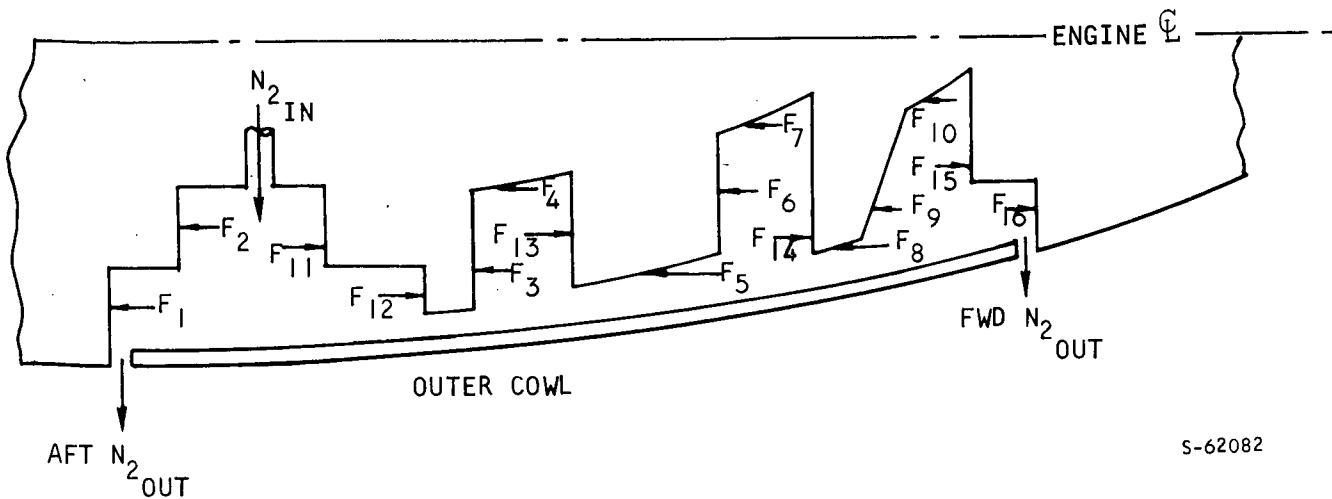


P_{PLEN}/P_{AMB}

S-62075

Figure 5-1. HRE/AIM Internal Pressure Losses - N_2 Purge Gas
Flowing to Forward Slot

The internal forces were then calculated from the pressure and area distributions. These forces are represented schematically below:



S-62082

The net force was obtained from the summation

$$(F_1 + F_2 + \dots + F_{10}) - (F_{11} + \dots + F_{16}) = F_{NET}$$

Calculations of these forces were extended over a range of plenum pressure ratios as shown in Figure 5-2. The force plotted acts in the aft direction on the outer shell, exerting an effective drag force on the engine. Thus, the AIM cavity drag increases in direct proportion to cavity pressure, an example of which was given in Reference 5-1.

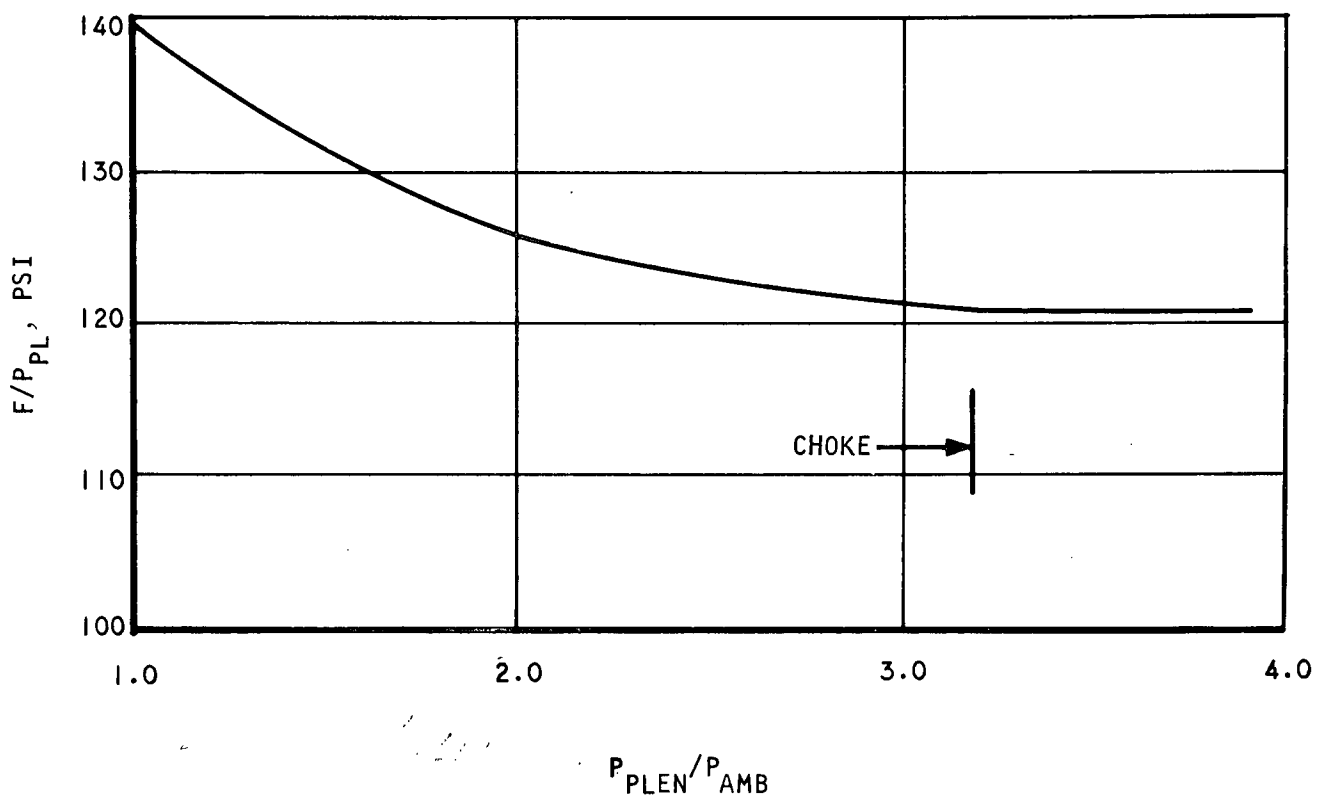
5.2 HEAT TRANSFER ANALYSIS

5.2.1 Instrumentation Assembly

A heat transfer analysis of the instrumentation assembly, PN 950592, was performed. The instrumentation assembly consists of five AiResearch-designed total/static pressure probes and five NASA-designed total temperature probes (modified only in the support section), and a water-cooled ring support assembly.

Pressure-drop analysis and orifice sizing for the various flow paths of the instrumentation assembly were made. Approximately 330 gpm (45 lb/sec) of water flow is required to cool the assembly and its probes. Water enters the support assembly at one leg and splits into two main routes; one clockwise and the other counterclockwise along the circumference, and leaves the assembly at the other support leg. Each main flow is further divided into two parts by the web which is required for structural purpose. The web and the cross section of the assembly are shown in Zone 7 of AiResearch Drawing 950592 attached at the end of this report. The flow distribution among the four branches is governed by the orifices at the exit station.





S-62073

Figure 5-2. HRE/AIM Engine Drag Force Due to Nitrogen Purge



The internal flow resistance of the assembly cannot be accurately estimated for the following reasons:

- (a) The pressure loss coefficients for bleed flows, contraction, sudden expansion, etc., found in the standard text books are not precise.
- (b) When these flow devices are in series, the overall pressure loss usually exceeds the sum of the individual part. Test data indicate that the overall pressure loss for three 90-deg turns arranged in a zigzag manner is nearly 9-times that for a single 90-deg turn.

The multiple flow disturbances occur within the probe's support bracket which is shown in Sections A-A and E-E of Drawing 950592. The bracket forms a flow channel with the ring's outer skin to direct the coolant to the probe and to provide local cooling for the outer skin of the rig. The flow disturbances are caused by (1) the blockage of the thermocouple wire connectors and pressure-tube connectors, and (2) the bleed flows from the side wall and the outward flow of coolant to the probe. The predicted overall pressure drop between the inlet station and the exit station of the assembly is 10 psi, approximately. With the available pressure on the order of 200 psia, the interest of this analysis lies in the determination of the flow distribution rather than the magnitude of pressure losses. If flow reportioning should become necessary, the only change required would be to replace the outlet orifice with one of a different size.

The analysis results are tabulated in Table 5-1. Shown in Table 5-1 are the bleed area and weight flows for different channels at various positions of the assembly. The pressure distributions for Channels 1 and 2 are shown in Figure 5-3. The predicted wall temperatures for the most severe heating conditions are indicated in Figure 5-4 with the peak metal temperature being 900°F. These temperatures given for the outer skin were determined for $M_\infty = 6$ while the temperatures given for the inner skin were determined for $M_\infty = 7$ conditions, and a local Mach number of $M = 2.7$.

The flow-proportioning orifices which are located at the exit port of the assembly are shown in AiResearch Drawing 950815, attached at end of this report. The required areas are 0.98 in.² and 2.9 in.² for channels 1 and 2, respectively, for the clockwise flow branch. For the counterclockwise branch, the flow areas are 0.6 in.² and 0.95 in.² for channels 1 and 2, respectively.



TABLE 5-1
FLOW DISTRIBUTION AND BLEED AREA REQUIREMENTS

Assembly Position	Angular Position, deg							
	260	280	330	0	30	70	110	180
W_{2i}	15.4	12.9	12.3	11.0	9.0	8.0	7.0	7.7
W_{2e}	14.8	12.9	12.3	10.8	8.7	8.5	7.9	5.22
W_{2-3}	0.6	0	0	0.2	1.1	0.9	0.7	2.48
A_{2-3}	1.2	0	0	0.6	1.9	1.9	1.0	1.9
W_{3i}	4.2	4.4	4.0	4.3	3.0	2.5	2.6	3.3
W_{3e}	2.5	3.4	3.0	1.2	1.8	1.1	2.3	2.48
W_p	2.3	1.0	1.0	3.3	2.3	2.3	1.0	3.3
W_1	9.4	9.4	9.4	9.4	8.6	7.2	5.6	5.0
W_{1-2}	0	0	0	0	0.8	1.4	1.6	0
A_{1-2}	0				0.6	1.35	1.35	

Symbols:

W flow rate, lb/sec

A_{1-2} bleed area between channels 1 and 2, in.²

A_{2-3} bleed area between channels 2 and 3, in.²

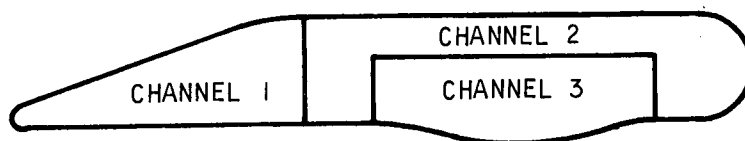
Subscripts:

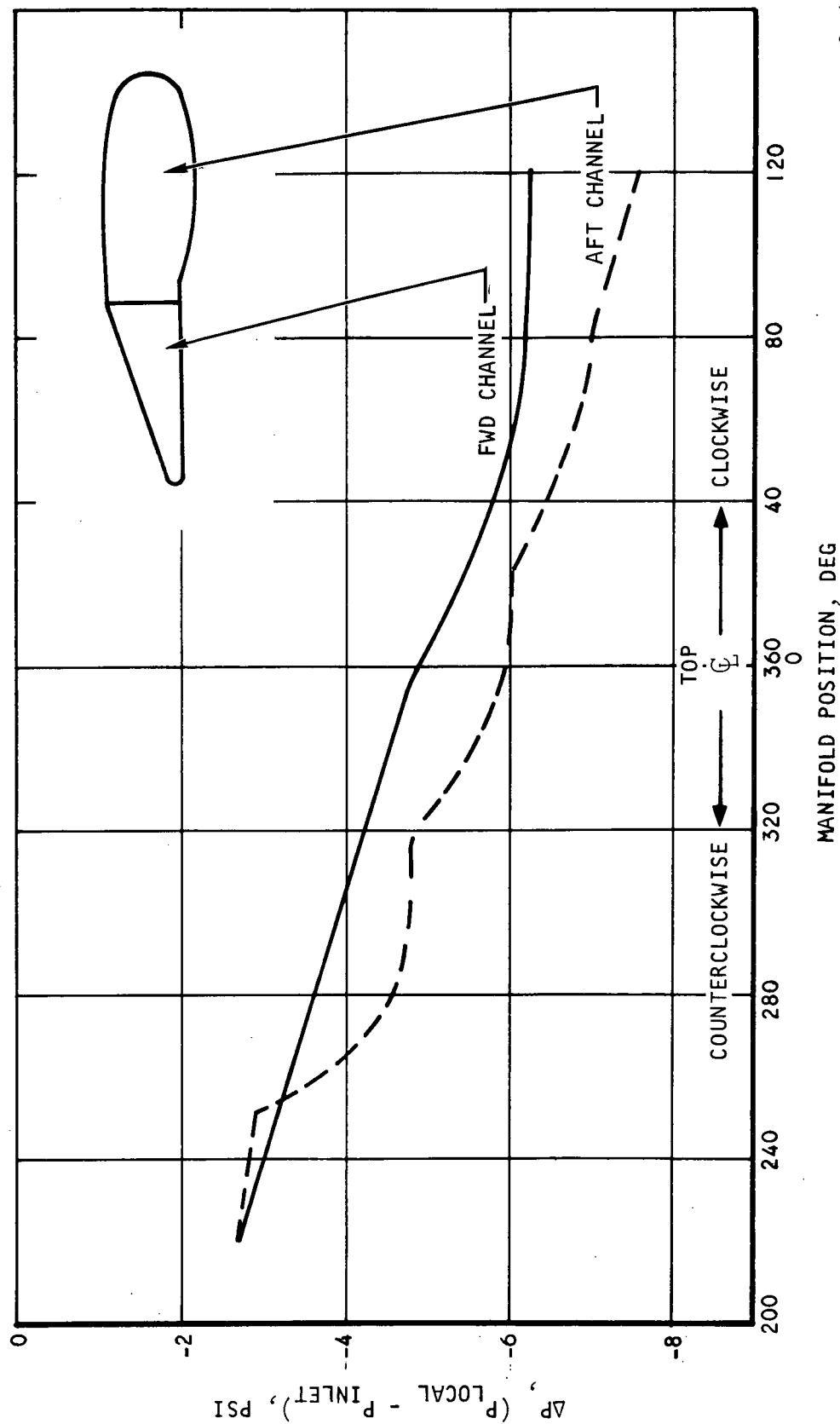
1, 2, 3 channels 1, 2, and 3 respectively (see sketch below)

e exit station of local section

i inlet station of local section

p probe



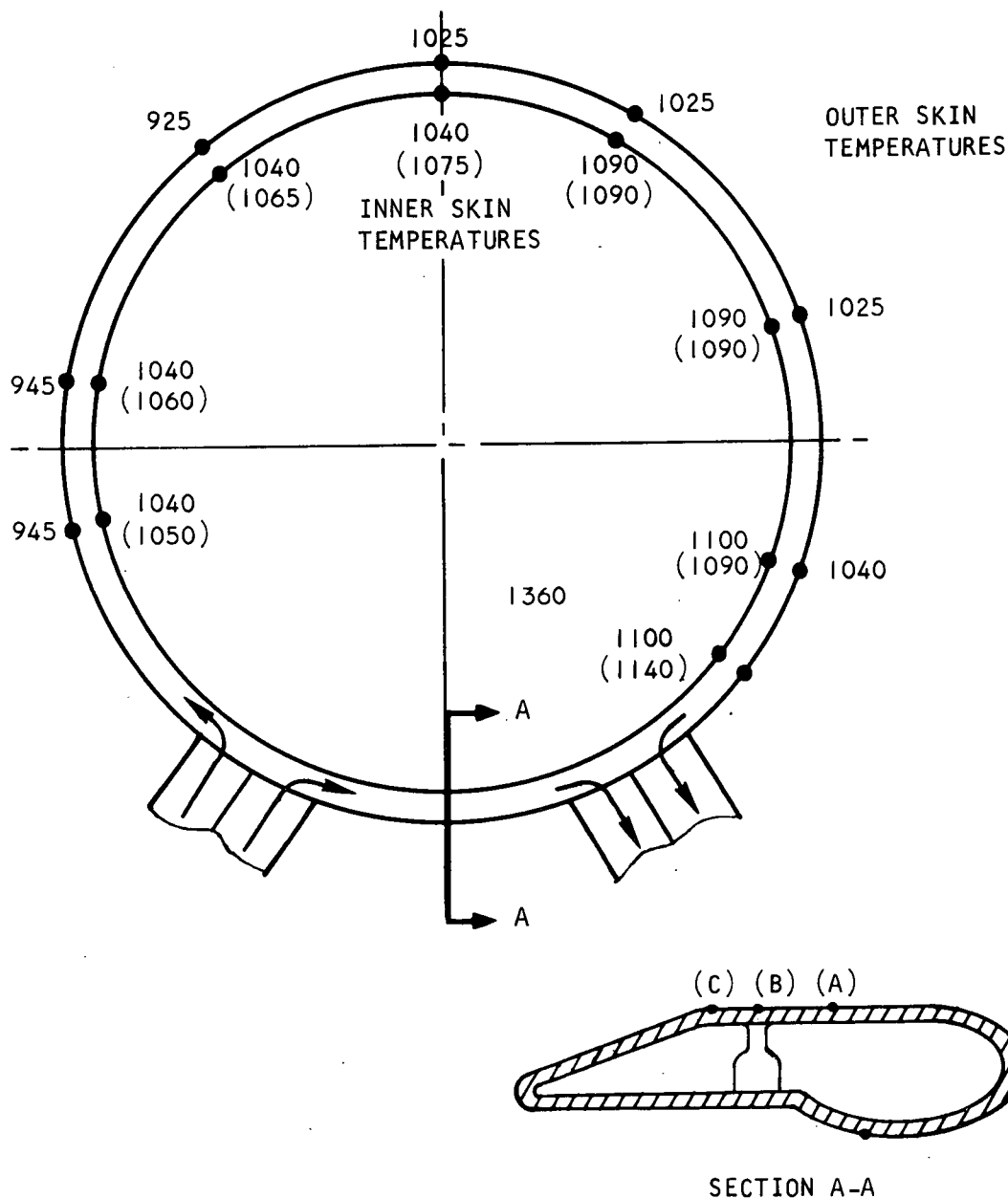


S-62076

Figure 5-3. Instrumentation Assembly Pressure Distribution



- NOTES: 1. ALL TEMPERATURES IN $^{\circ}\text{R}$
 2. NUMBERS IN PARENTHESES CORRESPOND TO POSITION "A"
 3. NUMBER IN RECTANGLE CORRESPONDS TO POSITION "B"
 4. ALL OTHERS CORRESPOND TO POSITION "C"



S-62079

Figure 5-4. Instrumentation Assembly Surface Temperatures



AIRESEARCH MANUFACTURING COMPANY
 Los Angeles, California

5.2.2 Air-Metering Duct Thermocouple Rake

To increase the accuracy of the airflow measurement by the air-metering duct, a rake consisting of five equally spaced 0.03-in.-dia platinum thermocouples is located at Station X = 80. The thermocouples are supported by a holder which is made of 0.05-in.-wall-thickness platinum sheet folded into a plate 0.25-in. thick with full radius at the leading edge. The assembly is insulated from its back cover and from the wall of the air-metering duct with zirconium oxide as shown in Figure 5-5.

In order to determine the possible error of this system due to conduction, the assembly was divided into 74 nodes and analyzed with the Steady-State Thermal Analyzer Program H0298. The predicted temperature error is less than 3 percent for uniform fluid properties, and slightly more than 3 percent if a 7th power velocity profile and Crocco's temperature distribution are assumed. The results from the computer are tabulated in Table 5-2.

TABLE 5-2

PREDICTED TEMPERATURE ERROR FOR AIR-METERING DUCT THERMOCOUPLES

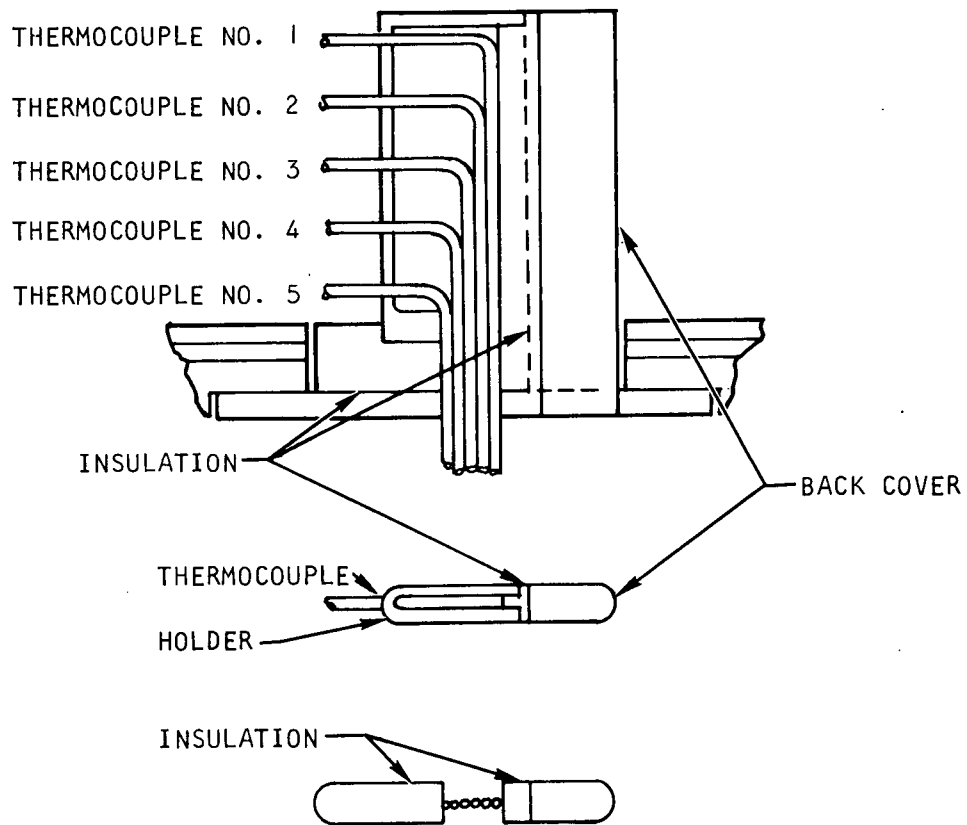
	Thermo- couple	Velocity, V, ft/sec	Recovery Temp, T_r , °R	Thermo- couple Reading, °R	ΔT , °R	Percent Error
A. Duct profile	1	640	3100	3090	-10	-0.32
	2	825	3310	3217	-93	-2.9
	3	885	3310	3207	-103	-3.2
	4	830	3160	3070	-87	-2.8
	5	730	2780	2800	+20	+0.7
B. Uniform fluid properties	1	800	3200	3169	-31	-1.0
	2	800	3200	3170	-30	-0.95
	3	800	3200	3166	-34	-1.07
	4	800	3200	3152	-48	-1.5
	5	800	3200	3118	-82	-2.6

Numerical designation of each thermocouple is shown in Figure 5-5.

5.2.3 Nickel Leading and Trailing Edges Heat Transfer Analysis

This section presents predictions of metal temperatures for the HRE/AIM leading and trailing edges when subjected to several wind tunnel heating conditions at Plumbrook. The analyzed leading and trailing edge configurations are similar to those in AiResearch Drawings 950554 and 950506, respectively, except that Nickel-200 (thermal conductivity = 25 Btu/hr-ft-°F) was used. Zirconium-copper





S-62084

Figure 5-5. Air-Metering Duct Thermocouple Rake



(thermal conductivity = 198 Btu/hr-ft-°F) was specified as the leading edge material and OFHC Copper (thermal conductivity = 210 Btu/hr-ft-°F) was specified as the trailing edge material in Drawings 950554 and 950506, respectively. The object of the analyses was to determine whether Nickel-200 could be feasibly substituted for zirconium-copper and OFHC Copper. The criteria for substitution is a Nickel-200 thermal cycle fatigue life that exceeds the 100 cycles proposed for HRE/AIM testing. The thermal cycle fatigue life of Nickel-200 was expected to be lower than zirconium-copper and OFHC Copper, because the lower Nickel-200 thermal conductivity would not allow operating temperatures as low as zirconium-copper (800°F maximum leading edge tip temperature).

Results of the analyses indicate that Nickel-200 can be used in the leading edge design if the "shock-outside-lip" condition is avoided for most of the tests. An estimated maximum trailing edge temperature of 1000°F with Nickel-200 indicates that Nickel-200 can be used instead of OFHC Copper. Details of the analyses are discussed below.

5.2.3.1 Leading Edge

Predicted leading edge maximum tip temperatures with Nickel-200 are presented in Table 5-3. Predictions were performed for three tunnel Mach numbers (5, 6, and 7), two tunnel total pressures (500 and 1000 psia), and three spike bow shock locations relative to the leading edge--shock on leading edge tip (shock impingement), shock inside leading edge, and shock outside leading edge. The hot gas for all tunnel conditions was clean air.

Results in Table 5-3 indicate that leading edge tip metal temperatures are highest (1773°F maximum at Mach 7, 1000 psia) when the spike bow shock wave is outside the leading edge. These metal temperatures (shock outside) are from 220° to 265°F higher than tip metal temperatures with shock impingement for the same tunnel condition. These higher (shock outside) metal temperatures result from a higher average hot gas heat transfer coefficient over the 0.030-in. radius leading edge stagnation region ($0.317 \text{ Btu/sec-ft}^2\text{-}^\circ\text{R}$ maximum at Mach 7, 1000 psia). With shock impingement, a peak coefficient of $1.32 \text{ Btu/sec-ft}^2\text{-}^\circ\text{R}$ over a 0.0025 in. width and an average coefficient of $0.198 \text{ Btu/sec-ft}^2\text{-}^\circ\text{R}$ (corresponding to $0.317 \text{ Btu/sec-ft}^2\text{-}^\circ\text{R}$ with shock outside) were used at Mach 7, 1000 psia. The high impingement heat flux over the 0.0025-in. width is dissipated into adjacent regions of the leading edge to maintain a lower maximum metal temperature (1528°F at Mach 7, 1000 psia) than with shock outside (1773°F). With shock inside the leading edge ($0.198 \text{ Btu/sec-ft}^2\text{-}^\circ\text{R}$ over the stagnation region at Mach 7, 1000 psia and no shock impingement effects), the maximum tip temperature is 1472°F, or 56°F lower than with shock impingement. The average leading edge heat transfer coefficient with shock outside ($0.317 \text{ Btu/sec-ft}^2\text{-}^\circ\text{R}$) is higher than with shock impingement or with shock inside ($0.198 \text{ Btu/sec-ft}^2\text{-}^\circ\text{R}$), because the air stagnation total pressure behind the spike bow shock wave is higher.



TABLE 5-3
THERMAL RESULTS OF HRE/AIM NI-200 LEADING EDGE ANALYSIS

M_∞	P_{TOT} psia $_\infty$	T_{TOT} °R $_\infty$	Shock Location	Max. Tip Metal Temp, °F (See Fig. 5-7)	Water Side Metal Temp, °F (See Fig. 5-7)	Max. L.E. Heat Transfer Coeff, Btu/sec-ft 2 -°R	T (See Fig. 5-7)	S (See Fig. 5-7)	P (See Fig. 5-7)	h_{F-R} Btu/sec-ft-°R (See Fig. 5-7)
7	1000	3830	Tip (Shock Impingement)	1527	198	1.32	1	12	1	0.110
			Inside	1372	195	0.198	1.8	1	1	
			Outside	1773	222	0.317	1.8	1	1.6	
	500		Tip	1238	182	0.933	1	12	1	0.078
			Inside	1095	200	0.140	1.8	1	1	
			Outside	1460	229	0.224	1.8	1	1.6	
6	1000	2940	Tip	1485	202	1.38	1	6.9	1	0.200
			Inside	1420	200	0.360	1.8	1	1	
			Outside	1730	270	0.521	1.8	1	1.45	
	500		Tip	1349	186	0.975	1	6.9	1	0.141
			Inside	1182	185	0.254	1.8	1	1	
			Outside	1512	216	0.369	1.8	1	1.45	
5		2205	Outside	893	168	0.288	1.8	1	1	0.16



Leading edge cycle life expectancy with Nickel-200 was determined from the "cycles-to-failure vs maximum leading edge temperature curve" in Figure 5-6 and the proposed HRE/AIM 100-cycle test plan inset in Figure 5-6. Results indicate that with shock impingement on leading edge tip (except at Mach 5) the 100 proposed cycles will expend 44.7 percent of the leading edge cycle life. Conversely, the 100 proposed test cycles could be repeated 2.24 times (i.e., 224 cycles) before a failure is expected. With shock outside leading edge, 93.9 percent of the leading edge cycle life is expended after 100 cycles because tip temperatures with this shock position are higher. Life expectancy calculations using the data in Figure 5-6 are presented in Table 5-4.

Leading edge temperatures were calculated using a steady-state thermal analyzer computer program (H2539). The nodal network is shown in Figure 5-7 with metal temperatures indicated for Mach 7, 1000 psia, shock impingement conditions. Stagnation region heat transfer coefficients used in the analyses are indicated in Table 5-3. The multipliers used with the Fay-Riddell coefficient (Reference 5-2) to obtain these stagnation heat transfer coefficients are included in Table 5-3. Explanation of these multipliers is presented in Figure 5-8. Hot gas heat transfer coefficient distributions on the inside and outside surfaces of the leading edge are presented in Figure 5-9. Distributions around the leading edge were calculated from results in Reference 5-3.

A heat transfer analysis of the leading edge with zirconium-copper was performed for Mach 6.65, 1200 psia total pressure, shock impingement conditions. Results of this analysis were reported in Reference 5-4. Since this analysis was performed, wind tunnel conditions have changed and aerodynamic heat transfer techniques have been updated. A summary of the similarities and differences between the analysis reported in Reference 5-4 and the analyses presented herein (Mach 7, 1000 psia, shock impingement conditions) are presented in Table 5-5 for reference.

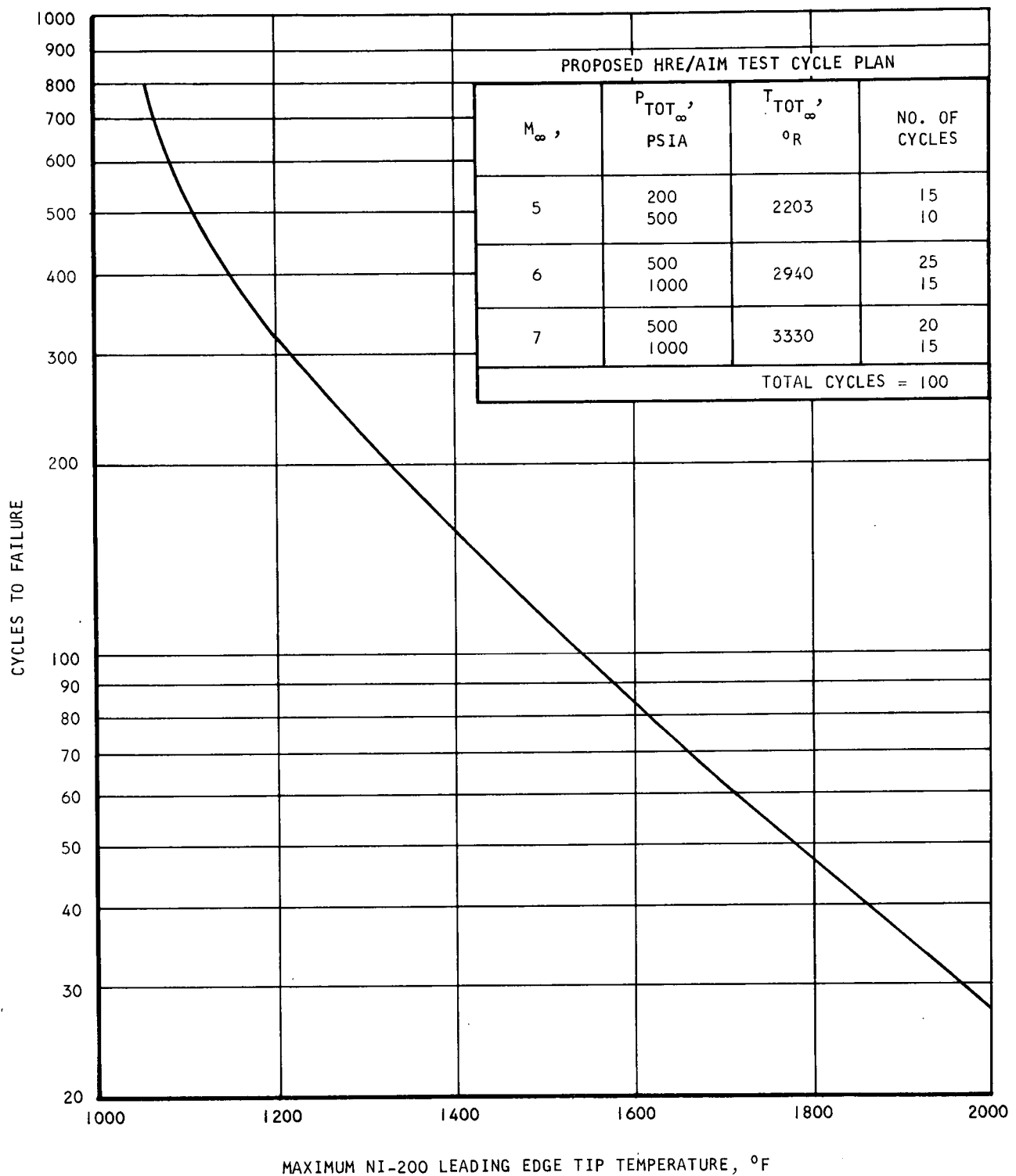
In the analyses reported herein, a laminar flow turbulence multiplier (T) of 1.8 was used in the heat transfer calculation to indicate the effect of freestream turbulence of 4 to 8 percent. However, the freestream turbulence at the Plumbrook wind tunnel test facility has been estimated at about one percent. Thus, the turbulence multiplier of 1.8 used in the analyses reported herein is higher than would be expected during test.

5.2.3.2 Trailing Edge

Results indicate a trailing edge tip temperature with Nickel-200 of 1000°F and a water-side metal temperature of 300°F. Previous analyses (Reference 5-5) using OFHC copper indicate corresponding temperatures of 600°F and 260°F, respectively. The length between the water passage and tip is 0.633 for both analyses (Drawing 950506).

The results for Nickel-200 are based on a gas-side heat flux of 44 Btu/sec-sq ft which was assumed over the entire trailing edge tip (actual external side tip heat flux is about 10 to 15 percent of the internal-side heat flux). Heat flux at the very tip of trailing edge is higher (100 Btu/sec-sq ft) due to a mild interaction of the internal and external flows. If this interaction effect were neglected, the Nickel-200 trailing edge tip maximum temperature would be 650°F.





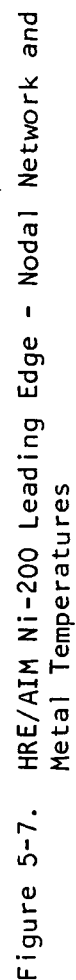
S-62093

Figure 5-6. Cycles-to-Failure vs Maximum Tip Temperature



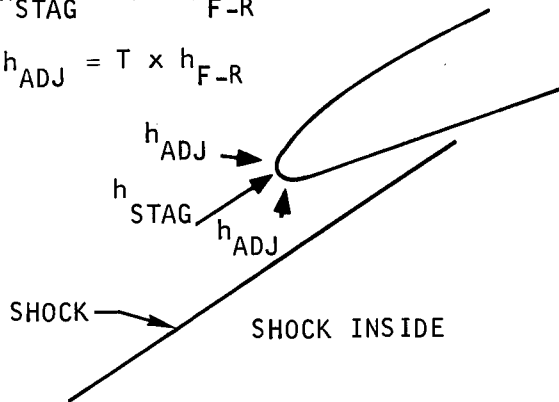
TABLE 5-4
ESTIMATE OF HRE/AIM NI-200 LEADING EDGE CYCLE LIFE

M_∞	P_{TOT_∞} , psia	T_{TOT_∞} , °R	Shock Location	Max. Tip Metal Temp, °F (Table 5-3)	A Cycles to Failure (Fig. 5-5)	B Proposed Cycles (Inset in Fig. 5-5)	$\frac{B}{A}$
7 → 6 → 5	1000 500 1000 500 →	3830 → 2940 → 2205	Tip (Shock Impingement) → Outside	1527 1238 1495 1349 893	100 275 115 265 ∞	15 20 15 25 10	0.150 0.073 0.130 0.094 0.0
							$\Sigma \rightarrow 0.447$
7 → 6 → 5	1000 500 1000 500 →	3830 → 2940 → 2205	Outside →	1773 1460 1730 1512 893	49 125 55 105 ∞	15 20 15 25 10	0.306 0.160 0.273 0.200 0.00
							$\Sigma \rightarrow 0.939$



$$h_{STAG} = T \times h_{F-R}$$

$$h_{ADJ} = T \times h_{F-R}$$



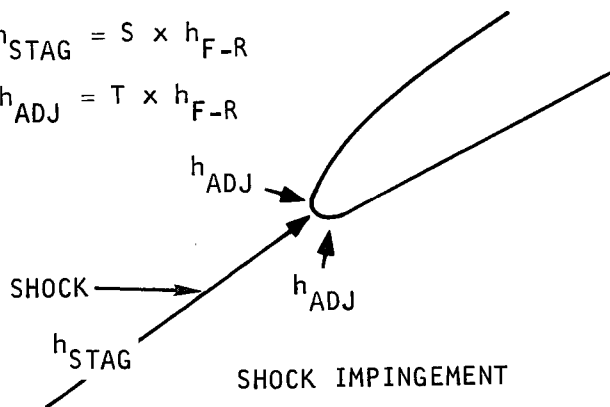
h_{STAG} = CONVECTIVE HEAT TRANSFER COEFFICIENT AT STAGNATION POINT

h_{ADJ} = CONVECTIVE HEAT TRANSFER COEFFICIENT ADJACENT TO STAGNATION POINT

h_{F-D} = CONVECTIVE HEAT TRANSFER COEFFICIENT BASED ON METHOD OF FAY-RIDDELL AND ON "SHOCK INSIDE" CONDITIONS

$$h_{STAG} = S \times h_{F-R}$$

$$h_{ADJ} = T \times h_{F-R}$$



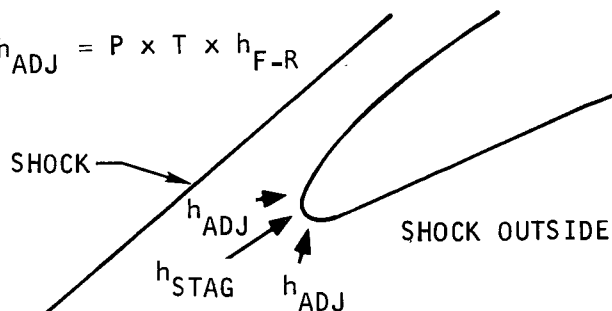
T = TURBULENCE FACTOR

S = SHOCK IMPINGEMENT MULTIPLIER

P = MULTIPLIER TO ACCOUNT FOR INCREASED PRESSURE BEHIND SPIKE SHOCK WAVE

$$h_{STAG} = P \times T \times h_{F-R}$$

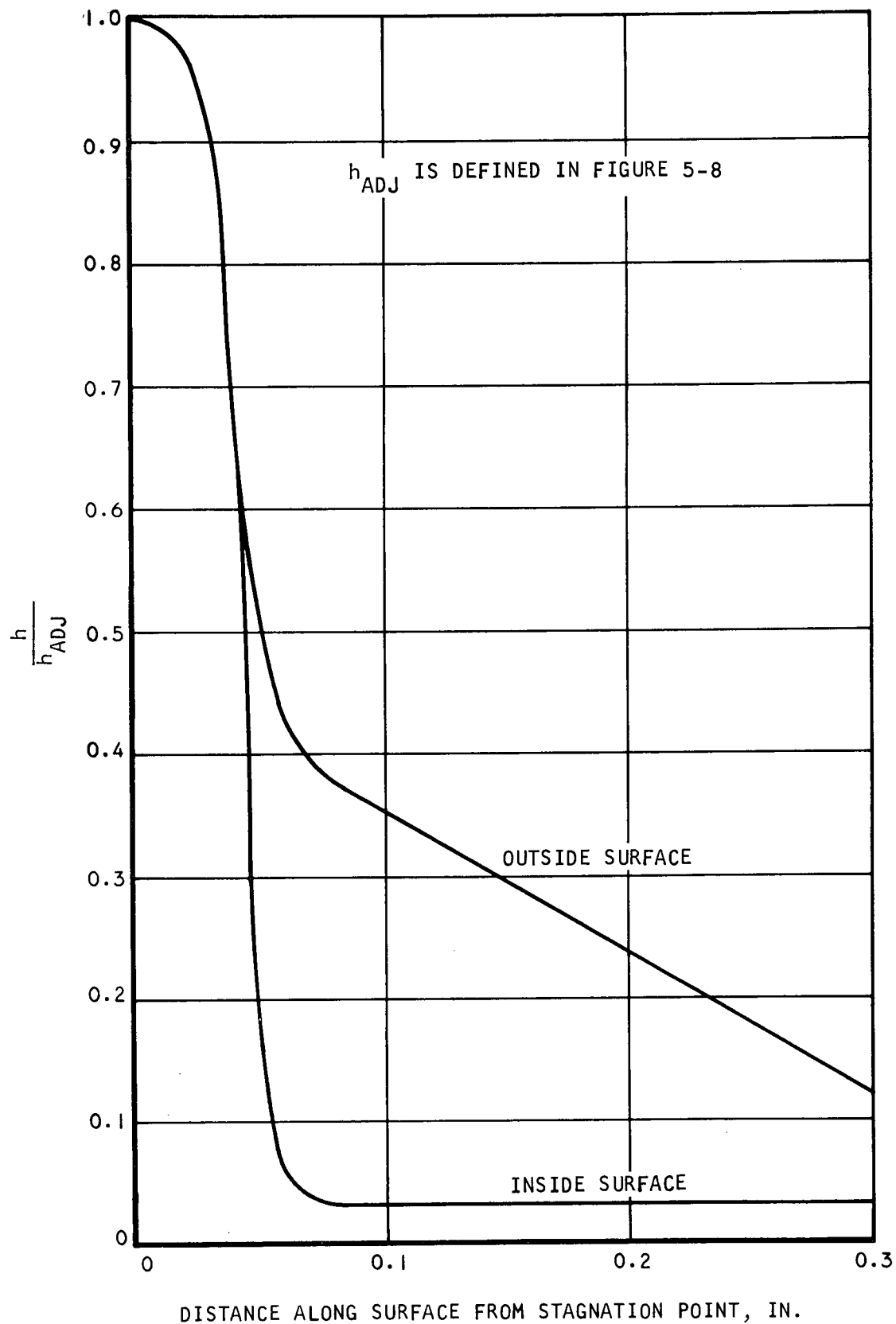
$$h_{ADJ} = P \times T \times h_{F-R}$$



S-62081

Figure 5-8. HRE/AIM Ni-200 Leading Edge - Heat Transfer Nomenclature





S-62074

Figure 5-9. Hot Gas Coefficient Distribution Along Leading Edge Sides



AIRSEARCH MANUFACTURING COMPANY
Los Angeles, California

70-6800
Page 5-18

TABLE 5-5
COMPARISON OF LEADING EDGE HEAT TRANSFER ANALYSES

Item	Present Analysis	Previous Analysis (Reference 5-4)
M_{∞}	7	6.65
$P_{TOT_{\infty}}$, psia	1000	1200
$T_{TOT_{\infty}}$, °R	3830	3770
Hot gas	Clean air	Vitiated air
Hot gas enthalpy, Btu/lbm	1050	1330 *
Shock impingement	Yes	Yes
h_{SHOCK}/h_{F-E} (Heat transfer coeff)	12	15.5
h_{F-R} , Btu/sec-ft ² -°R (Ref 5-2)	0.110	0.171
h (avg on sides of L.E.), Btu/sec-ft ² -°R	0.020	0.20
Leading edge material	Nickel-200	Zirconium-copper
Thermal conductivity, Btu/hr-ft-°R	25	198
Leading edge length, in.	0.316	0.300
Max. tip temp, °F	1527	800
Water side metal temp, °F	198°F	330

* Same as Mach 8 Flight, B-B Line.



5.3 INSTRUMENTATION ASSEMBLY STRESS ANALYSIS

5.3.1 Summary

The instrumentation rake structure per AiResearch Drawing 950592 has been analyzed for stresses due to containment pressure and for aerodynamic loads during wind tunnel testing. Pressure stresses predominated throughout the structure and the various thicknesses were established to satisfy containment loads. The ring and leg structure was also analyzed for deflections and rotations due to aerodynamic loads. This was done to verify that the various probe tips would not undergo excessive displacements due to steady-state aerodynamic forces.

The most pertinent and critical computations are provided below. The structure is satisfactory for the various load conditions, and it will perform its intended function.

5.3.2 Analysis

5.3.2.1 Allowable Stresses and Design Conditions

The ring and leg structures are constructed from Inconel 625. The peak metal temperatures on the surfaces exposed to aerodynamic testing will be subjected to operating pressures at the maximum temperature and to rated proof pressure at room temperature (RT). The design containment pressures are:

$$P_{\text{oper.}} = 300 \text{ psi (600}^{\circ}\text{F mean metal temp.)}$$

$$P_{\text{proof}} = 450 \text{ psi (RT)}$$

The following material properties are applicable:

$$f_{\text{ty}} = 50,000 \text{ psi at } 600^{\circ}\text{R}$$

$$f_{\text{ty}} = 60,000 \text{ psi at RT}$$

The allowable stresses have to be set at 85 percent of the yield strength to preclude permanent deformation in any portion of the load carrying structure. This leads to the following allowable stresses:

$$\sigma_{\text{all}} = 42,500 \text{ psi at } 600^{\circ}\text{F}$$

$$\sigma_{\text{all}} = 51,000 \text{ psi at RT}$$

It can be readily seen that the room temperature proof-pressure condition is the governing design load with respect to containment.

The other prime design consideration was the requirement to limit radial deflection of the probe tips to 0.050 in. at maximum tunnel test conditions. A total of ten probes are mounted from the ring structure inside surface.



Four of the probes are located at or near the top of the ring relative to the support legs, four probes are at or near the mid-height of the ring, and two probes are at the lower part of the ring. The ring has a 13-in. radius and is supported from two support legs that are located 30 deg from the vertical centerline of the ring. The aerodynamic forces at maximum rated conditions have been given as:

Axial load on each probe = 50 lb

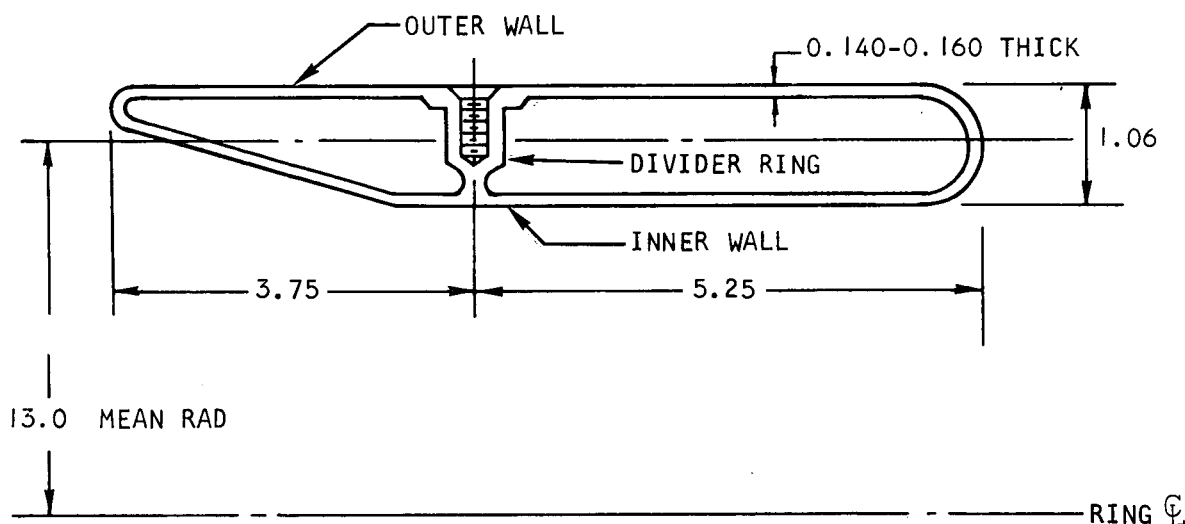
Ring load = 2.5 lb/in. on its 80-in. circumference

Leg load = 5.3 lb/in. along 23.6 in. length

The axial centerline of each probe is located on a 10-in. radius relative to the ring centerline, and hence they are 3 in. radially inward from the ring structure.

5.3.2.2 Pressure Stresses on Ring (AiResearch Drawing 950596)

The various cross sections of the ring were analyzed for thickness requirements and basic design concept prior to finalizing the design. The critical design considerations were membrane stresses due to pressure, and buckling of the ring inner wall which is exposed to external pressure loading due to containment. The final detailed ring cross section is depicted below.



S-62090

The divider ring shown above was utilized to keep the wall thickness of the ring structure to an acceptable value for the aerodynamic heating consideration. The total length of 9.0 in. would have required a much greater thickness



for the inner wall due to the buckling pressure, which would then have led to unacceptable metal temperatures on the heated surface.

The following calculations have been based upon the minimum allowable wall thickness of 0.140 in. The hoop stress is slightly higher for the outer wall due to the larger radius to the wall centerline. For the outer wall:

$$\sigma_{\text{Hoop}} = \frac{pR}{t}$$

where

$$p = 450 \text{ psi}$$

$$R = 13.5 \text{ in.}$$

$$t = 0.140$$

$$\sigma = \frac{(450)(13.5)}{(0.140)} = 43,400 \text{ psi}$$

This is within the allowable limit of 51,000 psi.

For the inner wall, the hoop stress is lower but the design consideration is the buckling pressure. For a short cylinder that is held circular at its ends, the appropriate formula for buckling under lateral pressure is:

$$p_{\text{crit}} = 0.868 \frac{E t^{2.5}}{l R^{1.5}}$$

where

$$E = 28.0 \times 10^6 \text{ psi}$$

$$t = 0.140 \text{ in.}$$

$$l = 5.25 \text{ in.}$$

$$R = 12.5 \text{ in.}$$

$$p_{\text{crit}} = \frac{(0.868)(28.0 \times 10^6)(0.140)^{2.5}}{5.25 \times (12.5)^{1.5}} = 917 \text{ psi}$$

The calculated critical pressure should generally show an adequate factor of safety when compared to the applied pressure to account for irregularities in shape, thickness, and end conditions. The critical pressure calculated above shows a factor of safety of slightly greater than 2.0 which is adequate and at the same time not excessively conservative for the intended service.

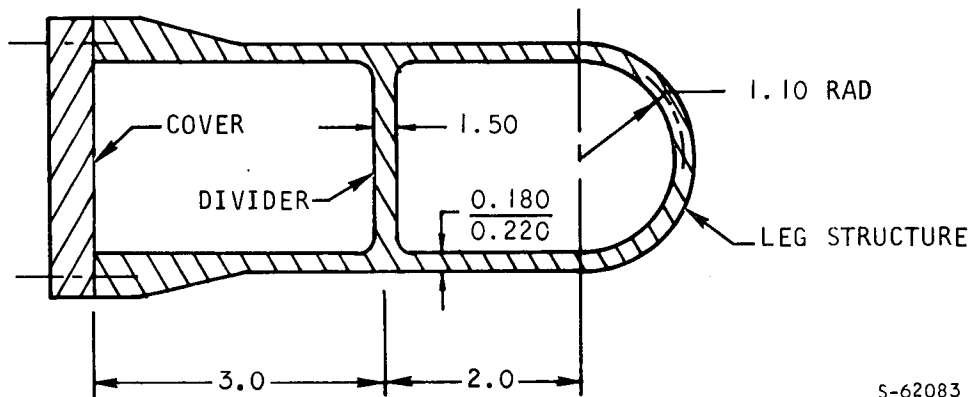
The outer wall surface is attached to the divider ring by an array of 64 0.250-28UNF (Unified National Fine) bolts around the circumference. The bolt spacing on the outer surface is 1.35 in. Each bolt will support the pressure



load between the bolts and over a length of approximately 2.5 in. This would produce a tensile loading of 1520 lb per bolt. The stress area of this fastener is 0.0326 sq in. The stress at proof pressure will be 46,500 psi which will be well below the capability of 90,000 psi minimum yield strength bolts. The bolts are made from A-286 steel.

5.3.2.3 Pressure Stresses in Legs (AiResearch Drawing 950812)

The pertinent cross sectional details of this leg are shown below.



The pressure requirements are identical to the ring. The prime consideration is bending stress in the flat sides of the leg. The unsupported spans of both the rear and front compartments are approximately 2.5 in. Using the minimum wall thickness of 0.180 in. and the formula for a built-in beam:

$$\sigma = 0.5 p \times \left(\frac{l}{t}\right)^2$$

where

$$p = 450 \text{ psi}$$

$$l = 2.5 \text{ in.}$$

$$t = 0.18 \text{ in.}$$

$$\sigma = (0.5)(450)\left(\frac{2.5}{0.18}\right)^2 = 43.300 \text{ psi}$$



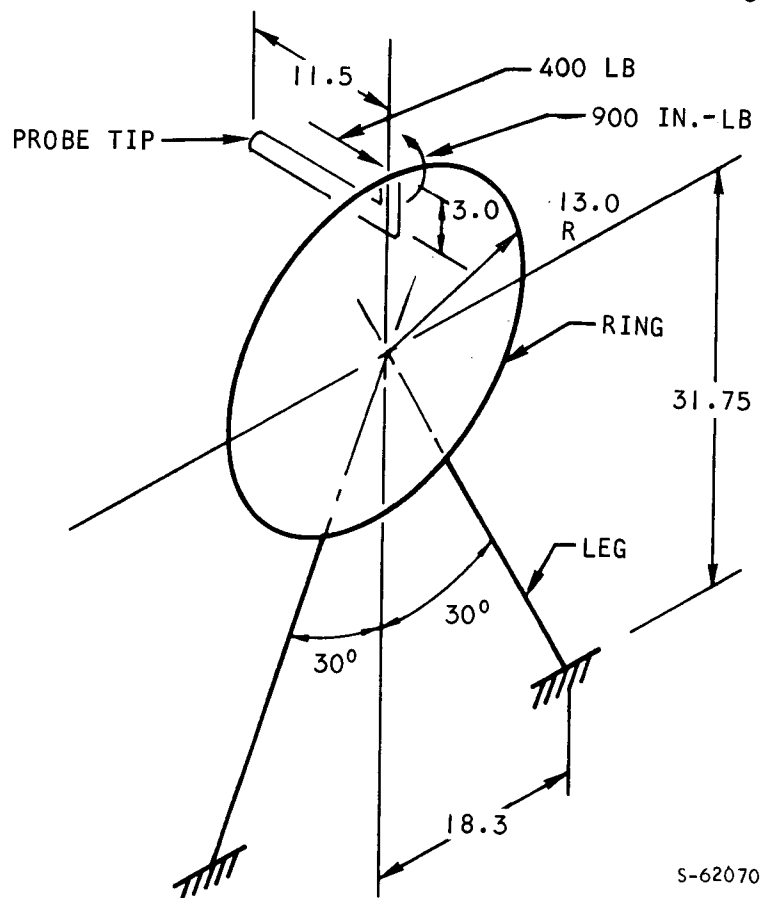
For the front section which is a 1.10-in. radius

$$\sigma = p \frac{R}{t} = (450) \left(\frac{1.10}{0.18} \right) = 2750 \text{ psi}$$

The rear cover and the divider experience low stresses. The structure is adequate for its intended purpose.

5.3.2.4 Deflections Due to Aerodynamic Forces

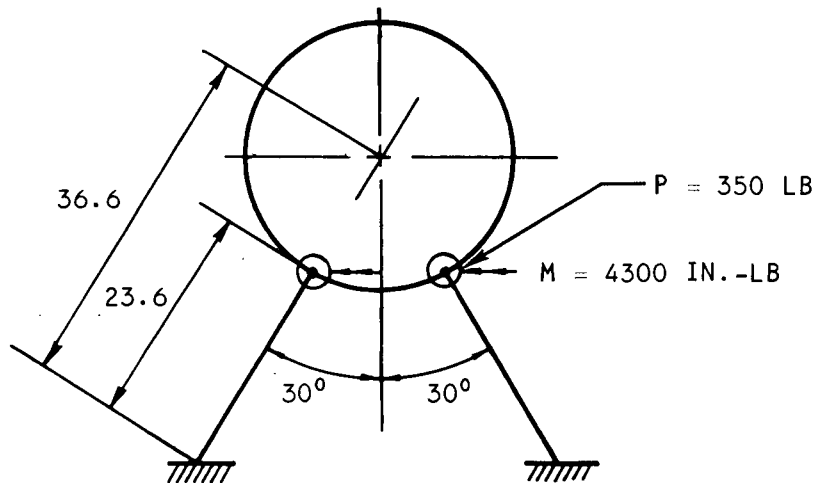
The loads on the various component parts of the assembly have been given in paragraph 5.3.2.1. The total probe axial load is $50 \times 10 = 500$ lb. The total load on the ring is 200 lb. For the legs, a load of 125 lb is applied to each leg. A simplified approach has been taken to estimate deflections of the probes located at the top of the ring. The load acting on six of the ten probes plus one-half of the total load on the ring was assumed to act at the top of the ring. This will give a calculated deflection that will exceed the actual case. The structure and the assumed loading is shown below.



The ring structure above the legs was assumed to be rigidly built into the legs. The deflections at the probe tips were then determined from the individual contributions of the legs and the ring structure.



The legs are loaded as cantilevers, and the end rotations of the legs at the juncture to the full ring will contribute to probe tip radial deflection. The moment of inertia of each leg was determined to be 18.1 in.⁴. The loading on each leg is depicted below:



S-62080

The bending load on each leg is $M_b = M \cos 30^\circ = 3730 \text{ in.-lb.}$

The rotation of the leg due to this loading is

$$\theta_{\text{leg}} = \frac{M_b l}{EI} + \frac{Pl^2}{2EI}$$

where

$$l = 23.6 \text{ in.}$$

$$E = 28 \times 10^6 \text{ psi}$$

$$I = 18.1 \text{ in.}^4$$

$$\theta_{\text{leg}} = \frac{(3730)(23.6)}{(28 \times 10^6)(18.1)} + \frac{(350)(23.6)^2}{(2)(28 \times 10^6)(18.1)} = 0.000174 + 0.000192$$

$$\theta_{\text{leg}} = 0.000366 \text{ radians}$$

The radial upward displacement at the probe tip is

$$\delta_{\text{Probe}} = 11.5 \theta_{\text{leg}} \cos 30^\circ = 0.0036 \text{ in.}$$



AIRESEARCH MANUFACTURING COMPANY
Los Angeles, California

Next the ring deflection was determined. The 150-deg arc length of the ring from the junction at the leg to the top of the ring was analyzed for rotations due to a unit concentrated force and a unit moment applied at the top of the ring. The ring properties of concern in this out-of-plane ring analysis were the section inertia in bending and the torsional inertia property. These were computed and found to be

$$I_{\text{bending}} = 19.1 \text{ in.}^4$$

$$I_{\text{torsion}} = 2.35 \text{ in.}^4$$

The ring rotation due to a unit force of 100 lb at the top of the ring was found to be

$$\theta_{\text{ring}} = 0.00048 \text{ rad/100 lb}$$

For a concentrated load of 400 lb shared by both sides of the ring, the rotation is

$$\theta_{\text{ring}} = 0.00072 \text{ rad}$$

For a unit moment of 100 in.-lb, the rotation at the attachment point was found to be

$$\theta_{\text{ring}} = -0.000053 \text{ rad/100 in.-lb}$$

Due to the total moment of 900 in.-lb shared by both sides of the ring, the ring rotation would be

$$\theta_{\text{ring}} = -0.00024 \text{ rad}$$

The net rotation due to ring deflection is 0.00048 rad, which would lead to a radially outward deflection at the probe tip

$$S_{\text{probe}} = (11.5)(0.00048) = 0.0056 \text{ in.}$$

The total probe deflection is $0.0036 + 0.0056 = 0.0092 \text{ in.}$, which is well within the permissible limit of 0.050 in.

5.3.3 Discussion of Results

Many other detailed aspects of the design were studied and analyzed. These were found to be satisfactory. The structure is therefore entirely satisfactory from the standpoint of structural adequacy for stress and rigidity.

5.4 SUMMARY OF HRE/AIM ERROR ANALYSIS

An analysis of the probable errors to be encountered in the determination of the performance parameters from tests of the HRE/AIM engine was completed. (Reference document AP-70-6216). The following summarizes the results obtained from the analysis performed.



5.4.1 Selected Approach to AIM Measurements

A study was completed of potential methods for determining the individual component performance of the inlet, combustor, and nozzle, as well as the overall engine performance. In general, more than one method of component performance evaluation is available. One way to establish component performance levels is to use subscale component efficiencies obtained during AIM configuration development tests; however, certain aspects of the flow were not simulated in the subscale tests. Differences between subscale and AIM test parameters which may be significant include inlet wall temperature ratio, combustor entrance flow profile, and nozzle kinetics. For these reasons, determination of component performance by direct AIM measurements is desirable wherever feasible.

The approaches selected for performance evaluation are indicated in Table 5-6. A continuity-momentum concept has been selected for calculating component performance. This method is based on the momentum theorem whereby the momentum flux at the downstream station of an appropriate control volume is evaluated from the entering momentum and the wall forces. The wall forces include a pressure-area term which is computed from measured wall static pressures and wall friction, which is calculated.

The overall engine performance is evaluated from the equation indicated on the chart. This equation shows that the load cell reading is corrected for (a) external drag on the metric portions of the engine which is comprised of a measured wall pressure force and calculated skin friction, and (b) the force exerted on the engine by the pressure in the cavity between the metric engine and the fixed portion of the cowl acting on a projected area. This latter force can be obtained through static calibrations. Both of these corrections act to reduce the load cell reading and, therefore, their values are added to the load cell force.

The airflow meter will require calibration testing to determine its discharge coefficient.

5.4.2 Measurements Required for Selected Approach

The measurements required to evaluate AIM performance are indicated in Table 5-7 together with the probable error calculated for each quantity. Some of the quantities shown are measured directly, such as load cell reading, but the bulk of the items in the table are derived quantities such as wall pressure force and heat rejection.

It should be noted that the component analyses were carried out in parallel so that some of the quoted errors, for example the airflow error shown for the combustor, are preliminary estimates and may not agree from one component to the next with the final errors shown on Table 5-7. The errors for each given component, however, are consistent between this and Table 5-7. In general, the preliminary estimates turned out to be conservative in magnitude.

It can be seen that the errors range over two orders of magnitude from 0.2 percent for inlet wall pressure force and flowmeter throat area, to 20 percent



TABLE 5-6

SELECTED APPROACH TO AIM MEASUREMENTS

COMPONENT	APPROACH
INLET	MEASURE WALL PRESSURE FORCE AND CALCULATE WALL FRICTION--CONTINUITY- MOMENTUM CONCEPT
COMBUSTOR	
NOZZLE	
OVERALL ENGINE	$T_i = F_{\text{LOADCELL}} + D_{\text{EXT.}} + F_{\text{CAVITY}}$
AIRFLOW METER	DIRECT CONNECT AND TUNNEL CALIBRATION



TABLE 5-7

MEASUREMENTS REQUIRED FOR SELECTED APPROACH

AIM COMPONENT	QUANTITIES REQUIRED	PROBABLE ERROR %		
		M = 5	M = 6	M = 7
INLET	FREESTREAM MOMENTUM	3.7	3.3	3.2
	WALL PRESSURE FORCE	0.2	0.2	0.2
	INLET AIR FLOW	2.9	2.5	2.5
	INLET HEAT REJECTION	10.0	10.0	10.0
COMBUSTOR	FREESTREAM TEMPERATURE	1.5	1.5	1.5
	AIR FLOW	5.5	5.5	5.5
	HEAT REJECTION	20.0	20.0	20.0
	FUEL FLOW	1.0	1.0	1.0
	I_{VAC}	2.7	3.2	4.5
NOZZLE	IDEAL MOMENTUM	3.8	4.1	5.2
	WALL PRESSURE FORCE	1.9	1.9	5.0
	WALL FRICTION	20.0	20.0	20.0
ENGINE	LOAD CELL FORCE	0.5	0.5	0.5
	STATIC PRESSURE	0.5	0.5	0.5
	FUEL FLOW	1.0	1.0	1.0
	EXTERNAL FRICTION	20.0	20.0	20.0
AIRFLOW METER	DISCHARGE COEFFICIENT	1.6	1.5	1.5
	THROAT AREA	0.2	0.2	0.2
	THROAT PRESSURE	0.8	0.7	0.6
	TOTAL TEMPERATURE	2.1	1.8	1.8



assumed for frictional forces and combustor heat rejection. Not all of the percentage errors shown are used directly in the root-sum-square calculation of overall component error, presented in Table 5-7. For example, at Mach 5, the 20-percent error shown for nozzle friction is equivalent to a 40-lb thrust error, whereas the 1.9-percent error in the wall pressure integral corresponds to 35-lb thrust at Mach 5. In other words, a given error shown in this table is given as a percentage of the nominal magnitude of the variable itself. Appropriate weighting factors must be applied to each before taking the root-sum-square error.

5.4.3 Summary of AIM Error Analysis Results

Table 5-8 presents a summary of the probable errors predicted for the performance parameters of interest. Inlet kinetic energy efficiency had the smallest uncertainty (± 1.3 percent) while inlet pressure recovery had the largest (± 30.5 percent) error. This seeming contradiction merely points up the relative sensitivity of these two parameters; the two errors are, in fact, consistent with one another. This is also true for combustor chemical efficiency and total pressure recovery as compared with combustor effectiveness.

The dual ranges shown at Machs 6 and 7 for mass flow ratio are related to the calibration of the airflow meter. The lower number is based on a static calibration while the larger error is based on a two-point wind tunnel calibration. As mass flow errors influence many other errors, this comparison shows the importance of a careful static calibration of the airflow meter.

Although some of the probable errors in component performance are rather large, it is heartening to note that the errors in overall engine thrust coefficient and specific impulse are quite acceptable as they range from 2.3 to 4.6 percent for an equivalence ratio of unity.

5.5 SUMMARY OF TEST PROGRAM

A total of 41 test runs are proposed for the AIM in the NASA wind tunnel facility. Typically, four to six stabilized data points will be obtained during each blow; thus, the program will provide approximately 200 separate data points. The proposed breakdown of these runs is presented in the adjacent chart. The philosophy of running all tests at a given Mach number before changing tunnel Mach number has been followed in establishing the run schedules.

The Mach 6 tests are scheduled first. The first test will be a checkout at Mach 6 with no fuel injection. The next three runs will yield inlet pressure recovery and mass flow data for Mach 6 (airflow meter installed). Following these initial four runs, the airflow meter will be removed and the combustor exit probes will be installed. There are seven runs designed to optimize supersonic combustion fuel injection schedules at the design spike position. These runs are also used to investigate the influence of angle-of-attack variation of fuel flow schedules. This is followed by three runs to examine inlet-combustor stability with varying spike positions. One run has the principal objective of gas sampling and profile investigations at the combustor exit for subsonic combustion, although these measurements are taken during many other runs during supersonic combustion tests. At the completion



TABLE 5-8

SUMMARY OF AIM ERROR ANALYSIS RESULTS

PARAMETER	ERROR $\sim \pm \%$		
	M = 5	M = 6	M = 7
INLET MASS FLOW RATIO	2.1	1.9-3.2	1.9-3.2
INLET PRESSURE RECOVERY	26.5	27.9	30.5
INLET KINETIC ENERGY EFFICIENCY	2.0	1.6	1.3
INLET PROCESS EFFICIENCY	8.9	7.9	7.2
COMBUSTOR CHEMICAL EFFICIENCY	8.0	11.6	20.3
COMBUSTOR EFFECTIVENESS	—	4.2	5.4
COMBUSTOR TOTAL PRESSURE RECOVERY	—	13.0	24.6
NOZZLE KINETIC ENERGY EFFICIENCY	1.8	1.8	1.8
NOZZLE PROCESS EFFICIENCY	21.0	14.0	11.0
INTERNAL SPECIFIC IMPULSE	2.5	3.3	4.6
INTERNAL THRUST COEFFICIENT	2.3	3.1	4.5



of fuel schedule and stability testing, the combustor exit probes are to be removed and the nozzle spike and shroud will be installed. Five runs are scheduled to determine the overall engine performance at Mach 6 as a function of combustion mode, angle of attack, and altitude.

The Mach 7 wind tunnel nozzle is to be installed after the first 20 blows. The Mach 7 test program is similar to the Mach 6 program outlined above but with four fewer data runs.

After completing 35 runs, the Mach 5 wind tunnel nozzle will be installed. The test plan again is similar to that for Machs 6 and 7, but condensed to six test runs.

Table 5-9 summarizes the number of tests and objectives of the test run for each of the test conditions specified.





TABLE 5-9

SUMMARY OF PLANNED TESTS FOR AIM

MACH NO.	5			6			7			TOTALS
	NONE	SUB-SONIC	SUPER-SONIC	NONE	SUB-SONIC	SUPER-SONIC	NONE	SUB-SONIC	SUPER-SONIC	
COMBUSTION MODE										
CHECKOUT				1						1
INLET PERFORMANCE AND AIRFLOW CALC	1			3			3			7
FUEL INJECTION OPTIMIZATION						7			6	13
INLET COMB STABILITY			2		1	3			3	9
ENGINE PERFORMANCE		1.5	1.5		1.5	3.5			3	11
TOTALS	1	1.5	3.5	4	2.5	13.5	3		12	41
	6			20			15			

S-62089

6. DESIGN AND FABRICATION

6.1 DESIGN

Design effort was directed towards designing (1) the combustor exit instrumentation assembly, (2) a mechanical joint for the spike assembly support cone assembly, (3) a five-element temperature rake assembly for the air metering duct, and (4) in support of fabrication.

6.1.1 Instrumentation Assembly

Two designs were considered for the instrumentation assembly. One consisted of fabricating the instrumentation mount assembly from sheet metal, and the other was to manufacture this assembly from forged rings and bars. Fabricating the instrumentation mount assembly from sheet metal appeared to be the best approach; however, analysis indicated that even with extensive fixturing it would be difficult to meet dimensional requirements, so this unit was fabricated from forged rings and bars. The advantages of this approach were:

- (a) fewer welded joints were required
- (b) the problem of shrinkage and distortion related with welding of thin sections was reduced
- (c) the amount of tooling required to fabricate this unit was minimized.

6.1.2 Mechanical Joint for the Inlet Spike

A mechanical joint was designed for attaching the support cone (AiResearch Drawing 950512) to the inlet spike. A mechanical joint was selected, in lieu of welding, to avoid possible distortion and alignment problems between the cone and the spike.

6.1.3 Temperature Rake

The design for the five-element temperature rake was initiated. The purpose of the rake was to obtain the temperature profile of the hot gas entering the airflow metering section.

6.2 FABRICATION

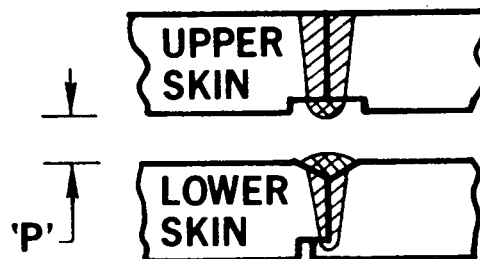
Fabrication of the AIM hardware has progressed satisfactorily. The difficulties encountered and resolved were basically associated with welding Nickel-200 sections to itself and to other metals. Report AP-70-6740, 17 September 1970, summarizing the problems associated with welding and various techniques employed to resolve the problems encountered has been prepared and



was submitted under separate cover.

The following is a summary of the problems encountered during fabrication of the AIM hardware.

- (a) The basic problem associated in E-B welding Nickel-200 to Nickel-200, and Nickel-200 to any other material was the effect of the magnetic field present in the nickel, or induced in the nickel by the beam current, causing the electron beam to deflect from its targeted position, resulting in an incomplete weld. Various techniques and Mu-metal shields were tried to preclude the problem. Each technique minimized the amount of deflection; however, it did not eliminate the problem.
- (b) In addition to standard inspection techniques utilizing X-Ray and dye check, development of shear-wave ultrasonic inspection was necessary. Tests revealed that during the solidification process, the shrinkage of the molten nickel would pull the incompletely welded joint together so tightly that resolution available by X-Ray technique would not reveal incomplete welds.
- (c) During fabrication of the spike assembly it was necessary to E-B weld two skins simultaneously. Weld samples indicated that weld schedules could be developed such that the droplets from the upper skin and buildup from the lower skin would not block passage "P" shown below.

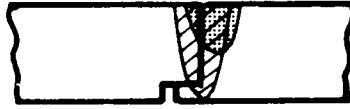


Tests revealed that the weld schedule was very sensitive to the height of passage "P". Tests also revealed that joints previously joined by the above described method could not be rewelded by the shoot-thru method.

- (d) Excessive porosity was experienced whenever air-melted Inco, or air-melted Hastelloy was E-B welded to air-melted Nickel.
- (e) The high energy requirements necessary to weld copper sections of any appreciable thickness presented great difficulty in E-B welding of copper. Also, experience revealed that whenever small sections of copper were welded, weld schedule was affected by the heat absorbed during the welding process, resulting in the necessity to make adjustments during the welding process.



- (f) During E-B welding of Nickel-200 to copper it was noted that slight deflection of the electron beam greatly affected the quality of the welded joint as per the following Figure.



6.2.1 E-B Welding of Nickel to Nickel

In general, the main problems encountered in E-B welding of nickel to nickel were electron-beam deflection off the joint, and, on occasions, porosity of the weld.

Two kinds of beam deflection were incurred. The first was an offset of the beam from the joint when the electron beam was first started. This deflection was easy to compensate for by simply moving the beam back onto the joint after the welding process had been started. This initial deflection of the beam is attributed to the magnetic field created by the beam current in the nickel. The second deflection problem encountered was a waving of the beam over the joint as the welding progressed. This waving of the beam was sufficient, in many instances, to create a mis-weld of the part. In addition, waving of the beam resulted in improper penetration of the weld joint. The waving of the electron beam was finally attributed to residual magnetic fields in the nickel. This assumption was verified by degaussing of the nickel parts prior to welding. Degaussing of the parts significantly reduced the amount of beam waving during welding. It was learned that the welding process was very sensitive to this residual magnetism. The general practice of using a compass as a means of detecting residual magnetic variations was adopted. It was not necessary to totally demagnetize the parts, but just to ensure that the residual magnetism was constant or uniform. Demagnetization of the parts was accomplished by the use of a large ac coil.

The occurrence of porosity in the weld appeared to be on a random basis. It was not until later in the program during welding of nickel to other nickel alloys that it was concluded that the porosity could be attributed to inclusions in the metal. In particular, it was concluded that air-melted metals were more susceptible to porosity. It was also noted that less porosity was encountered with nickel plates than with nickel forgings. This led to the assumption that the forging process was contaminating the metal and providing inclusions. The problem of random porosity in the weld joints was never fully resolved.

6.2.2 E-B Welding of Copper to Copper

The AIM design was such that in the copper-to-copper weld joint little or no blow-through could be tolerated on the backside of the weld. Tests were conducted in an attempt to determine a weld schedule which would produce a satisfactory copper-to-copper weld while minimizing the blow-through or splatter on the back of the joint. Section thicknesses to be welded were in the order of 0.2 in. Compared to the nickel and steels that were being E-B welded, copper required a much higher energy per unit length of weld for the same section thickness. This additional energy requirement was attributed to the higher thermal conductivity of the copper. Using the required high-energy weld levels



on copper consistently resulted in high incidence of metal expulsion, accompanied by porosity, in the weld zone. The metal expulsion observed was attributed to either impurities in the copper or possibly boiling of the copper in the weld zone. No satisfactory method of solving the expulsion problem was apparent, so further consideration of E-B welding copper to copper was discontinued.

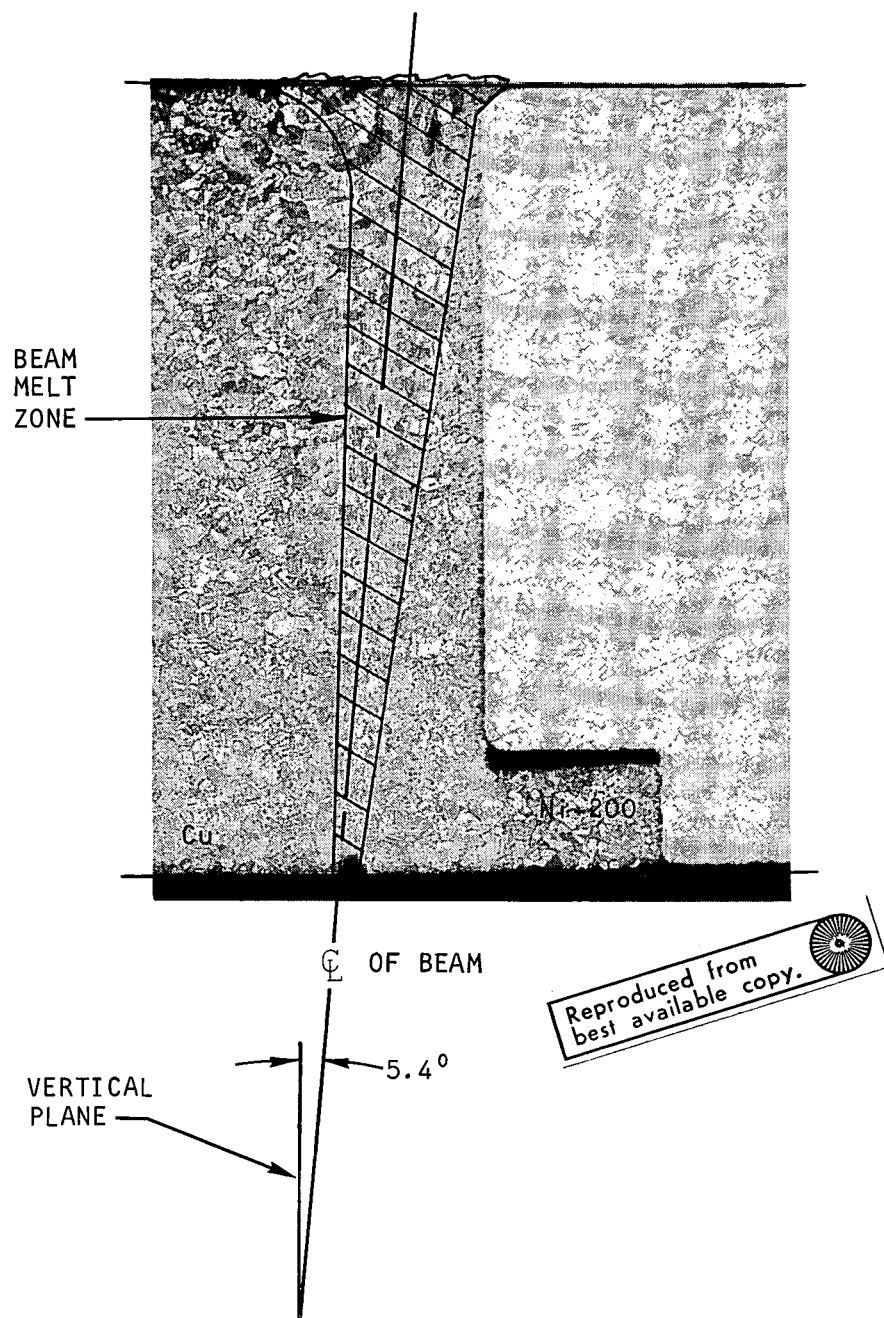
6.2.3 E-B Welding of Copper to Nickel

The major difficulty experienced in E-B welding of copper to nickel was beam deflection through the joint, as well as beam deflection off the joint. These beam deflections were related to two possible causes; (1) residual magnetism in the nickel, and (2) the "Seebeck", or thermocouple, effect.

Reference 6-1 indicates that the combination of copper and nickel results in a high electromotive force generation as a function of temperature. During welding, a temperature gradient is created along the weld joint. This temperature gradient gives rise to a voltage gradient which results in recirculation currents around the joints. It is conceivable that these recirculation currents are large enough to give rise to an electrostatic field which can deflect the electron beam. This electrostatic field, coupled with the one created by the beam current itself, now presents two possibilities for deflection of the beam. Tests were conducted on a "Sciaky" and a "Hamilton" welder to ascertain the validity of the above assumptions. A test was performed on a "Sciaky" welder using three magnetic compasses along each side of a copper-nickel weld joint. At the outset, the parts were demagnetized and the needles of the compasses were evenly aligned with magnetic North. At the initiation and for the duration of the weld, strong fields were registered by the compasses as evidenced by extremely rapid rotations of the needles around the axes. The needles continued to give small indications of residual magnetic fields after the welding was completed. Another observation of E-B deflection was noticed when using the Hamilton-Standard welder with the optical viewing system. When the beam was started on the copper-nickel joint, a deflection off the joint into the copper was consistently experienced. The deflections were corrected manually by the operator, who again directed the beam onto the joints and continued with the weld. For metal thicknesses of 0.5 in., the deflection was as much as 0.1 in. off the joint. Smaller metal thicknesses showed a correspondingly lesser deflection of the beam. In both tests, residual magnetism was removed before welding, which supports the assumption that the welding process itself creates electrostatic fields which interact with the beam location. In these tests it was not possible to determine the relative effects of the electrostatic fields created by the beam itself, or by the "Seebeck" effect.

One thing which was noticed, however, was that in the copper-nickel joints the electron-beam deflection occurred through the joint, as shown in Figure 6-1. The beam consistently deflected into the copper side of the joint. Since this phenomenon was not experienced in the nickel-to-nickel joint, one may then conclude that this additional deflection of the beam is attributable to the "Seebeck", or thermocouple, effect. One may further rationalize that the offset of the beam, since it is experienced in both the nickel-to-nickel joints and the nickel-to-copper joints, is related to the beam current itself.





F-12438

Figure 6-1. Internal Beam Deflection Into the Copper



AIRESEARCH MANUFACTURING COMPANY
Los Angeles, California

Two methods were found to give reasonably good corrections for beam deflections along the top-joint surface through the depth of the joint. One method tilts the part at an angle so the electron beam will favor the nickel; the other method offsets the electron beam into the nickel. Both correction methods are depicted in Figure 6-2.

Further efforts to reduce electron-beam deflections when welding copper to nickel involved nickel plating of the copper, which would give a nickel-to-nickel surface at the weld joint. Figure 6-3 shows weld zones that can occur for two plating thicknesses; namely, 0.06 in. and 0.01 in. Since plating bond strengths are much lower than welded joint strengths, it is necessary to include both the plating bond line and the joint in the weld zone. For thick nickel plating (0.06 in.), a wide weld zone is needed which results in excessive shrinkage. Thin nickel plating (0.01 in.) did not result in a significant change over the no-plating weld condition. These additional complications of nickel-plating the copper to improve copper-to-nickel E-B welding prompted a discontinuation of this approach.

A special case of magnetic field effects on E-B welding is encountered when a ring or cylindrical section is welded onto an internal surface. If the electron beam must pass near the top of the cylinder or ring, a beam deflection can result. The use of Mu-metal placed between the top surface of the part and the electron-beam path will shield the beam from most magnetic field effects (see Figure 6-4). Mu-metal is a nickel-iron alloy that has excellent magnetic shielding properties. Reference 6-2 provides detailed information on Mu-metal properties.

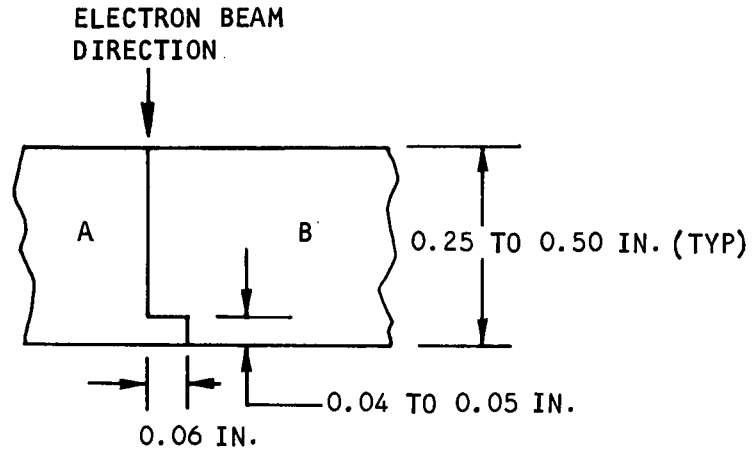
6.2.4 Explosive Bonding of Copper to Nickel

When E-B welding did not produce repeatable results for the bonding of copper to nickel, an investigation of explosive bonding was conducted. A detailed discussion of explosive bonding is presented in Reference 6-3. The concern in using explosive bonding was the feasibility of making the desired parts by this approach and the resultant joint efficiency. Both Battelle Institute (Columbus, Ohio) and E. I. duPont (Gibbstown, New Jersey) were contacted to determine whether they could supply the explosively bonded copper-to-nickel material. Consideration of schedule requirements led to the selection of duPont as the supplier. In order to evaluate the joint efficiency, a sample consisting of a 12 by 18 by 1 in. nickel plate bonded to a 12 by 18 by 1 in. copper plate was obtained from duPont. Tensile specimens were made from this plate. During operation of the AIM, the copper-nickel sections are subject to plastic deformation. Therefore, fatigue specimens were also made of the copper-nickel joints in order to evaluate the fatigue life. The results of the fatigue test are presented in Section 4. The tensile test indicated that explosive bonding provided an excellent joint, and the specimens always failed in the copper parent metal.

6.2.5 Porosity Problems in E-B Welding

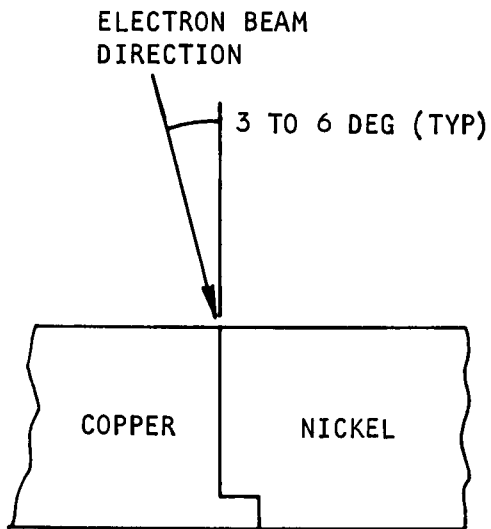
Porosity in the weld zone can be attributed to several conditions. Impurities in the joint area can cause porosity due to decomposition during the welding process. Reference 6-4 indicates that certain welding parameters can increase



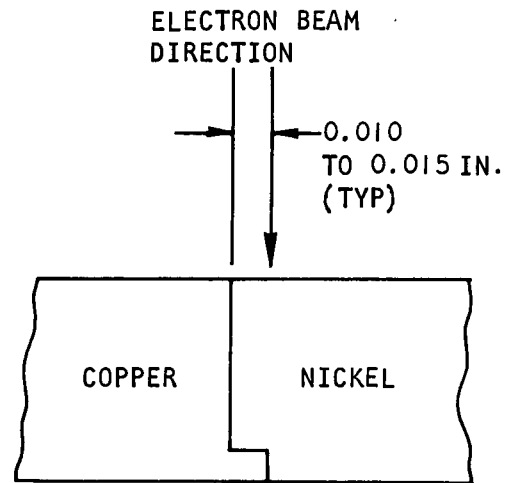


NOTE:

IF MATERIAL A AND MATERIAL B ARE DIFFERENT,
THE THERMAL CONDUCTIVITY OF MATERIAL A
SHOULD BE HIGH



ANGLE METHOD



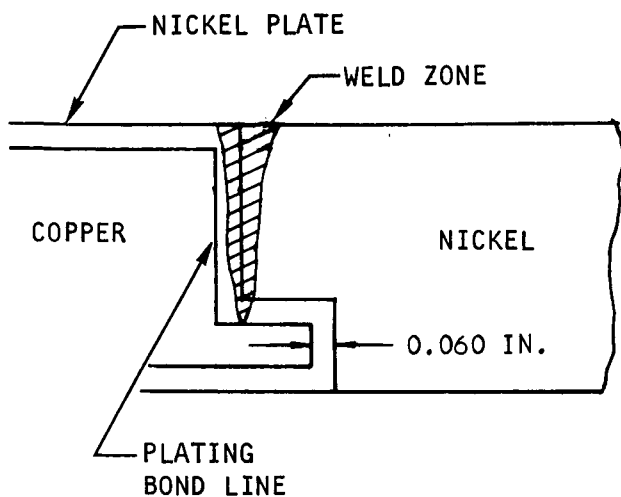
OFFSET METHOD

S-58323

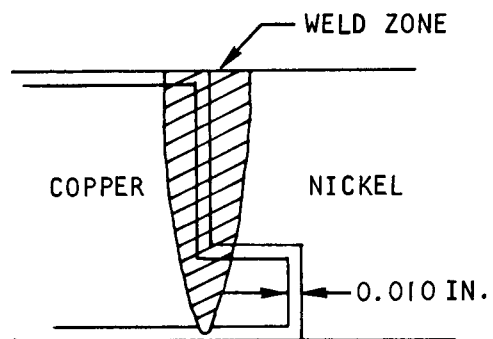
Figure 6-2. Weld Joint Correction Methods



AIRESEARCH MANUFACTURING COMPANY
Los Angeles, California



THICK-PLATING CONFIGURATION



THIN-PLATING CONFIGURATION

NOTE:

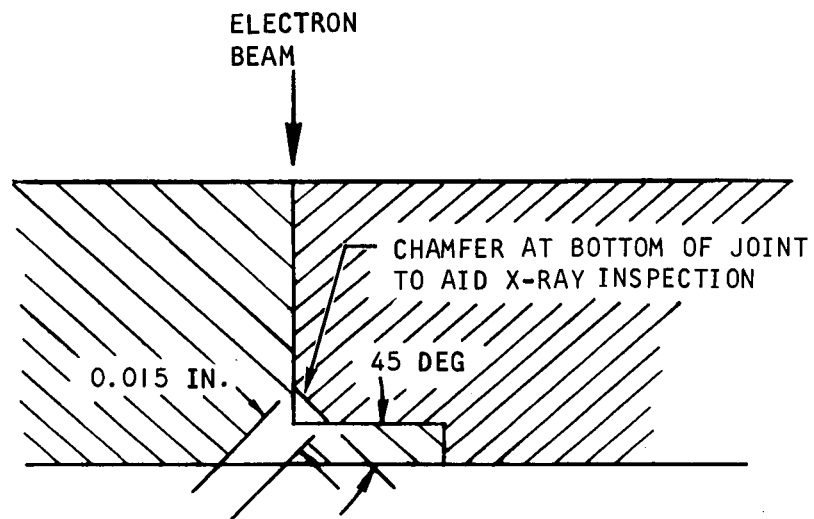
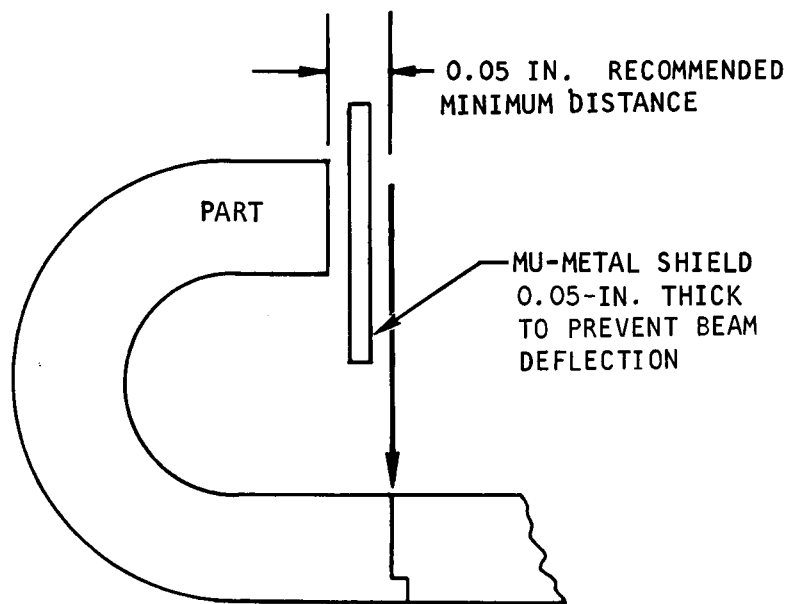
THE THICK-PLATING CONFIGURATION INDICATES A SERIOUS PROBLEM AREA IF THE WELD ZONE DOES NOT INCLUDE THE PLATING BOND LINE. THE JOINT STRENGTH IS DEPENDENT ON THE PLATING BOND STRENGTH, WHICH IS MUCH LOWER THAN THE WELD STRENGTH.

THE THIN-PLATING CONFIGURATION (APPROX. 0.010-IN. THICK) IS NOT SIGNIFICANTLY DIFFERENT THAN THE UNPLATED COPPER.

S-58324

Figure 6-3. Plating Effect on E-B Welding





S-58322

Figure 6-4. Utilization of Mu-Metal Shielding



porosity in copper E-B welds. If the porosity causes discussed therein could be related to boiling of the welded metal, then these causes might apply to metals other than copper.

Porosity problems were also encountered during the welding of Nickel-200 forgings, Inco 600, oxygen-free (OF) copper plate, and zirconium copper plate. There was very little occurrence of porosity when Nickel-200 plate was used for weld samples. Most of the actual hardware for the AIM engine were nickel forgings, which gave some indications of porosity. Inclusions from the forging process are suspected as a possible source of impurities. The use of Inco 600 was discontinued due to the extent of porosity experienced during E-B welding.

The excessive porosity and metal expulsion (undercutting) experienced during E-B welding of both OF and zirconium copper were a significant factor in the discontinuation of that approach.

It is believed that vacuum-melt materials should be investigated to determine if a reduction in impurity levels will reduce the porosity produced by E-B welding. Reference 6-4 indicates that the Atomic Energy Commission is conducting a study of various materials to obtain more information on E-B welding problems for different metals.

6.2.6 Overall Conclusions

Welding of nickel to nickel, when proper consideration is given to contamination and inclusion, produces an effective joint. In the welding of nickel it is important to demagnetize all parts prior to welding. It is necessary during the welding process to account for a beam offset created by electrostatic fields of the beam.

Electron-beam welding of copper to copper with section thicknesses of approximately one-quarter of an inch is not recommended.

Electron-beam welding of nickel to copper results in two beam deflections which must be corrected for. The first beam deflection is an offset which can be controlled by the operator. The second beam deflection is through the parent metal and appears related to the "Seebeck" effect. This deflection may be compensated for by tilting the part or the welding gun. Repeatable results could not be obtained in the welding of copper to nickel. Electron-beam welding of copper to nickel in thick sections and long joints is not recommended when very high joint efficiencies must be obtained.

Explosive bonding of copper to nickel produces consistent results and a weld joint that is stronger than the parent copper.

It is recommended that vacuum-melted materials be used when Inco 600 or Hastelloy X must be welded.



6.3 AIM COMPONENTS STATUS

6.3.1 Inlet Spike Assembly

All welding and brazing operations have been completed and the part is presently being contour-machined. During the fabrication period a number of difficulties were encountered. The difficulties were all associated with the metal-joining process, and changes in the design were necessary in order to facilitate manufacture of the spike assembly. The design of this unit also required welding both the outer and the inner shell simultaneously at three places. A development program was necessary to perfect this welding technique, and a separate report is being prepared, outlining the details of this program. The inspection of welded joints was also a problem since the resolution obtainable using normal X-ray methods was not adequate to detect flaws and missed welds. Ultrasonic inspection utilizing shear-wave technique was used in conjunction with normal X-ray and dye check methods. Shear-wave technique is not commonly used, and hence, a development program was also initiated to properly interpret the "C-scan" recording. Details of this development program are also being submitted in a separate report.

The basic problems of welding and of obtaining an adequate inspection of the joining process were applicable to all components manufactured.

Changes necessary on the spike assembly (to facilitate fabrication), such as incorporation of a mechanical joint at the intersection of the spike body section and its supporting cone is shown in AiResearch Drawing 950512, attached at the end of report.

6.3.2 Inner Shell Assembly (Figure 6-5)

Fabrication of the inner shell assembly was completed during this reporting period.

The problems encountered during the fabrication of this component, in addition to welding and associated inspection problems noted, were locating the strut sockets in the correct radial position. The error in angular position ranged from 0 deg, 30 sec to 0 deg, 7 min. The design of the engine requires that the strut sockets of the inner shell and the outer shell be positioned in accurate radial locations, hence the deviations from the theoretical position of the inner shell were transferred to the outer shell for match-machining.

6.3.3 Nozzle Plug Assembly (Figure 6-6)

Fabrication of this component was completed during this reporting period. The final contour was machined onto the component utilizing the electro-chemical grinding technique (ECG).

The problems encountered during the manufacture of this component were basically associated with the joining problem and inspection problem described previously.



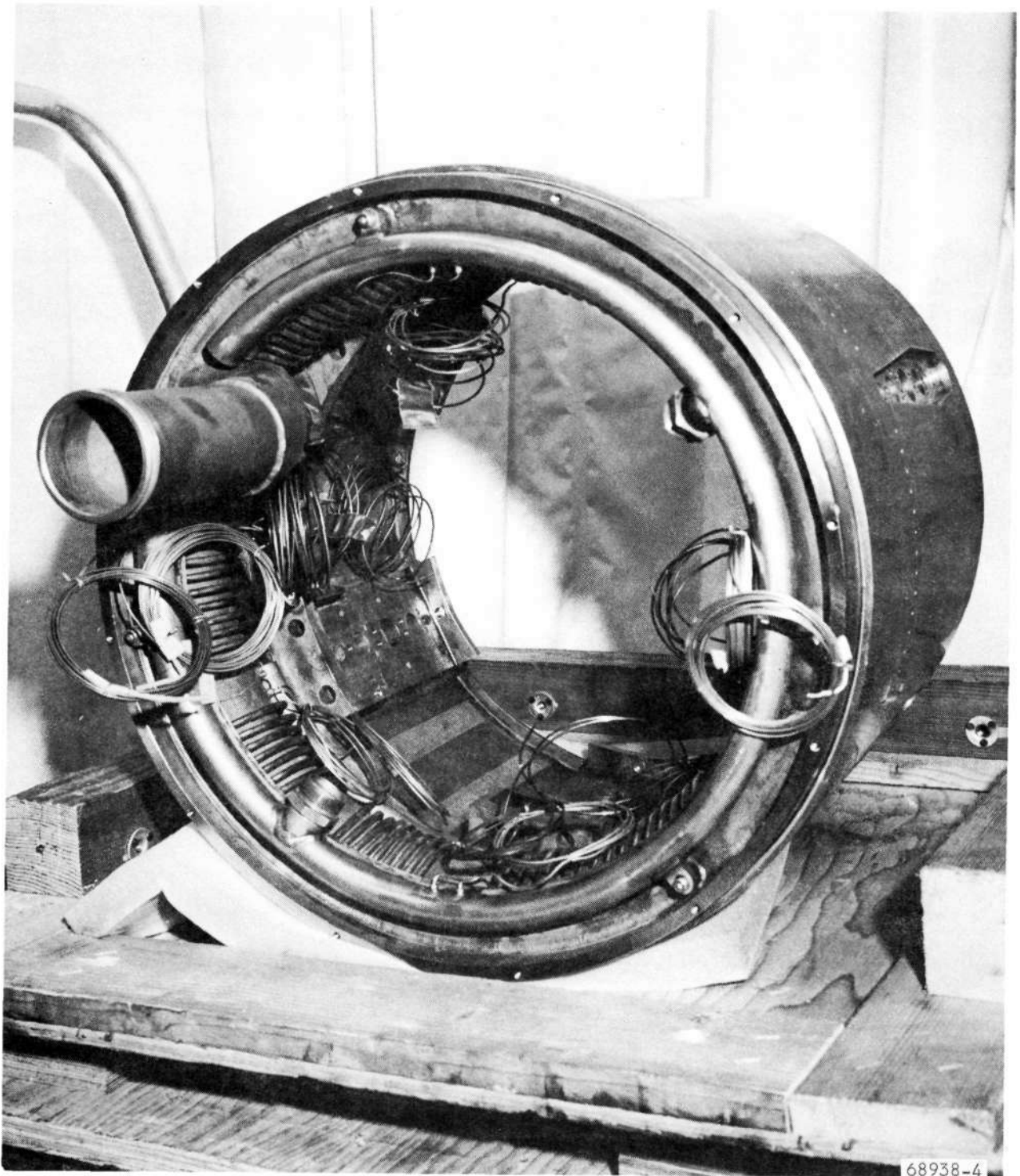
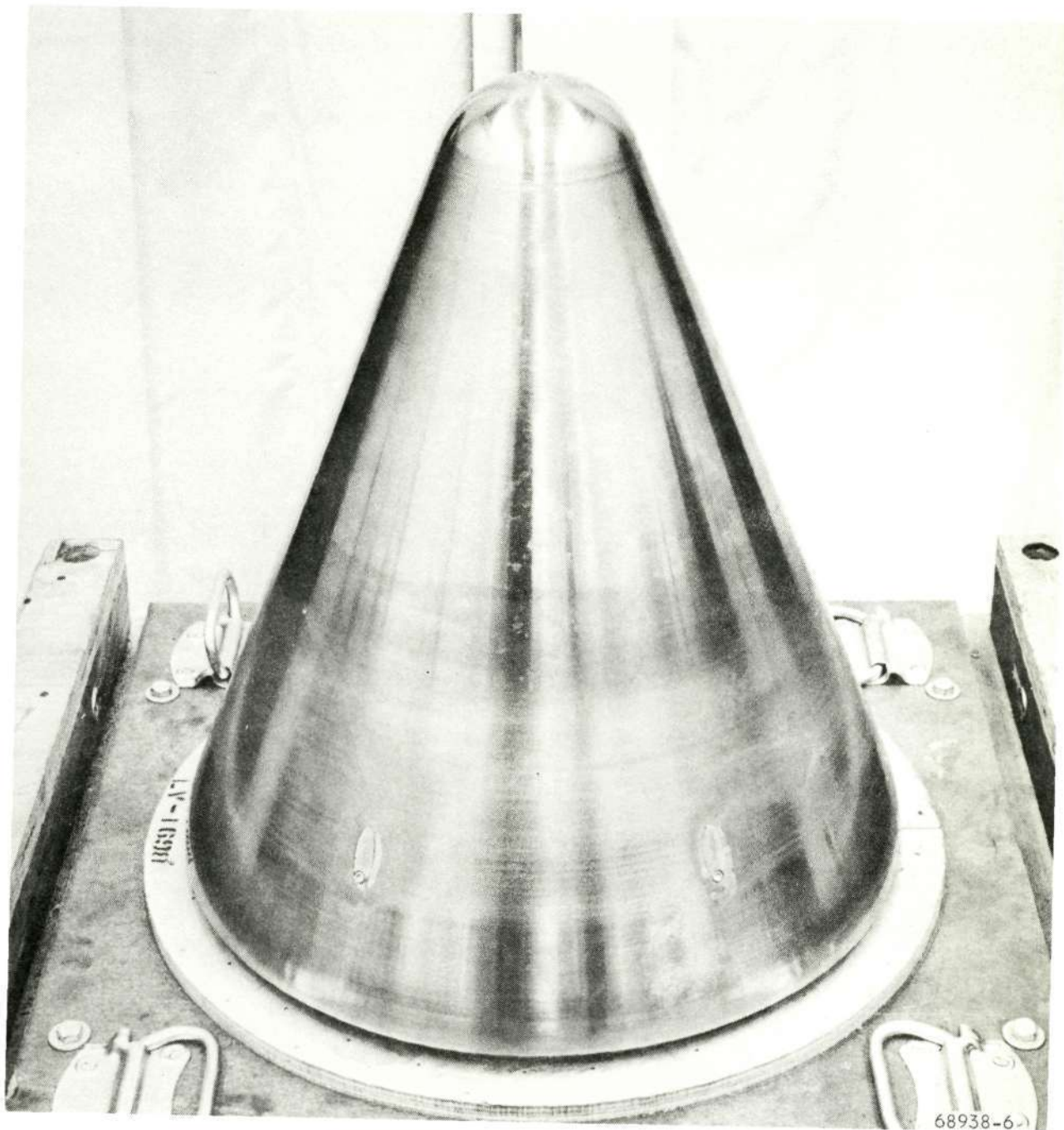


Figure 6-5. Inner Shell Assembly





68938-6

Reproduced from
best available copy.



Figure 6-6. Nozzle Plug Assembly



AIRESEARCH MANUFACTURING COMPANY
Los Angeles, California

6.3.4 Nozzle Shroud Assembly (Figure 6-7)

All welding and brazing operations on this component have been completed and the contoured section has been machined within 0.045 inches of its final contour.

The original design of this component required that the trailing edge be fabricated from OFHC copper. This requirement was set forth by heating experienced during test conditions specified for OAL. As noted previously, considerable difficulties were experienced in attempting to weld nickel to copper. Heat transfer analysis for the test conditions at Plumbrook indicated that nickel could be used; hence the fabrication of this component was completed with the use of a Nickel-200 trailing-edge section.

6.3.5 Outer Shell Assembly (Figure 6-8)

All welding and brazing operations have been completed on this component. Presently the strut sockets are being final-contoured, utilizing the electro-discharge machining (EDM) process.

Fabrication of this component is progressing satisfactorily.

6.3.6 Cowl Leading Edge Assembly

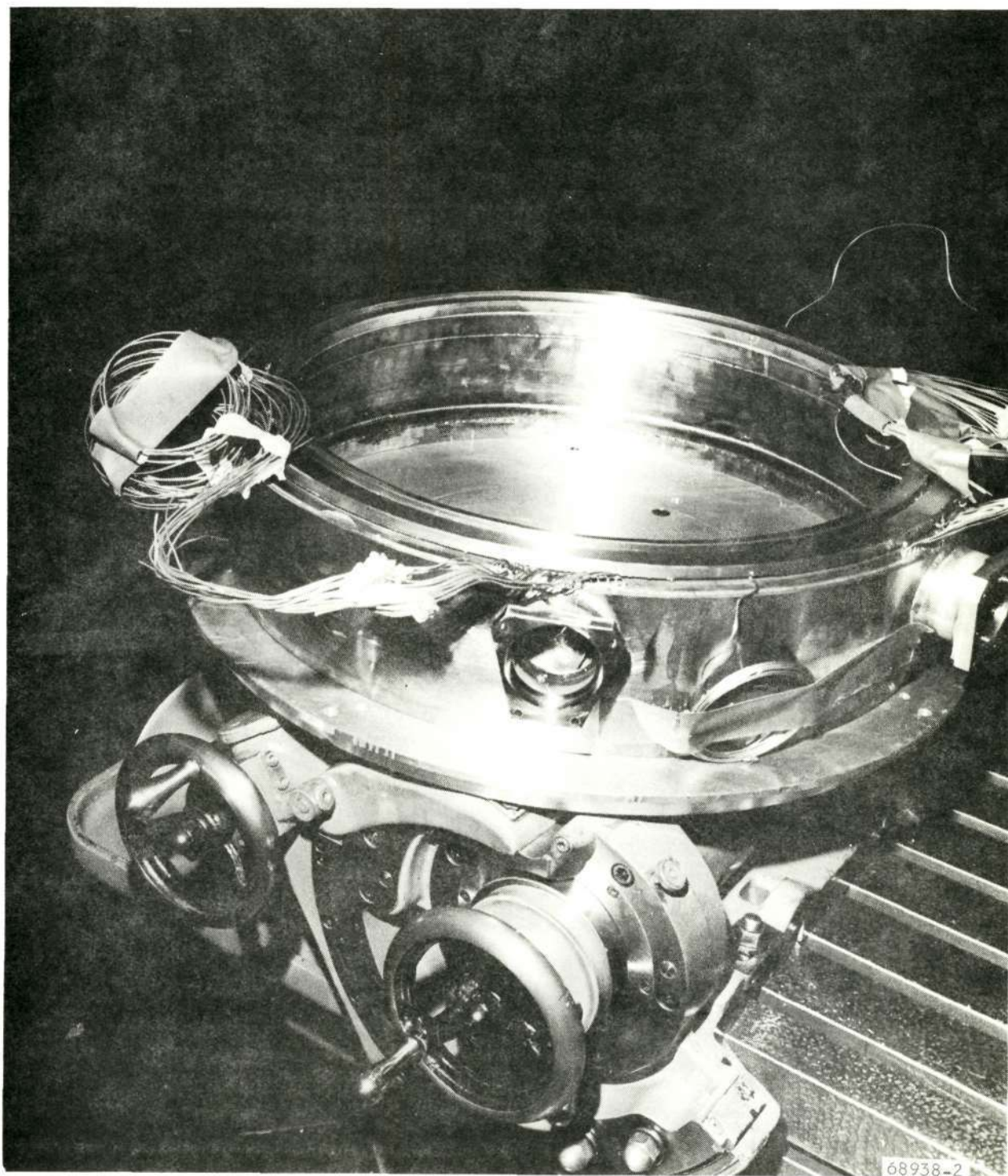
The fabrication of this component has been delayed as a result of two problem areas: (1) metal joining problems, and (2) maldistribution of the coolant flow through the parallel coolant passage shown in Figure 7-2 (see Section 7 of this report).

As discussed previously, considerable difficulties were experienced in attempting to weld copper to Nickel-200. Analysis of the test conditions at Plumbrook indicated that a nickel tip could be used for some of the test conditions specified at Plumbrook. Hence a decision was made that the initial cowl leading edge assembly would have a nickel tip, and a second tip would be fabricated with a copper tip and that this unit would be installed at the test site, if needed.

A parallel program to find an acceptable method to join copper to nickel was initiated. Electro-forming and explosive bonding was investigated. As discussed herein, explosive bonding appeared acceptable; however, data substantiating required physical properties of this joining process were not readily available so tests were performed to determine acceptability of this joining process for the AIM cowl leading edge structural requirements. Test results indicated acceptability of this joining method.

Coolant flow tests were performed on the nickel-tipped cowl leading edge tip section to ascertain that the coolant flow bypass-orifice configuration was as desired. Tests indicated that the pressure drop across this section was considerably higher than anticipated and indicated a maldistribution of the coolant. As a result, a development program to determine the cause of the high pressure drop was initiated.





68938-2

Reproduced from
best available copy.



Figure 6-7. Nozzle Shroud Assembly



AIRESEARCH MANUFACTURING COMPANY
Los Angeles, California

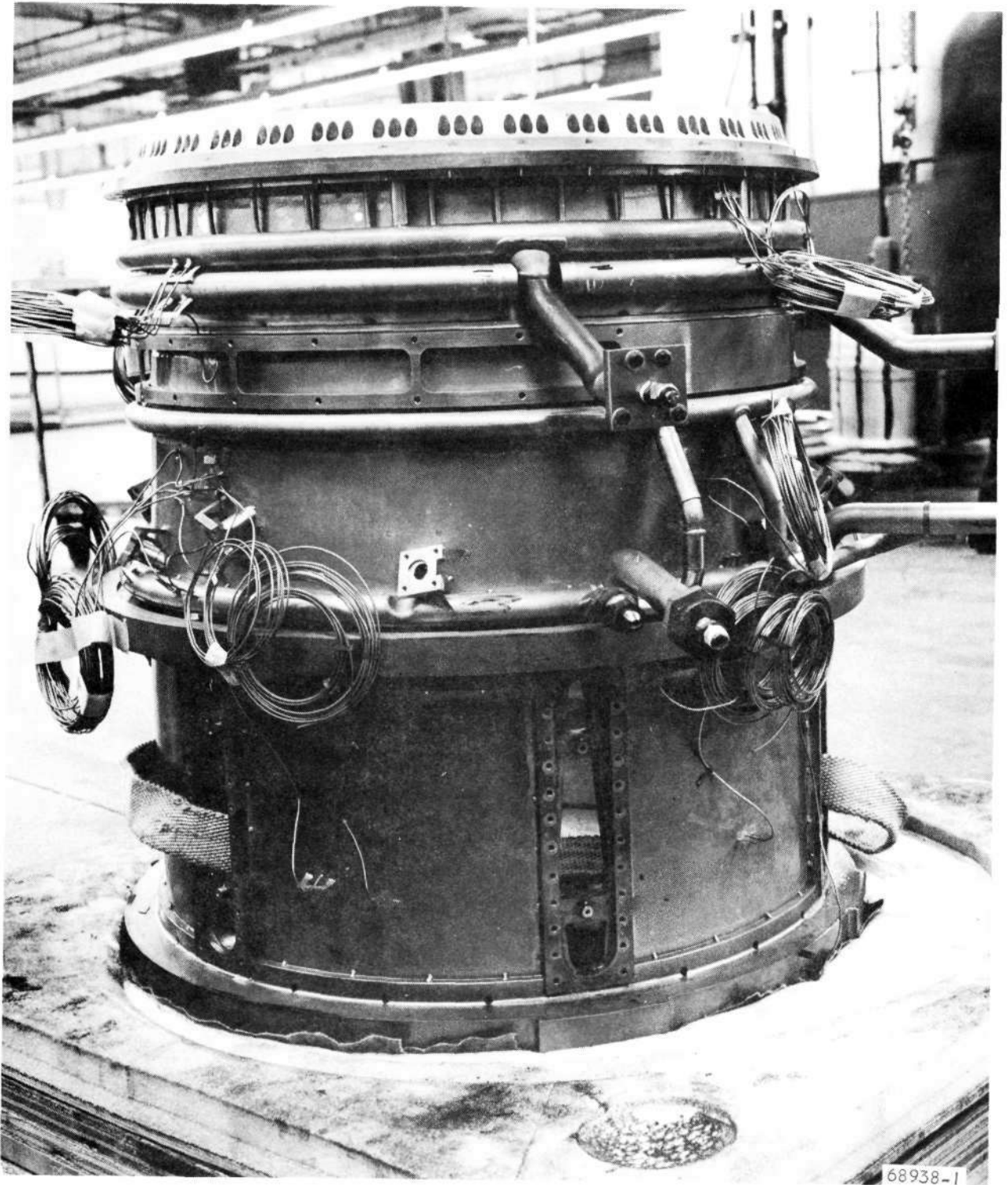


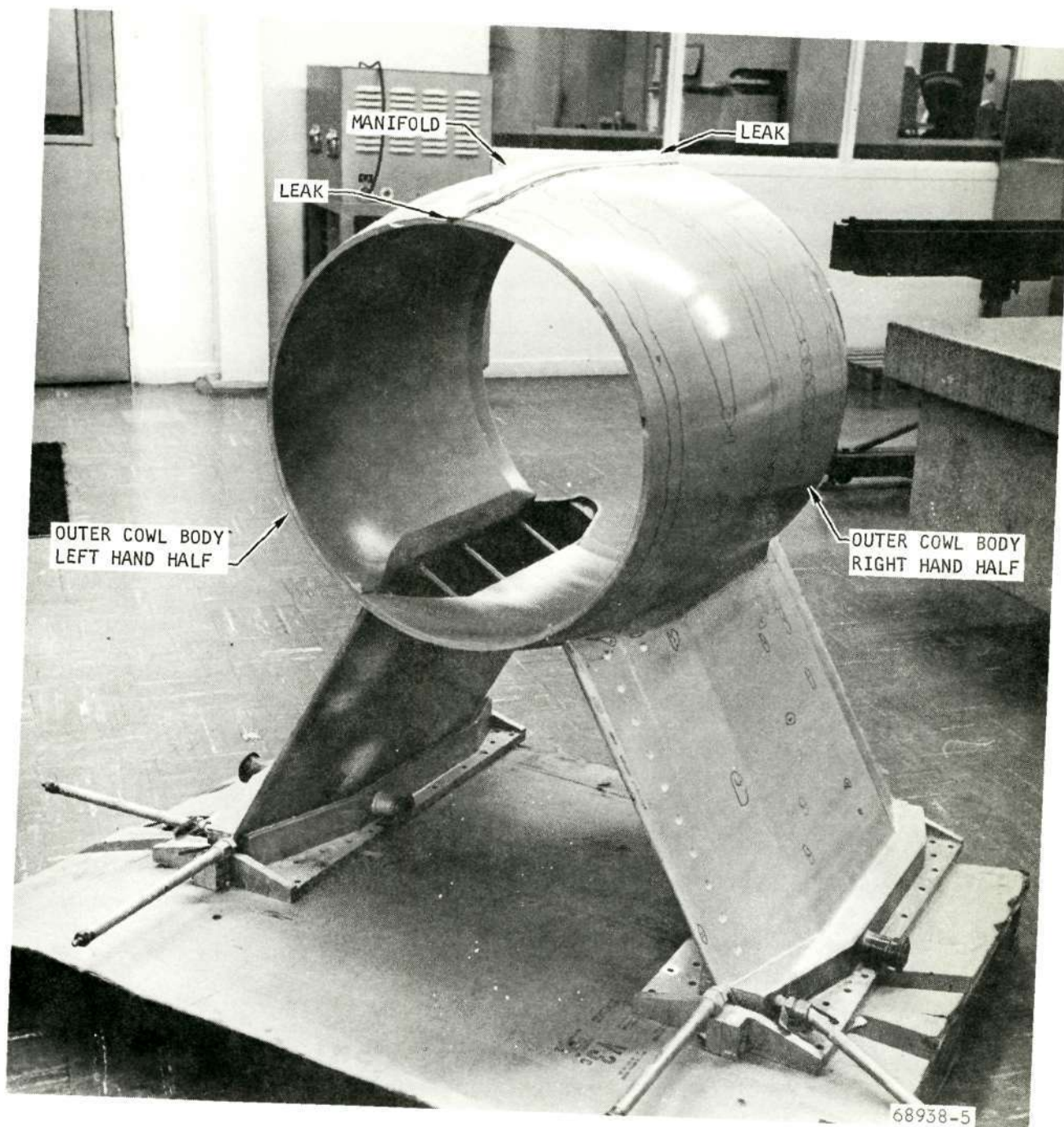
Figure 6-8. Outer Shell Assembly




6.3.7 Outer Cowl Body

The fabrication of this component has been completed. Pressure and Stress-Coat tests have substantiated its structural capabilities. During the pressure test, coolant was noted to leak excessively at the extremities of the interface of the outer cowl body and the coolant manifold (see Figure 6-9). Some leakage in this area can be tolerated during test of the HRE/AIM at Plumbrook; however, an effort to minimize the leak will be made.





Reproduced from
best available copy. 

F-12477

Figure 6-9. Outer Cowl Body



AIRESEARCH MANUFACTURING COMPANY
Los Angeles, California

7. TESTS

7.1 COWL LEADING EDGE COOLANT FLOW TESTS

The initial coolant flow test through the cowl leading edge tip section indicated that the pressure drop across this section exceeded the allowable limits and that possible maldistribution of the coolant flow was being experienced. Hence, the all-nickel cowl leading edge tip section scheduled to be assembled on SN 1 cowl leading edge was committed as a test item and additional pressure taps were installed. The results of testing this cowl leading edge tip section and a 10X-scale plastic model fabricated to visualize the coolant flow is described in this section.

7.1.1 Full-Scale Test

A full-scale cowl leading edge was pressure tapped and flow tested. Pressure taps were located at seven selected radial positions in such a manner as to measure the overall pressure drop, pressure drop approaching the tip, tip pressure drop, and the pressure drop across the fin (see Figure 7-1). The test configuration was similar to that shown in Drawing 950554 and in Figure 7-2 except that the intended slot length in the flow divider was foreshortened from 0.240 ± 0.010 in. to 0.137 ± 0.005 in., a reduction of 54 percent. The slots were shortened based on previous test results indicating a higher than expected tip pressure drop and also to add the flexibility of enlarging the bypass area in future rework. The flow divider support, Figure 7-2, is intended to overlap the slots 0.040 in., therefore leaving a design slot length of 0.097 in. Inspection of the test part revealed an actual slot length of 0.049 in. to 0.061 in., with 0.055 in. being typical due to a mislocation of flow divider, approximately 0.010 in. aft, and the flow divider support being too long. The net result was that the bypass slots were approximately 40 percent shorter than anticipated (72 percent shorter than the original design) and the leading edge flow passage approximately 20 percent larger than expected.

The unit was tested over a range of flow rates to the design flow of 660 gpm. At the design condition, an inlet water pressure of 220 psi was called for but due to facility limitations, the maximum achievable was approximately 130 psi. The location of the pressure taps 2 and 3 shown in Figure 7-1, were selected in a converging flow passage to provide a tip flowmeter. Figure 7-1 shows a plot of the overall pressure drop and the pressure drop between taps 2 and 3 as a function of inlet pressure P_1 . Tip pressure drops were erratic and some of the P_4 (station just aft of the fins) pressures were negative. Cavitation of the flow at high flow rates and modest inlet pressures was suggested by the data and it was verified by analysis that flow could cavitate under the test conditions of Figure 7-1. The analysis, based on Reference 7-1, indicated cavitation would



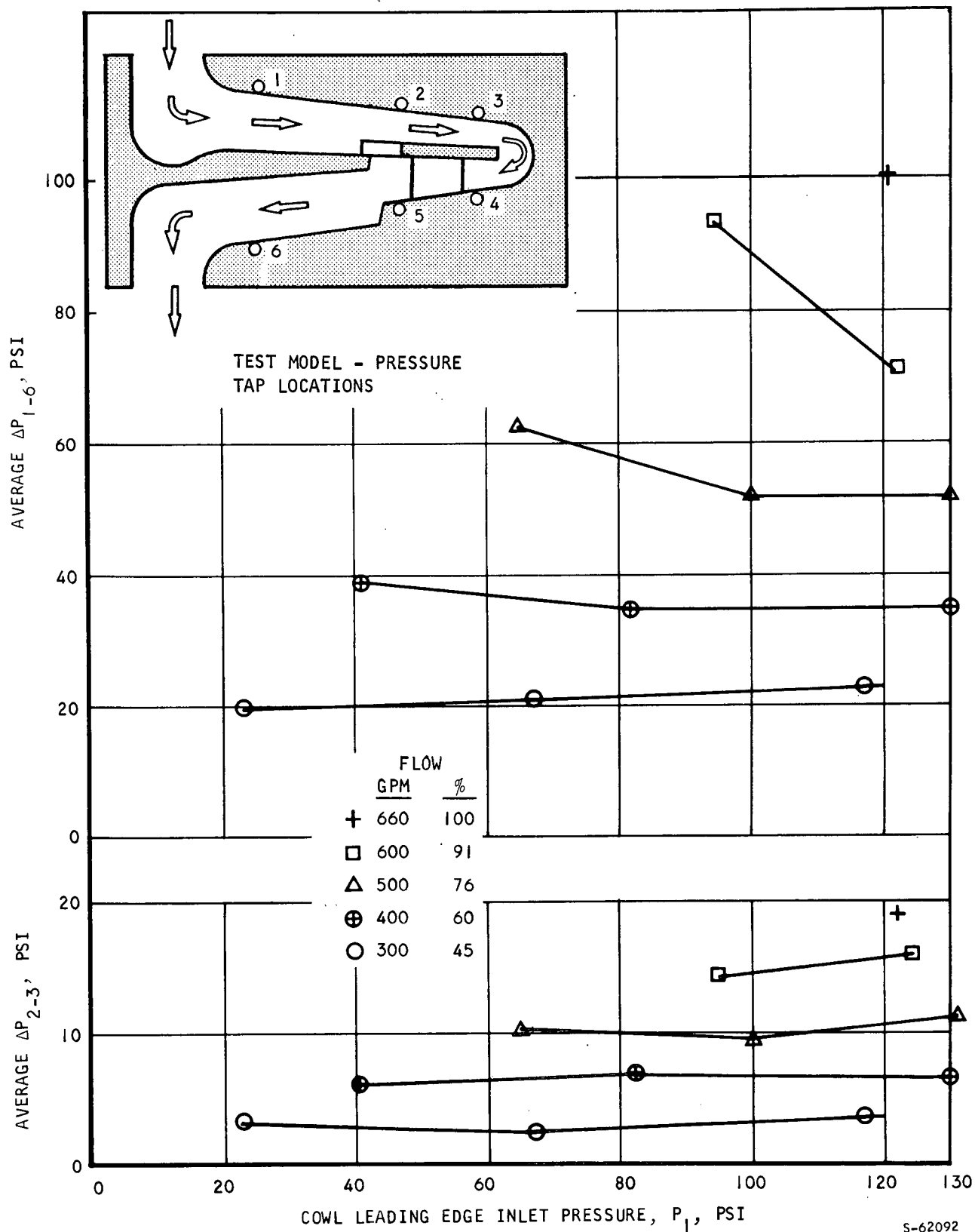


Figure 7-1. Full-Scale Cowl Leading Edge



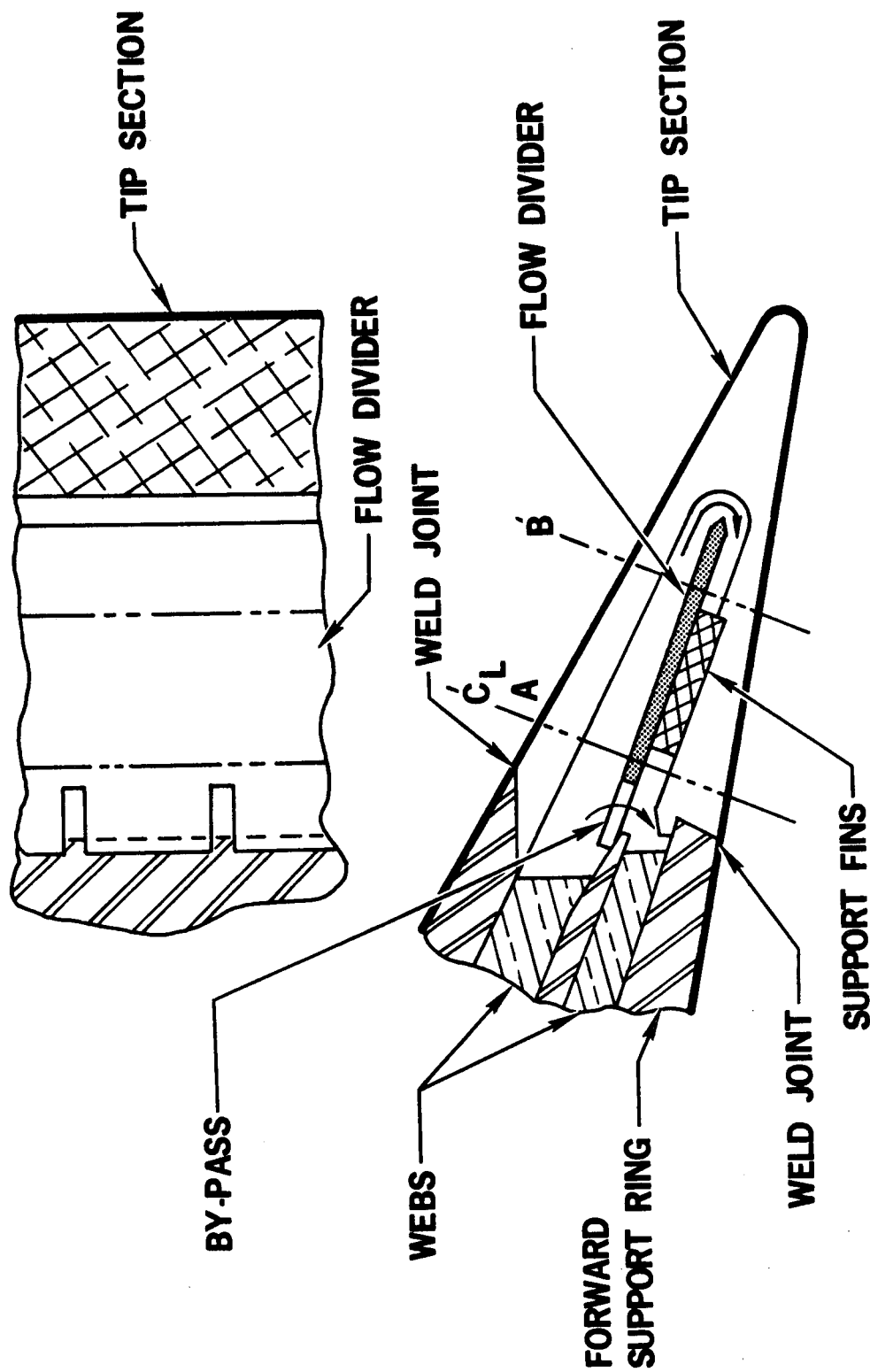


Figure 7-2. Cowling Leading Edge

occur below inlet pressures of 125 psi at 660 gpm and below 70 psi at 500 gpm. With the exception of the 660-gpm data point, the data shown in Figure 7-2 was cross-plotted at 120 psi and the results are shown in Figure 7-3. The analytically derived values of the relationship between the ΔP_{2-3} pressure drop and tip flow rate is also shown. The overall pressure drop (ΔP_{1-6}) was extrapolated to 82 psi at design flow and it was estimated that 75 percent of the flow was delivered to the tip and 25 percent bypassed. At 50 percent of design flow it was estimated that 70 percent of the flow was delivered to the tip section. It was therefore concluded that, in general, the excessive overall pressure drops were due to both cavitation and a poor flow split and detail interpretation of the data was not feasible due to the uncertainty associated with cavitation. It was further concluded that the design should be modified to make it less sensitive to manufacturing tolerances and to improve the efficiency of the flow passages.

7.1.2 10X-Scale Model Test

A 10X-scale model of the cowl leading edge was constructed of plastic to perform flow visualization testing and to investigate the relative merits of various flow-splitter configurations. The timing of these tests was such that early testing overlapped the full-scale tests. This model was instrumented in the same fashion as the full-scale model. The model was two-dimensional and represented 0.88 in. of the circumference of the full-scale cowl leading edge, i.e., the model width was 8.8 in. long. Figure 7-4 is a photo of the test set-up, and Figure 7-5 is a schematic diagram. The model has flow areas increased by a factor of 100 and velocities decreased by a factor of 10 which, based on scaling laws, should result in pressure drops reduced from full-scale by a factor of 100. Design flow for this model was 102 gpm. Cavitation was avoided due to the reduced velocities.

The model was constructed in a manner to permit insertion of various flow divider configurations. Figure 7-6 shows the flow divider designs that were tested. Configuration 1, no slots, was tested to obtain a flow calibration based on direct measurement of the water flow rate and the model ΔP_{2-3} pressure drop. This calibration was used to estimate the flow split between the tip and the bypass for subsequent splitter configurations. Figure 7-7 shows these data. The same analytical method of estimating the relationship between the tip flow and the ΔP_{2-3} pressure drop as was discussed previously was used to check the flow calibration and, as shown, the agreement was excellent.

The geometry of the second configuration was to duplicate that of the full-scale model and was constructed based on scaling of the intended full-scale dimensions. The slots were located so that observation from one side of the model showed a slot, and no slot on the other side resulting in an unsymmetrical configuration. A small amount of air was injected into the flow to permit flow visualization. Figure 7-8 shows the results of these observations. The separation of the flow in the tip region and the strong vortex flow in the bypass region increases the local velocities and therefore promotes cavitation in the full-scale design, although none was noted in the 10X-scale model testing. Figure 7-9 shows the resultant test data which indicated a flow split of approximately 72 percent flow to the tip at design flow. The overall (ΔP_{1-6})



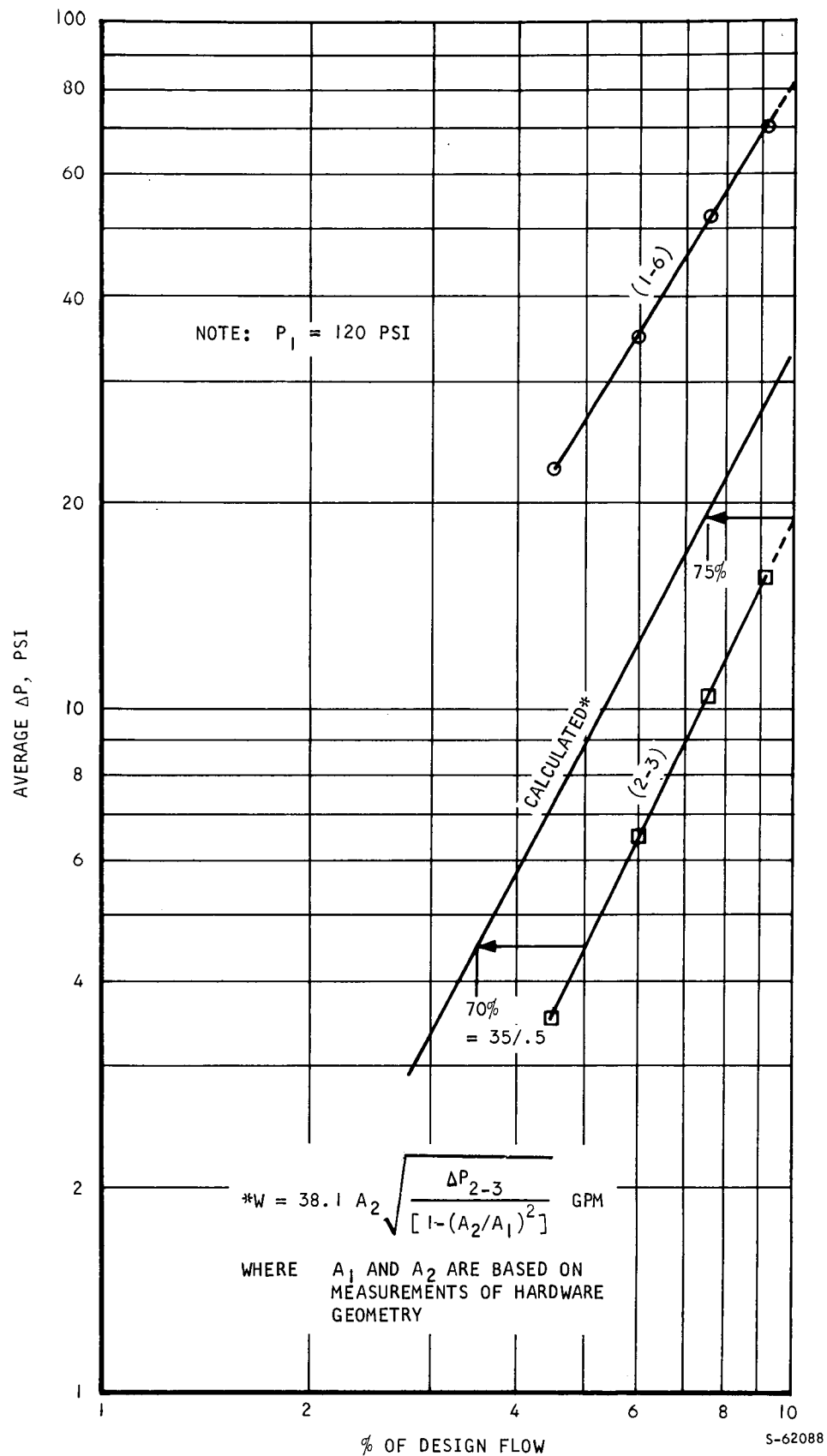


Figure 7-3. Cross-Plot of Full-Scale Cowl Leading Edge



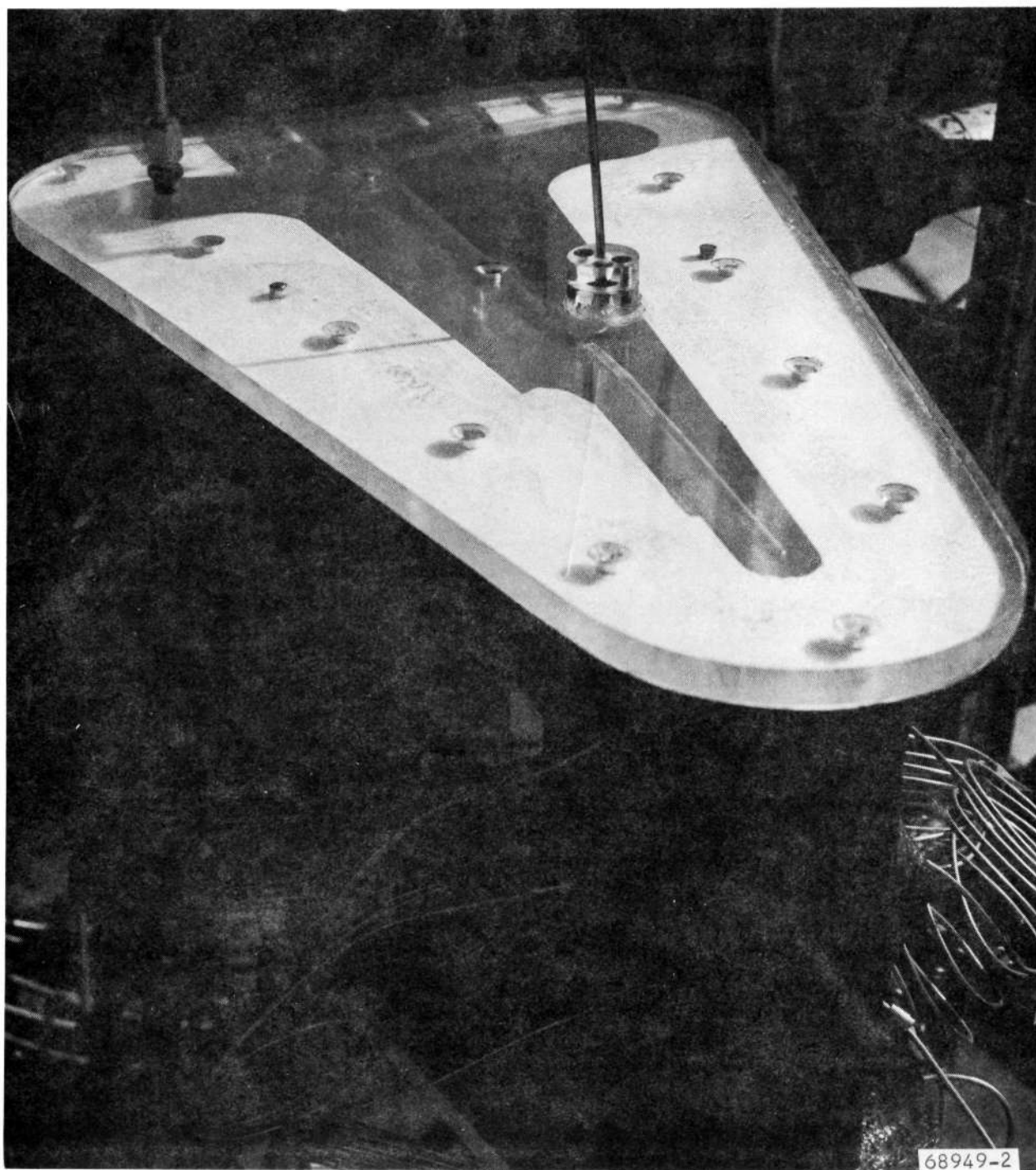


Figure 7-4. 10X-Scale Cowl Leading Edge Plastic Model



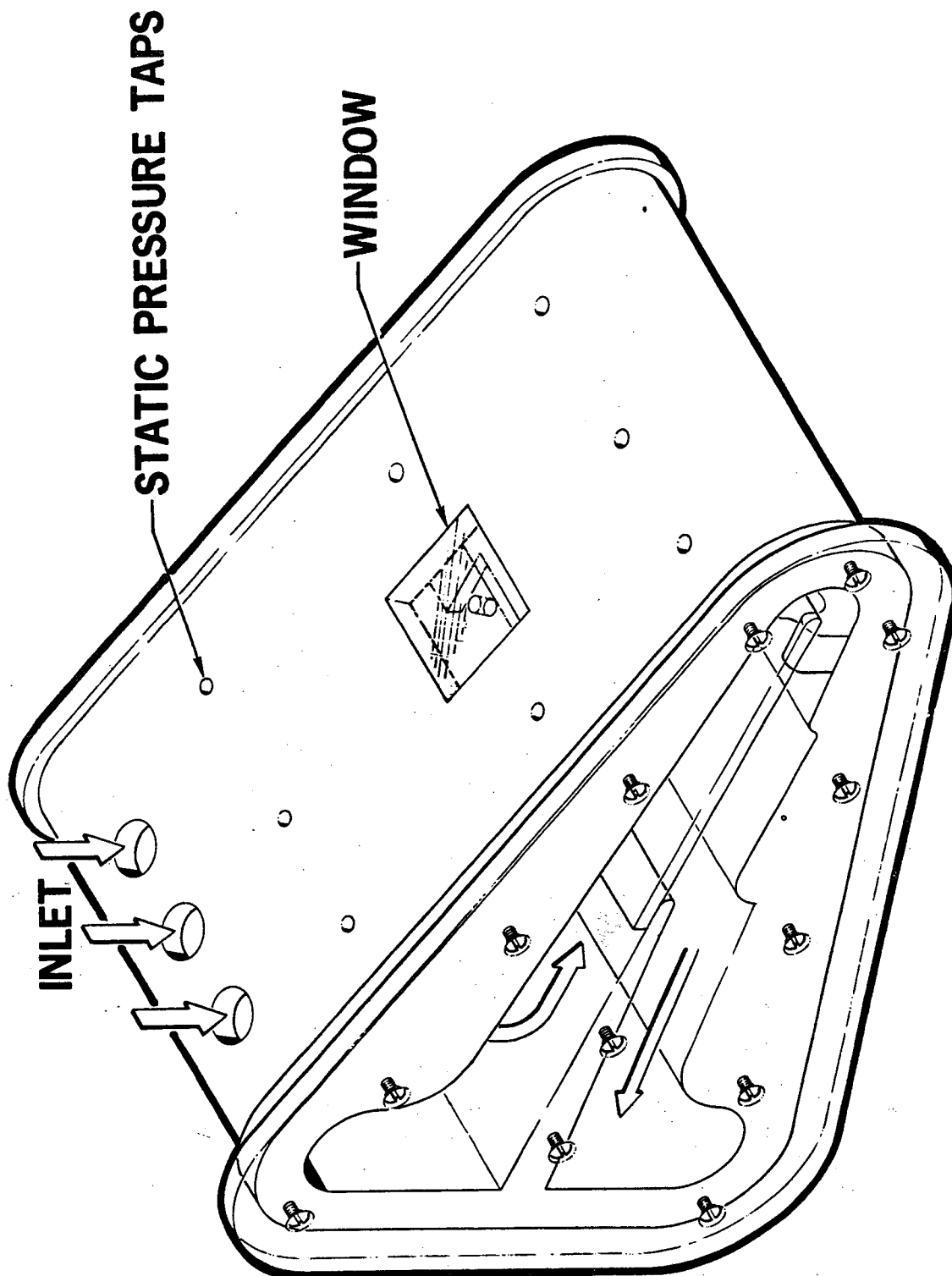
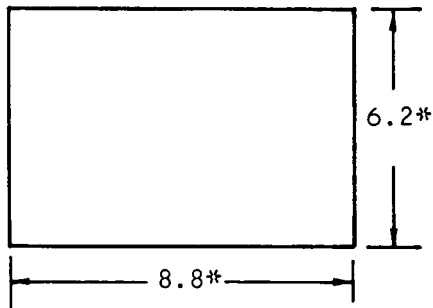


Figure 7-5. 10X-Scale Cowl Leading Edge Plastic Model Schematic

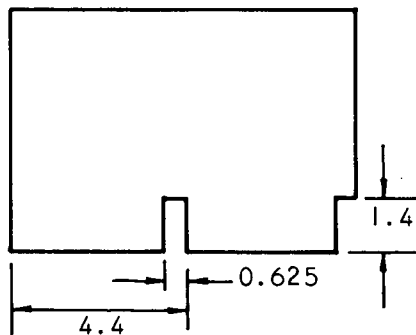


NO. 1

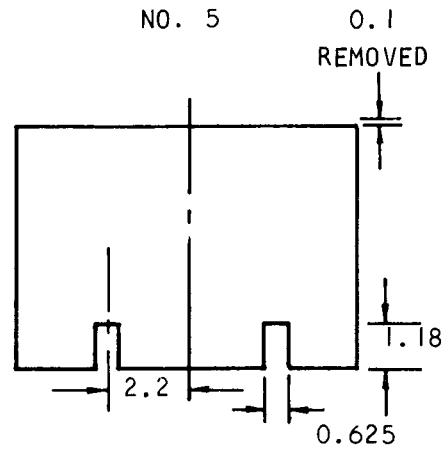


ALL DIMENSIONS IN INCHES

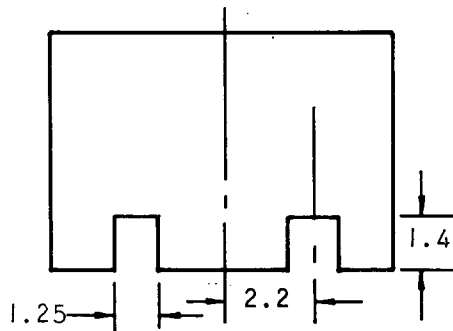
NO. 2



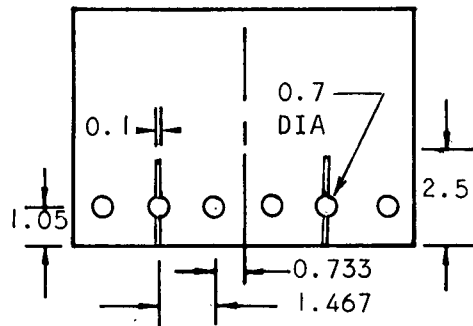
NO. 5



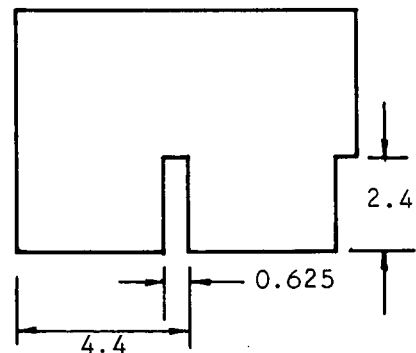
NO. 3



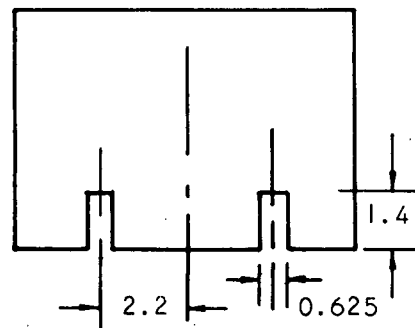
NO. 6



NO. 4



NO. 7



*Dimensions typical except for No. 5

S-62091

Figure 7-6. 10X-Scale Flow-Divider Configurations



AIRESEARCH MANUFACTURING COMPANY
Los Angeles, California

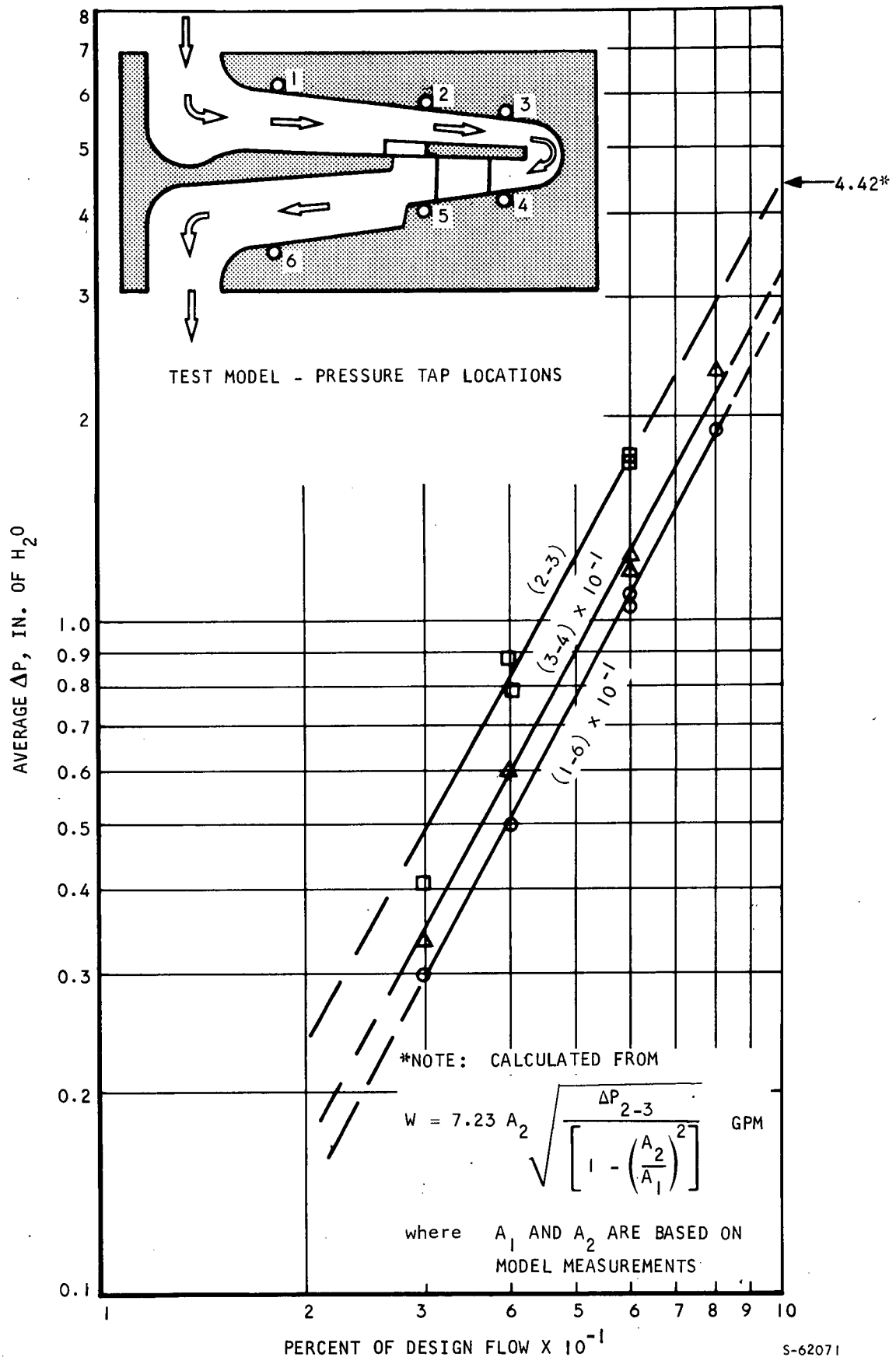


Figure 7-7. 10X-Scale Cowl Leading Edge Configuration I



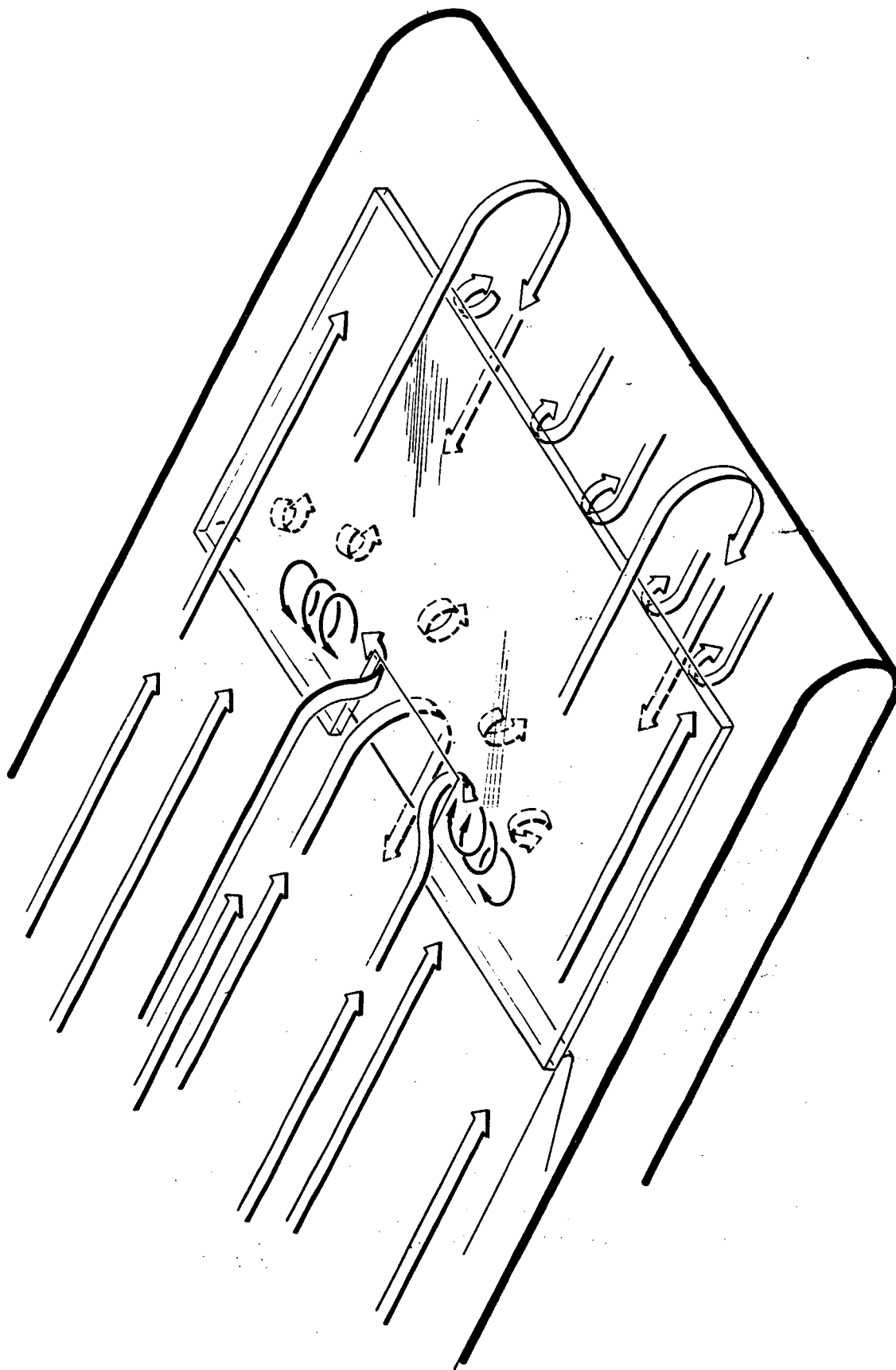
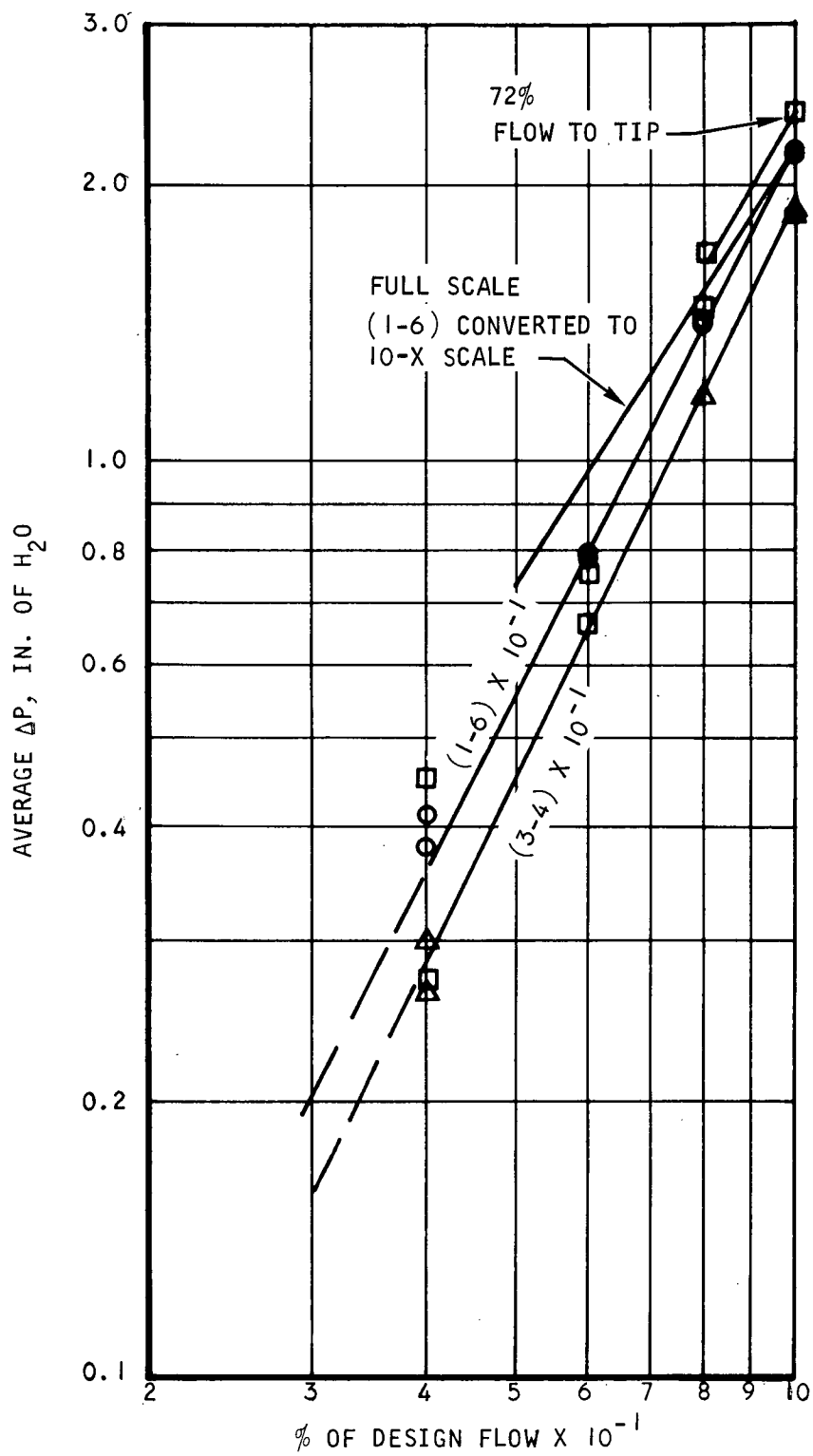


Figure 7-8. Flow Pattern Around Cowl Leading Edge
10X-Scale Bypass Slot





S-62036

Figure 7-9. 10X-Scale Cowl leading Edge Configuration 2



AIRESEARCH MANUFACTURING COMPANY
Los Angeles, California

pressure drop correlated well with the full-scale tests based on the indicated flow split. The flow split itself did not correlate, as Configuration 2 was based on dimensions anticipated for the full-scale test and not actual measurements. Although the location of the bypass slots were ideal for flow visualization, it was suspected that they may have not been ideal for simulation of the full-scale case. Therefore, two new configurations were manufactured, one identical to 2 but with the bypass slots symmetrical (Configuration 7), and one with the dimensions thought to be that of the full-scale design (at this point it was known that the full-scale flow splitter was located in such a manner as to open up the leading edge gap 0.010 in. and reduce the bypass length by the same amount, but it was not known that the flow splitter support was too long), Configuration 5, also with symmetrically located slots.

The third configuration tested had twice the bypass area of the second, with the slots symmetrically located and widened to obtain an increase in the bypass area. These data are shown in Figure 7-10. The overall-scaled pressure drop was reduced from 80 psi to approximately 55 psi with approximately 50 percent of the flow bypassed. Although the performance of this configuration was attractive, the design is very sensitive to placement of the flow divider.

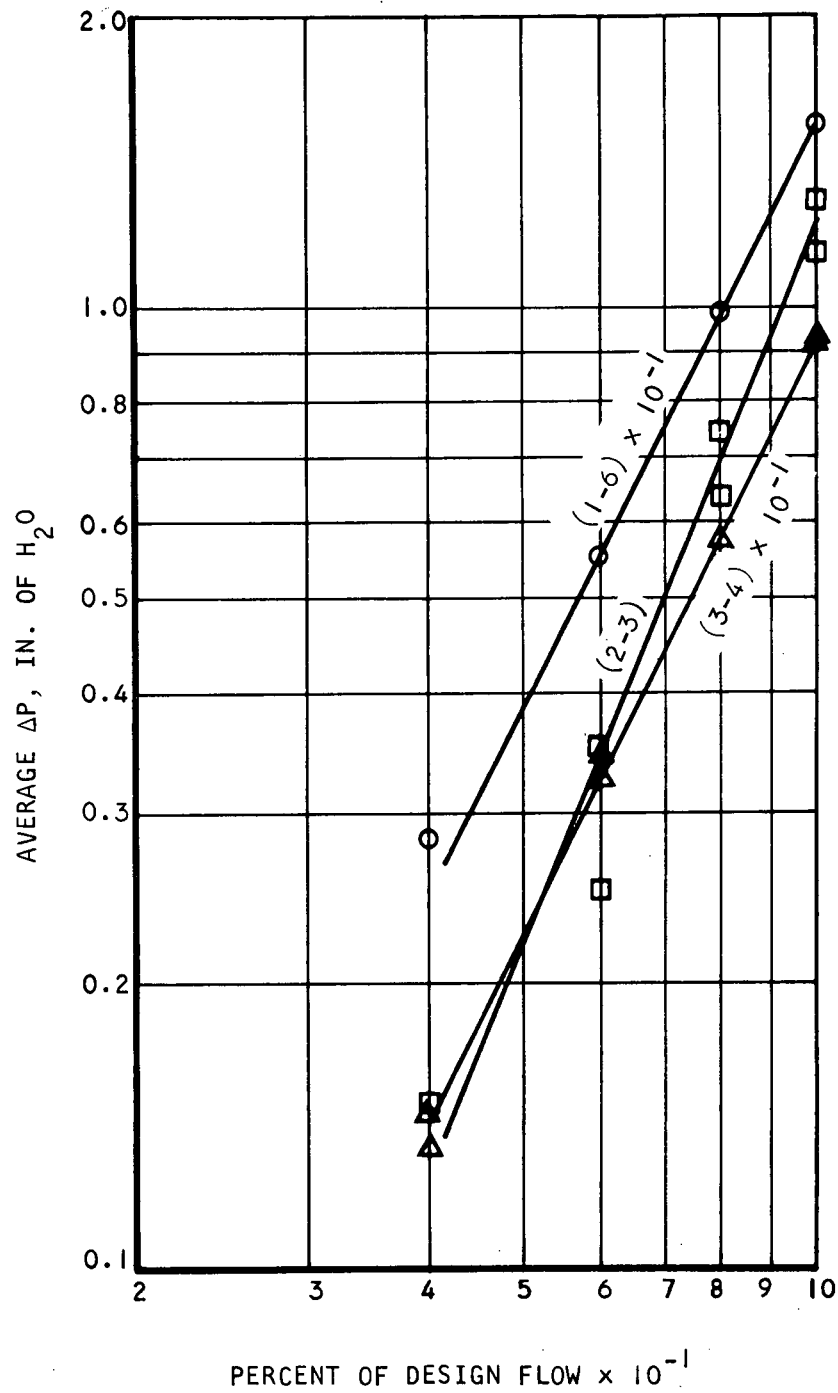
A fourth slotted configuration with approximately the same bypass area as the third was therefore tested. The slots were elongated to that of the original design (Drawing 950554) thereby reducing the sensitivity of the design to the placement of the flow splitter. These data are shown in Figure 7-11. This resulted in a scaled-overall pressure drop of approximately 81 psi and therefore, new slotted design approaches were abandoned as being either too sensitive to manufacturing tolerances or too high in pressure drop.

The fifth configuration, previously described, was tested, and the data is shown in Figure 7-12. A reasonable correlation of full-scale and 10X-scale data was obtained, but again, the flow split should have been lower based on full-scale measurements.

The sixth configuration used a series of small holes to bypass the flow. These holes were so sized and located as to minimize sensitivity to the flow splitter location and still locate them as far aft as feasible to permit the bypass flow to reenter the flow passage where the velocities are reduced. Very small (0.010-in.-wide full-scale) slots were incorporated for mechanical reasons, as the flow splitter must be capable of small deflections where it is supported on the aft end. The data from this test are shown in Figure 7-13. These data resulted in a scaled-overall pressure drop of approximately 50 psi and a tip flow of approximately 55 percent. It was therefore decided to further investigate this configuration with tests on a model which would be more representative of the full-scale cowl leading edge conditions, particularly those associated with cavitation.

Configuration 7, previously described, was tested, although the slotted designs had been abandoned in an effort to further understand the results of the 10X-scale model data. Limited data were obtained and are shown in Figure 7-14. Configuration 7 had the same bypass area as that of Configuration 2 but the bypass slots were centrally located. It was concluded from these



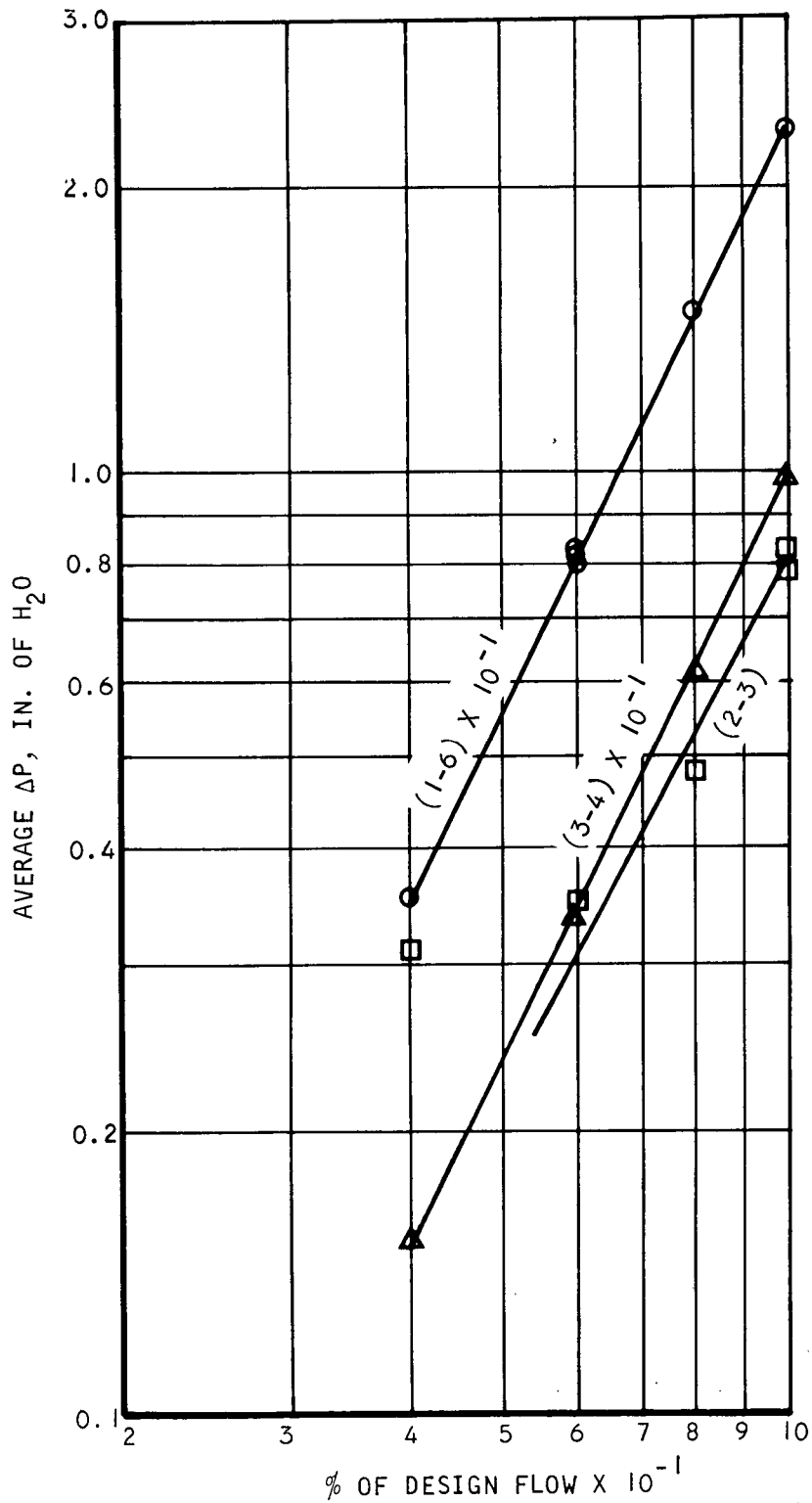


S-62078

Figure 7-10. 10X-Scale Cowl Leading Edge Configuration 3



AIRESEARCH MANUFACTURING COMPANY
Los Angeles, California

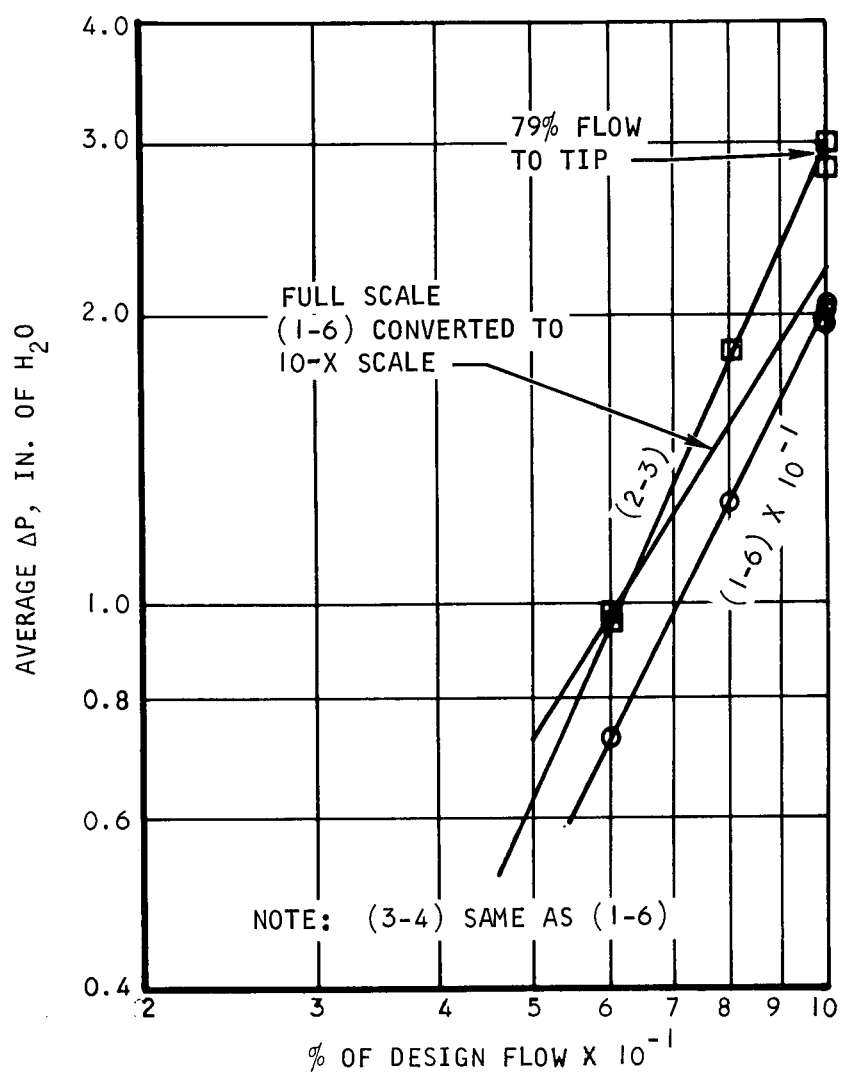


S-62087

Figure 7-11. 10X-Scale Cowl Leading Edge Configuration 4



AIRESEARCH MANUFACTURING COMPANY
Los Angeles, California

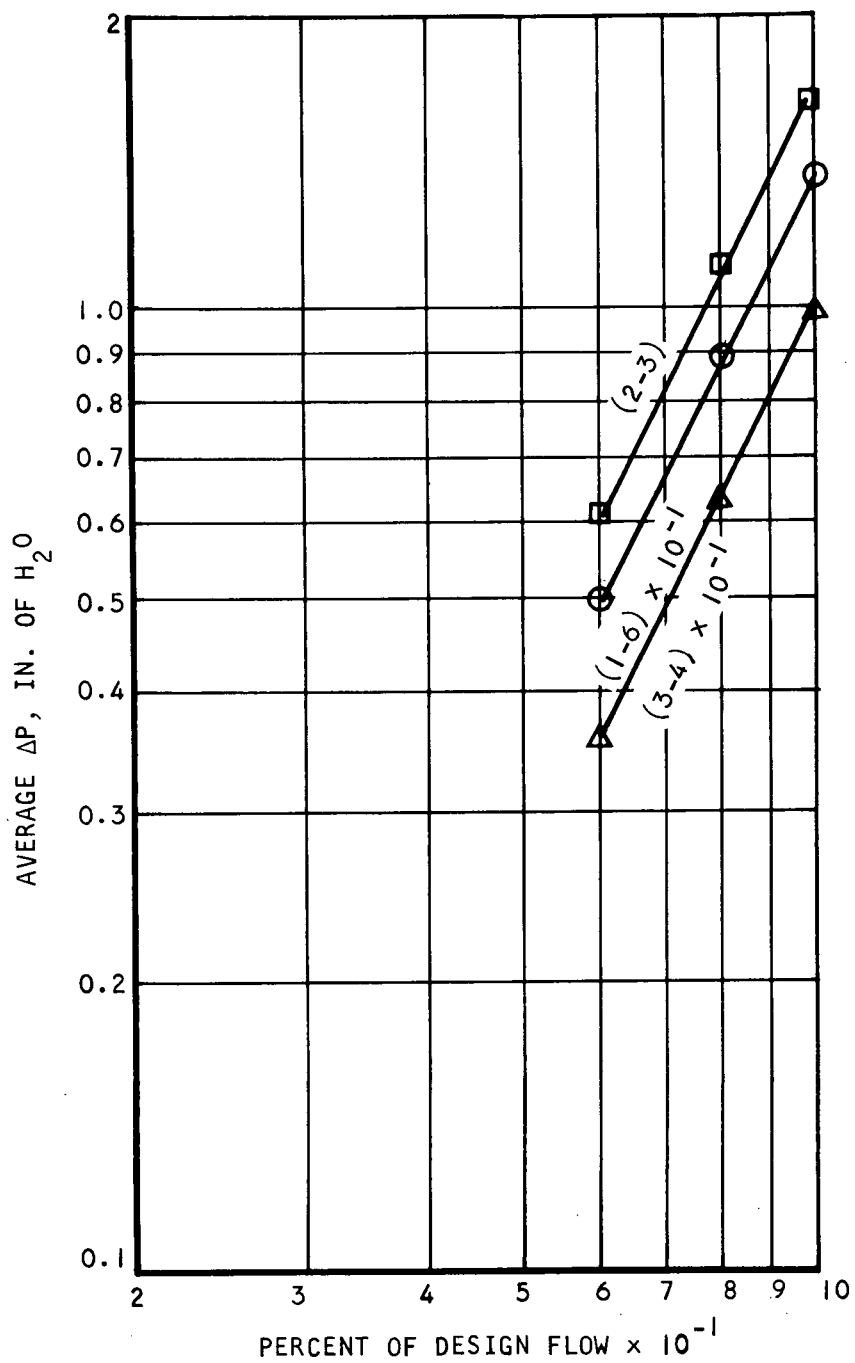


S-62085

Figure 7-12. 10X-Scale Cowl Leading Edge Configuration 5



AIRESEARCH MANUFACTURING COMPANY
Los Angeles, California

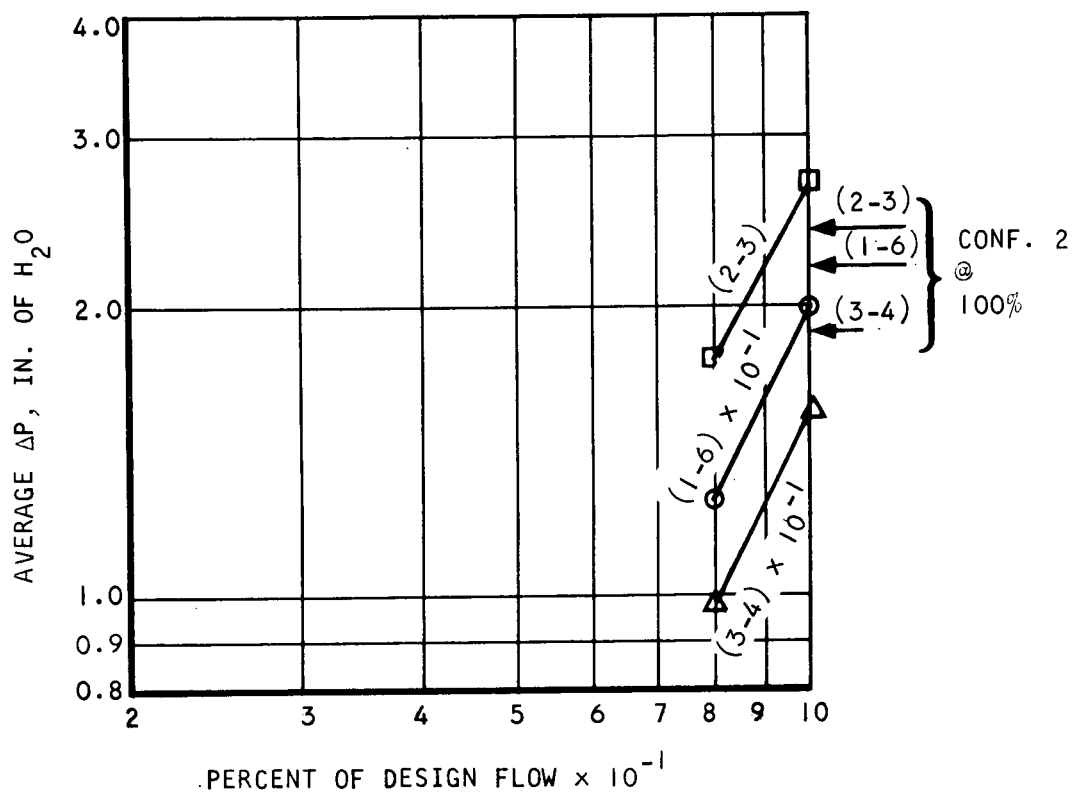


S-62072

Figure 7-13. 10X-Scale Cowl Leading Edge Configuration 6



AIRESEARCH MANUFACTURING COMPANY
Los Angeles, California



S-62077

Figure 7-14. IOX-Scale Cowl Leading Edge Configuration 7



AIRESEARCH MANUFACTURING COMPANY
Los Angeles, California

data that relocation of the slots in the 10X-scale model produces a small change in test results.

A segment of the full-scale cowl leading edge 1.61 in. long was selected for further testing. A flow divider based upon the design of Configuration 6 was planned for initial testing. The results of these tests will be covered in the next report

7.2 METAL JOINING EVALUATION

A test program to evaluate the joining efficiency of the techniques previously mentioned, as well as to investigate the effects of high-stress cyclic loading of the joints, was conducted.

Tensile testing was performed on E-B weld joints, explosive bonded joints, and the parent materials to evaluate joining effectiveness. Low-cycle fatigue testing of copper-nickel joints was also conducted. Results are shown in Table 7-1.

7.2.1 E-B Welded Copper-Nickel Joints

Initial interest in tensile testing was based on a requirement to determine the effect of weld defects on the strength of the joint. The first samples tested had dye-check indications on the bottom of the weld (Table 7-1, tests 1a through 1e).

The tensile results indicated that a slight amount of porosity on the bottom of the joint of a good weld will have little or no effect on tensile strength. If the joint has a larger defect area (for example, 10 percent missed on the bottom), then the tensile strength was seriously affected. The more common defect in copper-to-nickel E-B welding is a partially missed joint (see Figure 7-15). In addition to the incomplete penetration problem, a situation can exist at a copper-nickel joint where the copper will melt but not the nickel. This type of joint is difficult to identify and has a much lower strength.

The zirconium copper-nickel tensile bars in tests 1d and 1e were thin (0.170 in.) bars with complete penetration welds. The decreased strength was due to porosity and annealing in the heat-affected zone.

The tensile bars in tests 1f and 1g are considered good joints and the results confirmed the visual-weld cross-section inspection of the joint.

The square or rectangular test bar configuration served two purposes: (1) To simulate the weld joint as it occurs in the part, since a circular test piece could give misleading results if defects occur near the top or bottom of the weld; and (2) the cross-section of the weld can be polished and etched to show the grain structure of the weld zone before testing.

7.2.2 E-B Welded Copper-Copper Joints

The tensile results for E-B welded zirconium-to-zirconium copper (tests 2a



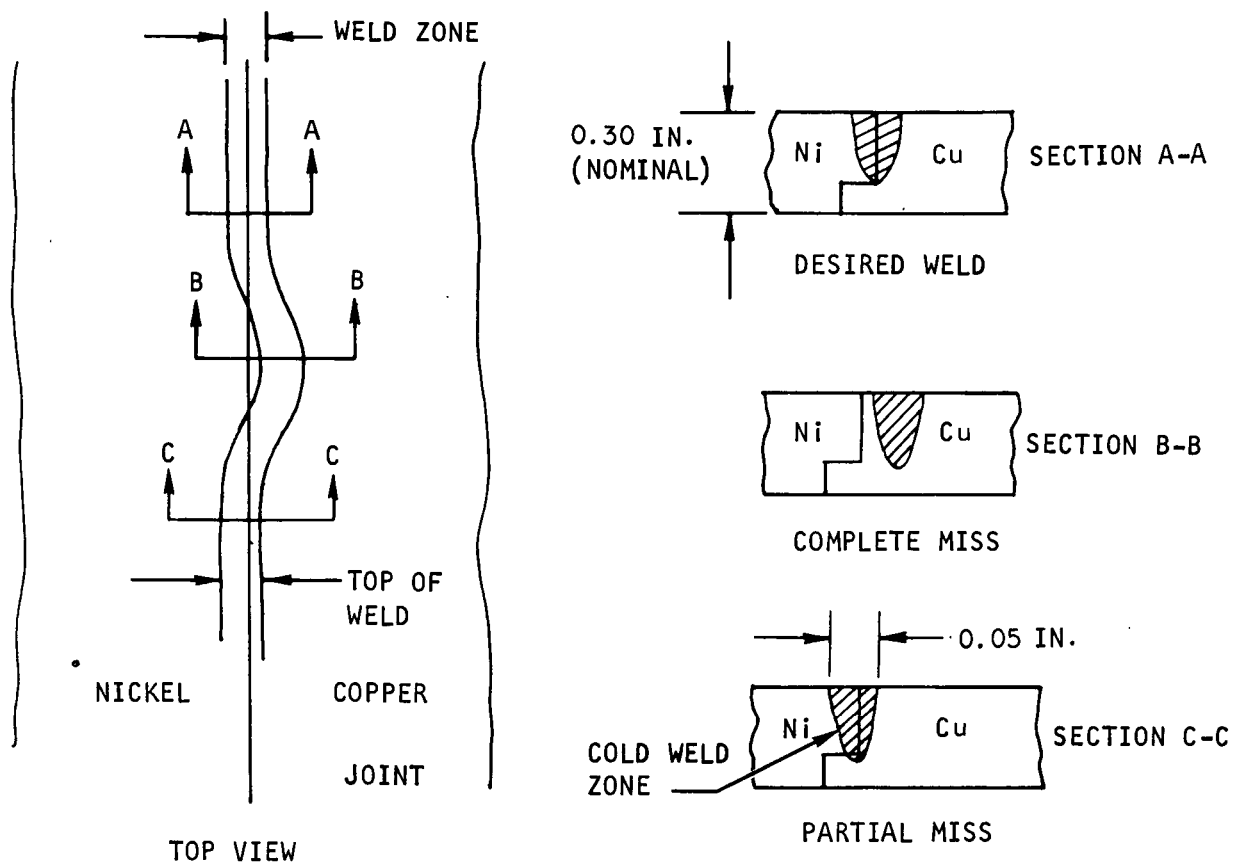
TABLE 7-1
TENSILE TEST RESULTS

Test	Material Used	Yield Stress, S _y , ksi	Ultimate Stress S _{ult} , ksi	Comments
<u>Group 1 E-B Welded Copper-Nickel Joint</u>				
1a	OF Cu-Ni*	-	23.5	Inconsistent results due to variations in weld penetration
1b	OF Cu-Ni	-	38.8	
1c	OF Cu-Ni	-	14.7	
1d	Zr Cu-Ni**	-	47.0	Some porosity in sample
1e	Zr Cu-Ni	-	41.0	2 small voids in sample
1f	OF Cu-Ni	~18	36.9	Not applicable
1g	OF Cu-Ni	~19	37.0	Slight porosity at bottom of weld
<u>Group 2 E-B Welded Zr Copper-Zr Copper Joint</u>				
2a	Zr Cu-Zr Cu	32.7	41.0	Fine porosity through- out weld
2b	Zr Cu-Zr Cu	32.5	41.0	Fine porosity through- out weld
2c	Zr Cu-Zr Cu	32.3	40.8	Fine porosity through- out weld
<u>Group 3 Explosively Bonded "OF" Copper-Nickel Joint</u>				
3a	OF Cu-Ni	32.2	34.6	
3b	OF Cu-Ni	28.5	34.2	
3c	OF Cu-Ni	32.4	35.6	
3d	OF Cu-Ni	-	36.4	
3e	OF Cu-Ni	-	36.5	
<u>Group 4 Properties of Solid (Parent) Materials</u>				
4a	Zr Cu	50.8	56.6	
4b	Zr Cu	50.3	55.8	
4c	Zr Cu	52.2	56.3	
4d	OF Cu	31.1	34.3	
4e	OF Cu	31.1	34.3	
4f	OF Cu	24.2	33.1	Not applicable
4g	Ni 200	22.0	88.7	
4h	Ni 200	22.3	89.5	
4i	Ni 200	22.6	88.5	

*Thickness of OF Cu-Ni sample = 0.210 in.

**Thickness of Zr Cu-Ni sample = 0.170 in.





IN VIEW C-C IT IS SHOWN THAT FOR A TYPICAL 0.05-IN. WIDTH WELD A 0.025-IN. MOVEMENT OF THE BEAM WILL RESULT IN A 90-PERCENT "MISSED" JOINT. THE COLD WELD ZONE OCCURS WHEN THE COPPER, BUT NOT THE NICKEL, MELTS.

S-58321

Figure 7-15. "Missed" E-B Weld Joint Configurations



through 2c) show several effects which are expected to be typical of copper-to-copper E-B welding. During the weld process, metal expulsion rates are much higher than with materials such as nickel or steel. The high expulsion rate during welding results in an irregular weld surface on the top. It was necessary to remove 30 percent of the top surface on a 0.375-in.-thick sample to remove 95 percent of the undercutting. After removing the undercut area, the weld area tensile strength was still only 73 percent of the parent material. This decrease in strength is primarily due to fine porosity in the joint and the annealing effect of the welding.

Two samples of OF copper-to-OF copper were welded, and resulted in similar metal expulsion problems as were experienced when welding zirconium copper. No tensile testing was performed on the OF-copper weld samples.

Using the experience of this test program and information in Reference 6-3, it was concluded that copper-to-copper E-B welding should not be used for the AIM program due to high metal expulsion rates and porosity in the heat-affected zone. It is recommended that E-B welding not be considered for joining copper when thick sections (0.25 in. or larger) are used and when high strength is required.

7.2.3 Explosive-Bonded Copper-Nickel Joint

The initial copper-to-nickel sample consisted of 1-in.-thick OF copper and Nickel-200 plates with an area of 12 by 18 in. The tensile data listed under Group 3 of Table 7-1 were all taken from the 12 by 18 in. test piece. All the samples failed in the parent copper (see Figure 7-16), which indicates that the bonding process for this configuration was acceptable. The high yield strength indicates that the copper is in a 10-percent cold-worked condition. The results of this tensile testing were considered adequate to accept the explosive bonding process for joining copper to nickel.

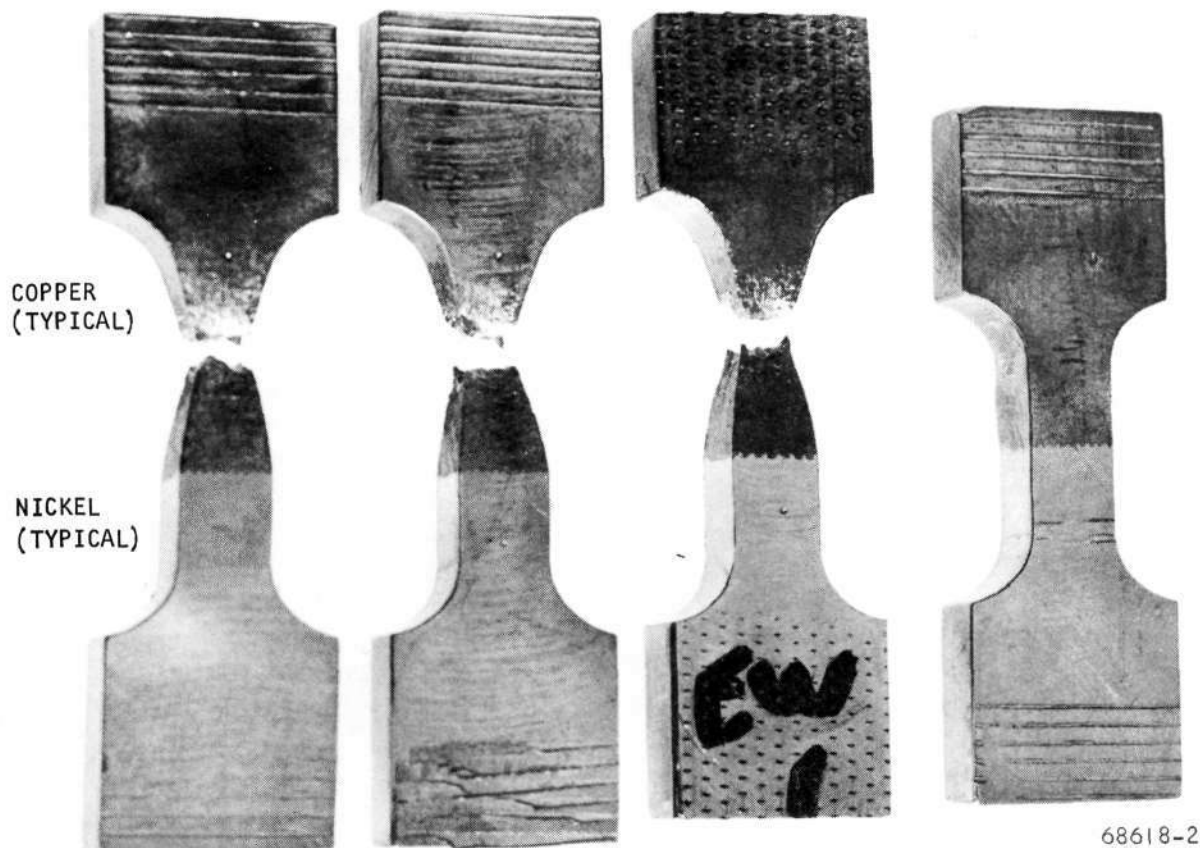
7.2.4 Tensile Strength of Parent Metals

In order to establish standards for the copper and nickel that were being used for the AIM, a series of tensile tests were performed on parent metals samples.

Test Group 4 of Table 7-1 gives the results for zirconium copper which was the same material used for the samples in Group 2. Again, the high yield strength indicates a certain amount of cold working of the material. The ultimate strength values are typical for zirconium copper.

The values under tests 4d and 4f for OF copper indicate a hardness level slightly lower than the explosive-bonded test bars. The sample with the lower yield strength of 24.2 ksi was from the same plate as the two samples with a yield strength of 31.1 ksi. There was no apparent reason for the difference in yield strengths.





F-12437

Figure 7-16. Explosively Bonded OF Copper-to-Nickel-200 Rectangular Tensile Samples



AIRESEARCH MANUFACTURING COMPANY
Los Angeles, California

7.2.5 Low-Cycle Fatigue Testing of Explosively Welded Copper-Nickel Specimen

7.2.5.1 Specimen Configuration

The initial specimens were made from rectangular bars that were 2 in. long by 0.5 in. wide by 0.25 in. thick. The actual gage length was 0.5 in. total, with the weld joint centrally located in this section. The section width in the gage length portion was 0.250 in. An effort was made to carry out push-pull cyclic tests using standard tensile attachment jaws in an Instron 10,000-lb.-capacity universal testing machine. At approximately 3 percent total strain range, there was visible slippage of the specimens in the jaws. There was also substantial buckling of the specimens during the compression portion of the test cycle. This buckling was largely due to the great length of the attachment jaws between the specimen ends and the testing machine fittings which hold the attachment jaws. It was concluded that it was not possible to conduct valid tests with this setup.

Four new round specimens were constructed with a 0.250-in.-dia reduced section and a 0.5-in. gage length. The ends were 1/2 by 13 UNC (Unified National Coarse-Thread Series) threaded sections. This design is depicted in Figure 7-17, which shows Specimen No. 2. Figure 7-18 shows all four of the round test specimens, as well as a rectangular tensile test bar. The redesigned specimen permitted the utilization of much shorter and more rigid threaded adapters for specimen attachment to the test machine.

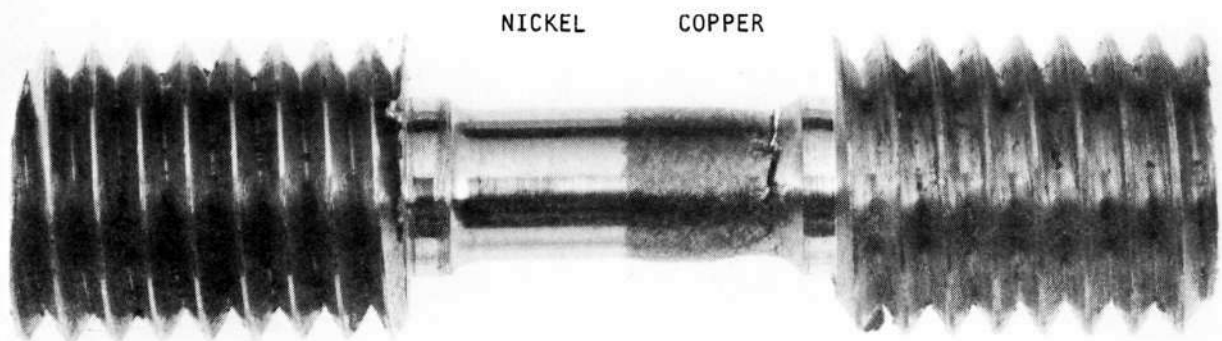
7.2.5.2 Test Results

Each test specimen was subjected to a test history of incrementally increasing applied strain range. The test objective was to determine an experimental value for the ductility constant of the composite structure. The cyclic testing would also demonstrate whether the critical portion of the structure was in the parent copper material, the parent Nickel-200 material or at the bi-metallic joint.

As shown in Figure 7-18, the tensile specimen fractured in the parent copper at a location substantially removed from the weld joint. This mode of failure occurred in three different explosive weld specimens; however, there was still a distinct doubt whether the weld joint would perform as well under cyclic loading where microcracks in the bi-metallic interface could propagate rapidly and lead to failure. A second major goal was to verify whether or not this would happen.

The specific cyclic test histories for each of the four round bar test specimens are presented in Tables 7-2 through 7-5. Shown in these tables are the pertinent dimensions, the plastic strain ranges, the elastic strain ranges, and the total strain ranges.





SPECIMEN NO. 2

08014-1

F-12436

Figure 7-17. OF Copper-Ni 200 Push-Pull Test Specimen No. 2



AIRESEARCH MANUFACTURING COMPANY
Los Angeles, California

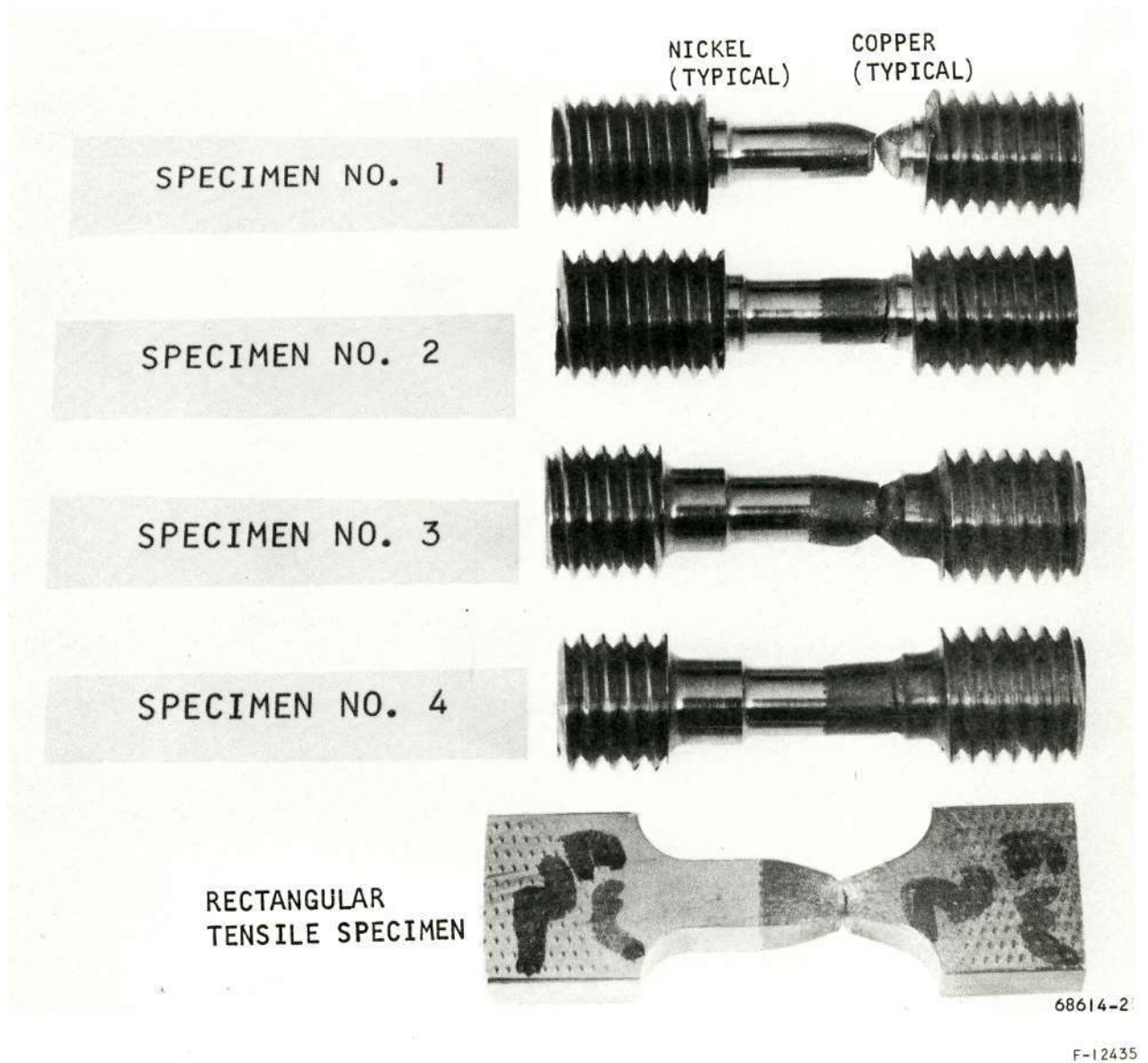


Figure 7-18. Low Cycle Fatigue Test Specimens (Round and Rectangular)



TABLE 7-2

SPECIMEN NO. 1 - CYCLIC TEST HISTORY

Specimen dia, in.	= 0.242
Cross section area, sq in.	= 0.046
Load range, lb	= ± 1400
Stress amplitude, P/A, psi	= 30,000
Elastic modulus, psi	= 15×10^6
Elastic strain range, $2 \epsilon_{el}$, in./in.	= $\frac{2 \times 30 \times 10^6}{15 \times 10^3} = 0.0040$

STRAIN RANGE

<u>Cycle</u>	<u>$\Delta \epsilon_{pl}$</u>	<u>$2 \epsilon_{el}$</u>	<u>$\Delta \epsilon_{total}$</u>
1 - 100	0.0060	0.0040	0.0100
101 - 250	0.0100	0.0040	0.0140
251 - 300	0.0080	0.0040	0.0120
301 - 400	0.0144	0.0040	0.0184
401 - 500*	0.0160	0.0040	0.0200
501 - 545	0.0160	0.0040	0.0200

*First crack noted in Cycle 498 in copper fillet radius near threaded end. Substantial necking down thereafter followed by complete fracture in copper at Cycle 545.



TABLE 7-3

SPECIMEN NO. 2 - CYCLIC TEST HISTORY

Specimen dia, in.	= 0.250
Cross section area, sq in.	= 0.049
Load range, lb	≈ 1500
Stress amplitude, psi	= 30,000
Elastic strain range, in./in.	= 0.0040

STRAIN RANGE

<u>Cycle</u>	<u>$\Delta\epsilon_{pl}$</u>	<u>$2\epsilon_{el}$</u>	<u>$\Delta\epsilon_{total}$</u>
1 - 25	0.0052	0.0040	0.0092
26 - 50	0.0068	0.0040	0.0108
51 - 100	0.0084	0.0040	0.0124
101 - 200	0.0108	0.0040	0.0148
201 - 300	0.0140	0.0040	0.0180
301 - 375	0.0148	0.0040	0.0188
376 - 450	0.0156	0.0040	0.0196
451 - 500	0.0164	0.0040	0.0204
501 - 525*	0.0220	0.0040	0.0260

*Small crack first noted in copper fillet radius near threaded end at Cycle 525. Small crack noted almost simultaneously at weld joint. Large crack propagation in copper at Cycle 561 when test was terminated.



TABLE 7-4

SPECIMEN NO. 3 - CYCLIC TEST HISTORY

Specimen dia, in.	=	0.250
Cross-section area, sq in.	=	0.046
Load range, lb	≈	1500
Stress amplitude, psi	=	30,000
Elastic strain range, in./in.	=	0.0040

STRAIN RANGE

<u>Cycle</u>	<u>$\Delta\epsilon_{pl}$</u>	<u>$2\epsilon_{el}$</u>	<u>$\Delta\epsilon_{total}$</u>
1 - 75	0.0140	0.0040	0.0180
76 - 100	0.0132	0.0040	0.0172
101 - 150*	0.0280	0.0040	0.0320

*Small crack noted in weld joint after 126 cycles.
 Small crack in fillet radius after 140 cycles.
 Significant load degradation after Cycle 150 followed
 by fracture in copper at 162 cycles.



TABLE 7-5

SPECIMEN NO. 4 - CYCLIC TEST HISTORY

Specimen dia, in.	=	0.250
Cross-section area, sq in.	=	0.049
Load range, lb	≈	1650
Stress amplitude, psi	=	33,000
Elastic strain range, in./in.	=	0.0044

STRAIN RANGE

<u>Cycle</u>	<u>$\Delta\epsilon_{pl}$</u>	<u>$2\epsilon_{el}$</u>	<u>$\Delta\epsilon_{total}$</u>
1 - 5	0.0120	0.0044	0.0164
6 - 25	0.0156	0.0044	0.0200
26 - 40	0.0188	0.0044	0.0232
41 - 75	0.0200	0.0044	0.0244
76 - 105	0.0208	0.0044	0.0252
106 - 125*	0.0372	0.0044	0.0416

*Small crack noted in copper fillet radius at 110 cycles.
 Extensive crack growth and local degradation at 125 cycles.
 Test terminated at 131 cycles without complete fracture.



7.2.5.3 Test Data Reduction

The test histories from each specimen were analyzed to obtain the effective ductility constant, C , for the composite structure. This was accomplished by determining the value for (C) that would be required to produce a total damage fraction of 1.0 for each specimen. The accepted formula for low-cycle fatigue analysis is

$$N^C \Delta\epsilon_p = C$$

where: N = cycles to failure
 c = fatigue exponent (≈ 0.5)
 $\Delta\epsilon_p$ = plastic strain range
 C = ductility constant

Utilizing 0.5 for (C) and rearranging the above formula,

$$N = \left(\frac{C}{\Delta\epsilon_p} \right)^2$$

The total damage fraction for a test consisting of several plastic strain levels, $\Delta\epsilon_{pi}$, and a particular number of cycles, η_i , at each strain level

is

$$\sum \frac{\eta_i}{N_i} = \sum \frac{\eta_i}{(C/\Delta\epsilon_{pi})^2} = 1.000$$

This leads to a direct numerical evaluation for (C)

$$C = \left[\sum \eta_i (\Delta\epsilon_{pi})^2 \right]^{1/2}$$

This formula was applied to the test histories of the four test specimens. The evaluations for (C) are tabulated below:

<u>Specimen</u>	<u>Effective (C)</u>
1	0.292
2	0.310
3	0.240
4	<u>0.256</u>
Avg. = 0.274	



The welded tensile specimens fractured in the parent copper portion with an average RA of 82 percent. The related theoretical ductility constant is 1.10 or approximately four-times higher than the test results. The reduced test values were partly due to eccentric loading and localized strain concentrations due to necking at the higher cyclic strain amplitudes.

7.2.6 Nozzle Shroud Trailing Edge Specimens

7.2.6.1 Specimen Configuration

Two test specimens were constructed to the dimensions of the nozzle shroud trailing edge configuration. The trailing edge geometry and the test specimen geometries are shown in Figures 7-19 and 7-20, respectively. Cooling passage pressurization of the nozzle shroud during engine usage will cause the stainless steel outer skin to expand radially, while the Nickel-200 inner skin will be forced radially inward. Due to the design configuration, the trailing edge piece will tend to move with the outer skin. The differential movement between the trailing edge and the inner skin will be absorbed by the contoured transition structure. The OFHC/Nickel-200 bi-metallic joint was located away from the trailing edge so that the metal thickness at the joint would be substantially greater than the minimum section. Another design objective was to place the joint at an inflection point to minimize bending stresses due to the radial deflections.

7.2.6.2 Test Setup

The specimens were tested in the AiResearch Instran 10,000 lb tensile machine. One end of the specimen was rigidly clamped to the movable crossbar, and the other end was attached to the fixed frame of the test machine. This end was also fixtured in a manner to prevent end rotation during the crosshead motion, and to thereby apply a true simulation of the relative displacement caused by pressure loads.

7.2.6.3 Test Results

The computed maximum relative displacement at engine operating pressure was 0.0115 in. The first specimen (No. 1) was cycled at 0.002, 0.004, 0.006, and 0.008 in. with no measurable plastic loop. This specimen, which was instrumented with two strain gages was then subjected to 100 cycles each, at 0.010, 0.020, 0.040, 0.060, and 0.080 in. total deflection range. By the end of the 500th cycle, a small crack had developed at the copper-nickel weld joint, and significant cracking had developed at the copper minimum section. One of the strain gages was located at the minimum section, while the second gage was attached on the copper side of the bi-metallic weld joint. The first gage indicated a small plastic loop at 0.010 in. deflection which continuously increased with deflection. The corresponding plastic flow at the second strain gage was much smaller. The size of the plastic loop from the strain gage at the minimum section was recorded and plotted versus deflection range. These results were utilized to obtain the data presented in Table 7-6.



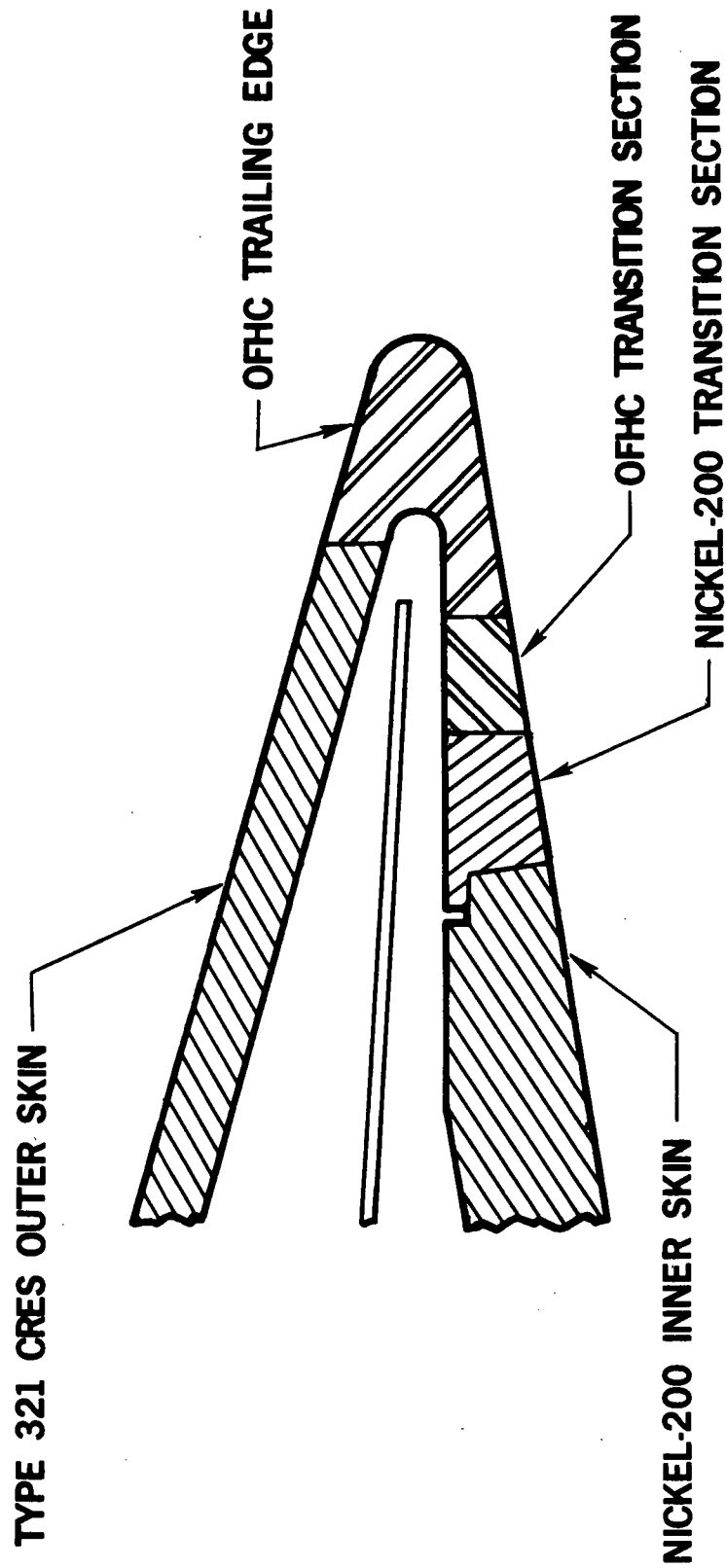


Figure 7-19. Trailing Edge Geometry

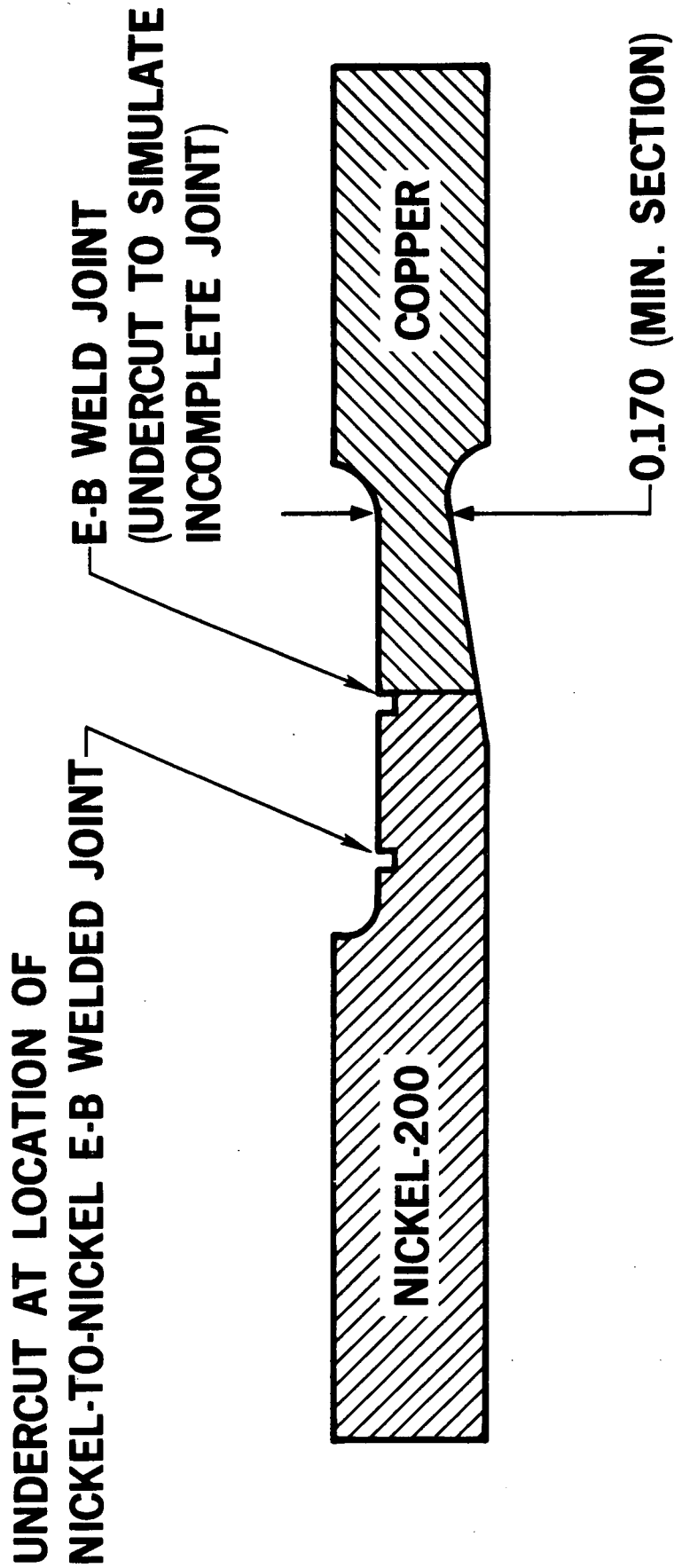


Figure 7-20. Test Specimen Geometry

TABLE 7-6

TEST HISTORY FOR SPECIMEN NO. 1

<u>Deflection Range, in.</u>	<u>Total Strain Range, in./in.</u>	<u>Plastic Strain Range, in./in.</u>	<u>No. of Cycles</u>
0.010	0.00287	small	100
0.020	0.00605	0.00205	100
0.040	0.0134	0.0094	100
0.060	0.0225	0.0185	100
0.080 *	0.0340	0.0284	100
0.100 **	0.0400	0.0360	37

*Gage failed during this run.

**Significant cracking and load decay during this portion of test.
These cycles were not counted in data reduction. Specimen fractured
in copper minimum section at Cycle 37.

The second test specimen was not instrumented with strain gages. Local deflection was monitored on a strip chart to observe the increase in plastic loop size and to keep an accurate count of cycles. The strain gage data from Specimen No. 1 was used to determine the strain range. The test history and appropriate remarks are noted in Table 7-7.

TABLE 7-7

TEST HISTORY FOR SPECIMEN NO. 2

<u>Deflection Range, in.</u>	<u>Total Strain Range, in./in.</u>	<u>Plastic Strain Range, in./in.</u>	<u>No. of Cycles</u>
0.008	0.0025	small	30
0.010	0.00287	small	50
0.016	0.0049	0.0009	100
0.020	0.00605	0.00205	100
0.024	0.0069	0.0029	100
0.030	0.0095	0.0055	100
0.040	0.0134	0.0094	100
0.050	0.0175	0.0135	100
0.070	0.0275	0.0235	100
0.090	0.0400	0.0360	133

*Small loss in load with slight crack in weld at cycle 50.

Significant cracking in copper minimum section accompanied by marked load decay each cycle after cycle 50 until total fracture at cycle 133. Only first 50 cycles counted towards fatigue life.



7.2.6.4 Test Data Reduction

The observed plastic flow per cycle for the entire test history was used to obtain the effective ductility constant for the two test specimens. The computed results were:

For specimen No. 1: $C = 0.352$

For specimen No. 2: $C = 0.388$

These results indicated higher ductility constants for the copper than the push-pull explosively welded specimens. This was partly due to the fact that strain range was being measured at the critical location, and that the effects of localized strain concentration was minimized.

7.2.6.5 Conclusions

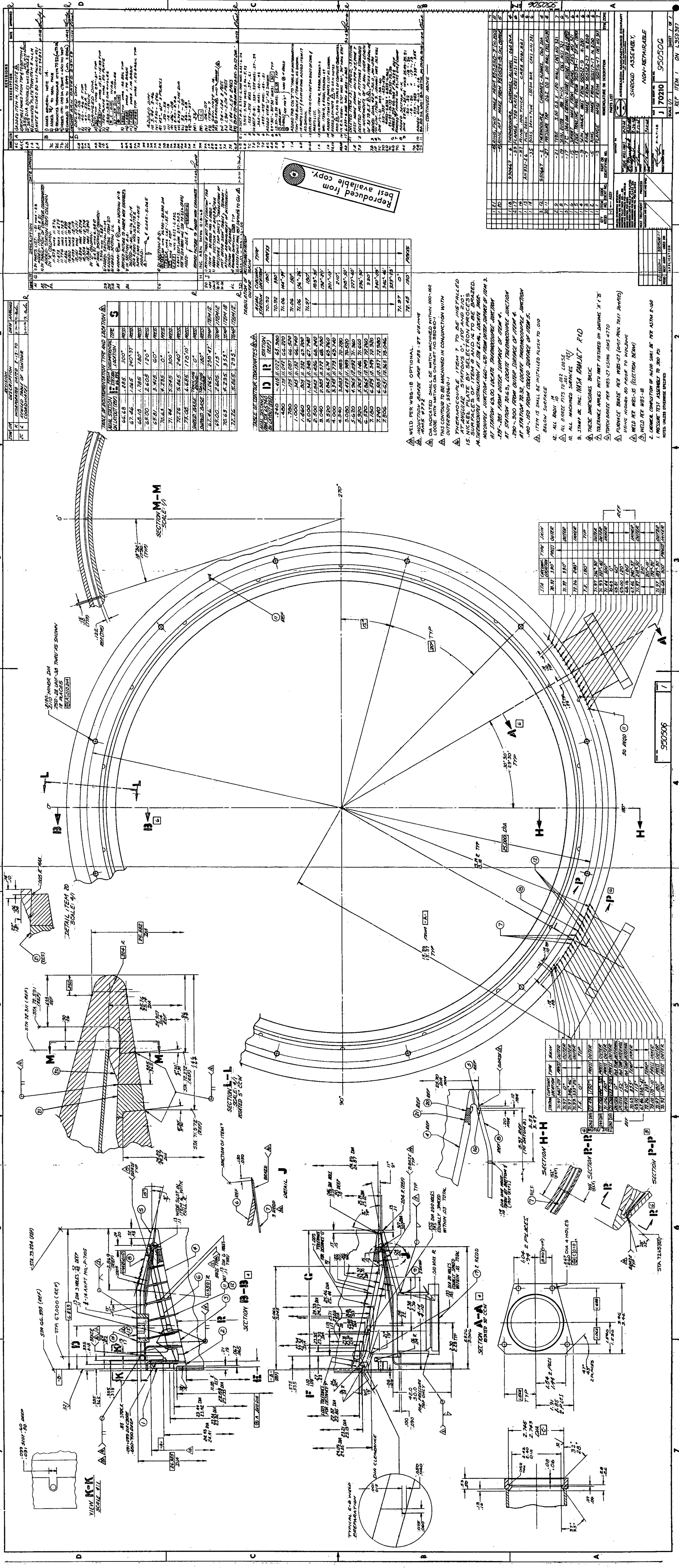
The plastic loop at rated operating conditions will be quite small. The design life of the trailing edge structure due to low cycle fatigue is estimated to be well in excess of 2000 cycles. The most critical area is at the minimum copper section, rather than at the bi-metallic joint which fulfills the design intent.



REFERENCES

- 5-1. Engineering Staff, Hypersonic Research Engine Project - Phase IIA, Structures and Cooling Development, Eighth Interim Technical Data Report, Data Item 55-7.08, AiResearch Report No. AP-69-4759, 27 February 1969.
- 5-2. Fay, J. A., and F. R. Riddell, "Theory of Stagnation Point Heat Transfer in Dissociated Air," Journal of the Aeronautical Sciences, Volume 25, No. 2, February 1958.
- 5-3. Glen, G., et al, "Investigation of Local Heat-Transfer and Pressure Drag Characteristics of a Yawed Circular Cylinder at Supersonic Speeds," NACA RM A55H31, January 1956.
- 5-4. Engineering Staff, Hypersonic Research Engine Project - Phase IIA, Phase IIA Aerothermodynamic Integration Model (AIM) Development, Fifth Interim Technical Data Report, Data Item No. 55-4.05, AiResearch Report No. 69-5298, 8 July 1969, CONFIDENTIAL.
- 5-5. HRE/AIM Heat Transfer Calculation File No. 42, Aug. 1968.
- 6-1. Zermansky, M. W., Heat and Thermodynamics, 4th Edition, McGraw-Hill, New York, 1957.
- 6-2. Anon., Allegheny Ludlum Mu Metal Including Magnetic Shielding Data, Allegheny Ludlum Blue Sheet EM-12 Edition 10, Allegheny Ludlum Steel Corp., Pittsburgh 22, Penn.
- 6-3. Holtzman, A. H., and G. R. Cowan, "Bonding of Metals with Explosives", Welding Research Council Bulletin No. 104, April 1965, pp 1-21.
- 6-4. Johnson, L. D., "Some Observations on the Electron Beam Welding of Copper", Welding Journal, Vol. 49, No. 2, February 1970, Research Supplement pp 55s - 60s.
- 7-1. Stonemetz, R. E., "Liquid Cavitation Studies in Circular Pipe Bends," NASA TN D-3176, dated December 1965.



[illegible]

DATE	TIME	BY	REMARKS
1	REP	ITEM 1	ON L950987

Page intentionally left blank

Page intentionally left blank

Page intentionally left blank

Page intentionally left blank

Page intentionally left blank

Page intentionally left blank

Page intentionally left blank

Page intentionally left blank

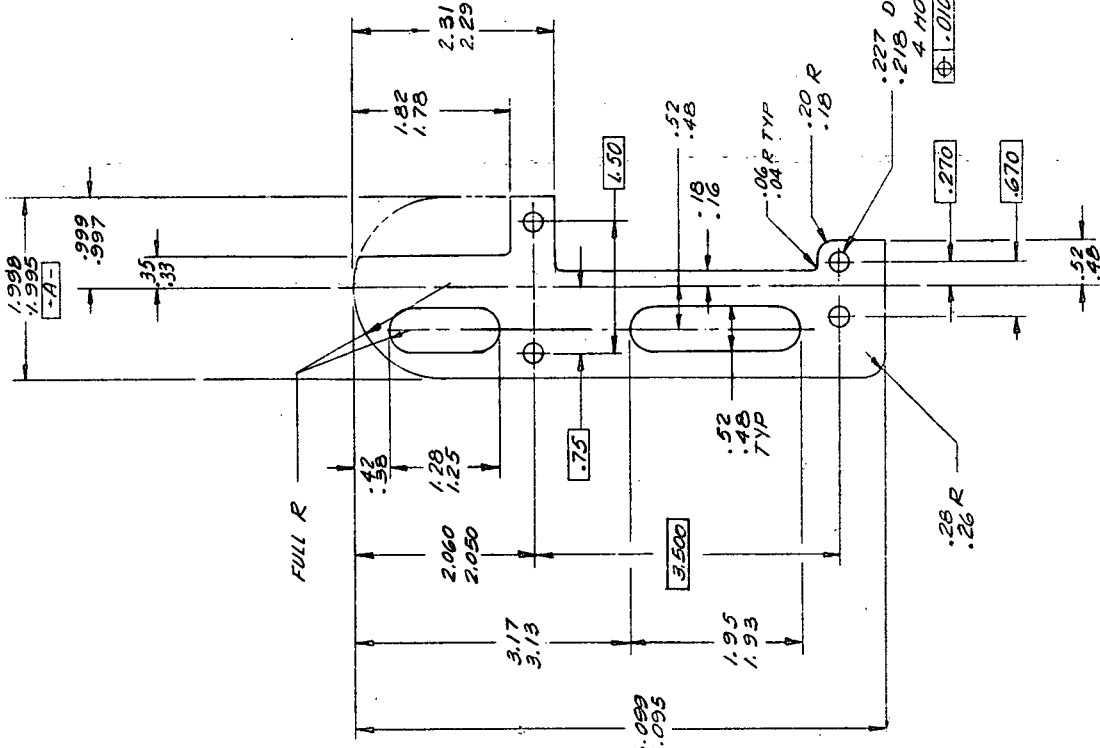
Page intentionally left blank

Page intentionally left blank

Page intentionally left blank

FOLDOUT FRAME

Abstract



REVIEWS			
LTR	DESCRIPTION	DATE	APPROVED
A-1	DELETED DMS 2-11-73, 2-01-2-03; 2-04-73, 2-05-73, 2-06-73, 2-07-73; 2-08-73, 2-09-73, 2-10-73, 2-11-73; 2-12-73, 2-13-73, 2-14-73, 2-15-73; 2-16-73, 2-17-73, 2-18-73, 2-19-73; 2-20-73, 2-21-73, 2-22-73, 2-23-73; 2-24-73, 2-25-73, 2-26-73, 2-27-73; 2-28-73, 2-29-73, 2-30-73, 2-31-73; 2-32-73, 2-33-73, 2-34-73, 2-35-73; 2-36-73, 2-37-73, 2-38-73, 2-39-73; 2-40-73, 2-41-73, 2-42-73, 2-43-73; 2-44-73, 2-45-73, 2-46-73, 2-47-73; 2-48-73, 2-49-73, 2-50-73, 2-51-73; 2-52-73, 2-53-73, 2-54-73, 2-55-73; 2-56-73, 2-57-73, 2-58-73, 2-59-73; 2-60-73, 2-61-73, 2-62-73, 2-63-73; 2-64-73, 2-65-73, 2-66-73, 2-67-73; 2-68-73, 2-69-73, 2-70-73, 2-71-73; 2-72-73, 2-73-73, 2-74-73, 2-75-73; 2-76-73, 2-77-73, 2-78-73, 2-79-73; 2-80-73, 2-81-73, 2-82-73, 2-83-73; 2-84-73, 2-85-73, 2-86-73, 2-87-73; 2-88-73, 2-89-73, 2-90-73, 2-91-73; 2-92-73, 2-93-73, 2-94-73, 2-95-73; 2-96-73, 2-97-73, 2-98-73, 2-99-73; 2-100-73, 2-101-73, 2-102-73, 2-103-73; 2-104-73, 2-105-73, 2-106-73, 2-107-73; 2-108-73, 2-109-73, 2-110-73, 2-111-73; 2-112-73, 2-113-73, 2-114-73, 2-115-73; 2-116-73, 2-117-73, 2-118-73, 2-119-73; 2-120-73, 2-121-73, 2-122-73, 2-123-73; 2-124-73, 2-125-73, 2-126-73, 2-127-73; 2-128-73, 2-129-73, 2-130-73, 2-131-73; 2-132-73, 2-133-73, 2-134-73, 2-135-73; 2-136-73, 2-137-73, 2-138-73, 2-139-73; 2-140-73, 2-141-73, 2-142-73, 2-143-73; 2-144-73, 2-145-73, 2-146-73, 2-147-73; 2-148-73, 2-149-73, 2-150-73, 2-151-73; 2-152-73, 2-153-73, 2-154-73, 2-155-73; 2-156-73, 2-157-73, 2-158-73, 2-159-73; 2-160-73, 2-161-73, 2-162-73, 2-163-73; 2-164-73, 2-165-73, 2-166-73, 2-167-73; 2-168-73, 2-169-73, 2-170-73, 2-171-73; 2-172-73, 2-173-73, 2-174-73, 2-175-73; 2-176-73, 2-177-73, 2-178-73, 2-179-73; 2-180-73, 2-181-73, 2-182-73, 2-183-73; 2-184-73, 2-185-73, 2-186-73, 2-187-73; 2-188-73, 2-189-73, 2-190-73, 2-191-73; 2-192-73, 2-193-73, 2-194-73, 2-195-73; 2-196-73, 2-197-73, 2-198-73, 2-199-73; 2-200-73, 2-201-73, 2-202-73, 2-203-73; 2-204-73, 2-205-73, 2-206-73, 2-207-73; 2-208-73, 2-209-73, 2-210-73, 2-211-73; 2-212-73, 2-213-73, 2-214-73, 2-215-73; 2-216-73, 2-217-73, 2-218-73, 2-219-73; 2-220-73, 2-221-73, 2-222-73, 2-223-73; 2-224-73, 2-225-73, 2-226-73, 2-227-73; 2-228-73, 2-229-73, 2-230-73, 2-231-73; 2-232-73, 2-233-73, 2-234-73, 2-235-73; 2-236-73, 2-237-73, 2-238-73, 2-239-73; 2-240-73, 2-241-73, 2-242-73, 2-243-73; 2-244-73, 2-245-73, 2-246-73, 2-247-73; 2-248-73, 2-249-73, 2-250-73, 2-251-73; 2-252-73, 2-253-73, 2-254-73, 2-255-73; 2-256-73, 2-257-73, 2-258-73, 2-259-73; 2-260-73, 2-261-73, 2-262-73, 2-263-73; 2-264-73, 2-265-73, 2-266-73, 2-267-73; 2-268-73, 2-269-73, 2-270-73, 2-271-73; 2-272-73, 2-273-73, 2-274-73, 2-275-73; 2-276-73, 2-277-73, 2-278-73, 2-279-73; 2-280-73, 2-281-73, 2-282-73, 2-283-73; 2-284-73, 2-285-73, 2-286-73, 2-287-73; 2-288-73, 2-289-73, 2-290-73, 2-291-73; 2-292-73, 2-293-73, 2-294-73, 2-295-73; 2-296-73, 2-297-73, 2-298-73, 2-299-73; 2-300-73, 2-301-73, 2-302-73, 2-303-73; 2-304-73, 2-305-73, 2-306-73, 2-307-73; 2-308-73, 2-309-73, 2-310-73, 2-311-73; 2-312-73, 2-313-73, 2-314-73, 2-315-73; 2-316-73, 2-317-73, 2-318-73, 2-319-73; 2-320-73, 2-321-73, 2-322-73, 2-323-73; 2-324-73, 2-325-73, 2-326-73, 2-327-73; 2-328-73, 2-329-73, 2-330-73, 2-331-73; 2-332-73, 2-333-73, 2-334-73, 2-335-73; 2-336-73, 2-337-73, 2-338-73, 2-339-73; 2-340-73, 2-341-73, 2-342-73, 2-343-73; 2-344-73, 2-345-73, 2-346-73, 2-347-73; 2-348-73, 2-349-73, 2-350-73, 2-351-73; 2-352-73, 2-353-73, 2-354-73, 2-355-73; 2-356-73, 2-357-73, 2-358-73, 2-359-73; 2-360-73, 2-361-73, 2-362-73, 2-363-73; 2-364-73, 2-365-73, 2-366-73, 2-367-73; 2-368-73, 2-369-73, 2-370-73, 2-371-73; 2-372-73, 2-373-73, 2-374-73, 2-375-73; 2-376-73, 2-377-73, 2-378-73, 2-379-73; 2-380-73, 2-381-73, 2-382-73, 2-383-73; 2-384-73, 2-385-73, 2-386-73, 2-387-73; 2-388-73, 2-389-73, 2-390-73, 2-391-73; 2-392-73, 2-393-73, 2-394-73, 2-395-73; 2-396-73, 2-397-73, 2-398-73, 2-399-73; 2-400-73, 2-401-73, 2-402-73, 2-403-73; 2-404-73, 2-405-73, 2-406-73, 2-407-73; 2-408-73, 2-409-73, 2-410-73, 2-411-73; 2-412-73, 2-413-73, 2-414-73, 2-415-73; 2-416-73, 2-417-73, 2-418-73, 2-419-73; 2-420-73, 2-421-73, 2-422-73, 2-423-73; 2-424-73, 2-425-73, 2-426-73, 2-427-73; 2-428-73, 2-429-73, 2-430-73, 2-431-73; 2-432-73, 2-433-73, 2-434-73, 2-435-73; 2-436-73, 2-437-73, 2-438-73, 2-439-73; 2-440-73, 2-441-73, 2-442-73, 2-443-73; 2-444-73, 2-445-73, 2-446-73, 2-447-73; 2-448-73, 2-449-73, 2-450-73, 2-451-73; 2-452-73, 2-453-73, 2-454-73, 2-455-73; 2-456-73, 2-457-73, 2-458-73, 2-459-73; 2-460-73, 2-461-73, 2-462-73, 2-463-73; 2-464-73, 2-465-73, 2-466-73, 2-467-73; 2-468-73, 2-469-73, 2-470-73, 2-471-73; 2-472-73, 2-473-73, 2-474-73, 2-475-73; 2-476-73, 2-477-73, 2-478-73, 2-479-73; 2-480-73, 2-481-73, 2-482-73, 2-483-73; 2-484-73, 2-485-73, 2-486-73, 2-487-73; 2-488-73, 2-489-73, 2-490-73, 2-491-73; 2-492-73, 2-493-73, 2-494-73, 2-495-73; 2-496-73, 2-497-73, 2-498-73, 2-499-73; 2-500-73, 2-501-73, 2-502-73, 2-503-73; 2-504-73, 2-505-73, 2-506-73, 2-507-73; 2-508-73, 2-509-73, 2-510-73, 2-511-73; 2-512-73, 2-513-73, 2-514-73, 2-515-73; 2-516-73, 2-517-73, 2-518-73, 2-519-73; 2-520-73, 2-521-73, 2-522-73, 2-523-73; 2-524-73, 2-525-73, 2-526-73, 2-527-73; 2-528-73, 2-529-73, 2-530-73, 2-531-73; 2-532-73, 2-533-73, 2-534-73, 2-535-73; 2-536-73, 2-537-73, 2-538-73, 2-539-73; 2-540-73, 2-541-73, 2-542-73, 2-543-73; 2-544-73, 2-545-73, 2-546-73, 2-547-73; 2-548-73, 2-549-73, 2-550-73, 2-551-73; 2-552-73, 2-553-73, 2-554-73, 2-555-73; 2-556-73, 2-557-73, 2-558-73, 2-559-73; 2-560-73, 2-561-73, 2-562-73, 2-563-73; 2-564-73, 2-565-73, 2-566-73, 2-567-73; 2-568-73, 2-569-73, 2-570-73, 2-571-73; 2-572-73, 2-573-73, 2-574-73, 2-575-73; 2-576-73, 2-577-73, 2-578-73, 2-579-73; 2-580-73, 2-581-73, 2-582-73, 2-583-73; 2-584-73, 2-585-73, 2-586-73, 2-587-73; 2-588-73, 2-589-73, 2-590-73, 2-591-73; 2-592-73, 2-593-73, 2-594-73, 2-595-73; 2-596-73, 2-597-73, 2-598-73, 2-599-73; 2-600-73, 2-601-73, 2-602-73, 2-603-73; 2-604-73, 2-605-73, 2-606-73, 2-607-73; 2-608-73, 2-609-73, 2-610-73, 2-611-73; 2-612-73, 2-613-73, 2-614-73, 2-615-73; 2-616-73, 2-617-73, 2-618-73, 2-619-73; 2-620-73, 2-621-73, 2-622-73, 2-623-73; 2-624-73, 2-625-73, 2-626-73, 2-627-73; 2-628-73, 2-629-73, 2-630-73, 2-631-73; 2-632-73, 2-633-73, 2-634-73, 2-635-73; 2-636-73, 2-637-73, 2-638-73, 2-639-73; 2-640-73, 2-641-73, 2-642-73, 2-643-73; 2-644-73, 2-645-73, 2-646-73, 2-647-73; 2-648-73, 2-649-73, 2-650-73, 2-651-73; 2-652-73, 2-653-73, 2-654-73, 2-655-73; 2-656-73, 2-657-73, 2-658-73, 2-659-73; 2-660-73, 2-661-73, 2-662-73, 2-663-73; 2-664-73, 2-665-73, 2-666-73, 2-667-73; 2-668-73, 2-669-73, 2-670-73, 2-671-73; 2-672-73, 2-673-73, 2-674-73, 2-675-73; 2-676-73, 2-677-73, 2-678-73, 2-679-73; 2-680-73, 2-681-73, 2-682-73, 2-683-73; 2-684-73, 2-685-73, 2-686-73, 2-687-73; 2-688-73, 2-689-73, 2-690-73, 2-691-73; 2-692-73, 2-693-73, 2-694-73, 2-695-73; 2-696-73, 2-697-73, 2-698-73, 2-699-73; 2-700-73, 2-701-73, 2-702-73, 2-703-73; 2-704-73, 2-705-73, 2-706-73, 2-707-73; 2-708-73, 2-709-73, 2-710-73, 2-711-73; 2-712-73, 2-713-73, 2-714-73, 2-715-73; 2-716-73, 2-717-73, 2-718-73, 2-719-73; 2-720-73, 2-721-73, 2-722-73, 2-723-73; 2-724-73, 2-725-73, 2-726-73, 2-727-73; 2-728-73, 2-729-73, 2-730-73, 2-731-73; 2-732-73, 2-733-73, 2-734-73, 2-735-73; 2-736-73, 2-737-73, 2-738-73, 2-739-73; 2-740-73, 2-741-73, 2-742-73, 2-743-73; 2-744-73, 2-745-73, 2-746-73, 2-747-73; 2-748-73, 2-749-73, 2-750-73, 2-751-73; 2-752-73, 2-753-73, 2-754-73, 2-755-73; 2-756-73, 2-757-73, 2-758-73, 2-759-73; 2-760-73, 2-761-73, 2-762-73, 2-763-73; 2-764-73, 2-765-73, 2-766-73, 2-767-73; 2-768-73, 2-769-73, 2-770-73, 2-771-73; 2-772-73, 2-773-73, 2-774-73, 2-775-73; 2-776-73, 2-777-73, 2-778-73, 2-779-73; 2-780-73, 2-781-73, 2-782-73, 2-783-73; 2-784-73, 2-785-73, 2-786-73, 2-787-73; 2-788-73, 2-789-73, 2-790-73, 2-791-73; 2-792-73, 2-793-73, 2-794-73, 2-795-73; 2-796-73, 2-797-73, 2-798-73, 2-799-73; 2-800-73, 2-801-73, 2-802-73, 2-803-73; 2-804-73, 2-805-73, 2-806-73, 2-807-73; 2-808-73, 2-809-73, 2-810-73, 2-811-73; 2-812-73, 2-813-73, 2-814-73, 2-815-73; 2-816-73, 2-817-73, 2-818-73, 2-819-73; 2-820-73, 2-821-73, 2-822-73, 2-823-73; 2-824-73, 2-825-73, 2-826-73, 2-827-73; 2-828-73, 2-829-73, 2-830-73, 2-831-73; 2-832-73, 2-833-73, 2-834-73, 2-835-73; 2-836-73, 2-837-73, 2-838-73, 2-839-73; 2-840-73, 2-841-73, 2-842-73, 2-843-73; 2-844-73, 2-845-73, 2-846-73, 2-847-73; 2-848-73, 2-849-73, 2-850-73, 2-851-73; 2-852-73, 2-853-73, 2-854-73, 2-855-73; 2-856-73, 2-857-73, 2-858-73, 2-859-73; 2-860-73, 2-861-73, 2-862-73, 2-863-73; 2-864-73, 2-865-73, 2-866-73, 2-867-73; 2-868-73, 2-869-73, 2-870-73, 2-871-73; 2-872-73, 2-873-73, 2-874-73, 2-875-73; 2-876-73, 2-877-73, 2-878-73, 2-879-73; 2-880-73, 2-881-73, 2-882-73, 2-883-73; 2-884-73, 2-885-73, 2-886-73, 2-887-73; 2-888-73, 2-889-73, 2-890-73, 2-891-73; 2-892-73, 2-893-73, 2-894-73, 2-895-73; 2-896-73, 2-897-73, 2-898-73, 2-899-73; 2-900-73, 2-901-73, 2-902-73, 2-903-73; 2-904-73, 2-905-73, 2-906-73, 2-907-73; 2-908-73, 2-909-73, 2-910-73, 2-911-73; 2-912-73, 2-913-73, 2-914-73, 2-915-73; 2-916-73, 2-917-73, 2-918-73, 2-919-73; 2-920-73, 2-921-73, 2-922-73, 2-923-73; 2-924-73, 2-925-73, 2-926-73, 2-927-73; 2-928-73, 2-929-73, 2-930-73, 2-931-73; 2-932-73, 2-933-73, 2-934-73, 2-935-73; 2-936-73, 2-937-73, 2-938-73, 2-939-73; 2-940-73, 2-941-73, 2-942-73, 2-943-73; 2-944-73, 2-945-73, 2-946-73, 2-947-73; 2-948-73, 2-949-73, 2-950-73, 2-951-73; 2-952-73, 2-953-73, 2-954-73, 2-955-73; 2-956-73, 2-957-73, 2-958-73, 2-959-73; 2-960-73, 2-961-73, 2-962-73, 2-963-73; 2-964-73, 2-965-73, 2-966-73, 2-967-73; 2-968-73, 2-969-73, 2-970-73, 2-971-73; 2-972-73, 2-973-73, 2-974-73, 2-975-73; 2-976-73, 2-977-73, 2-978-73, 2-979-73; 2-980-73, 2-981-73, 2-982-73, 2-983-73; 2-984-73, 2-985-73, 2-986-73, 2-987-73; 2-988-73, 2-989-73, 2-990-73, 2-991-73; 2-992-73, 2-993-73, 2-994-73, 2-995-73; 2-996-73, 2-997-73, 2-998-73, 2-999-73; 2-1000-73, 2-1001-73, 2-1002-73, 2-1003-73; 2-1004-73, 2-1005-73, 2-1006-73, 2-1007-73; 2-1008-73, 2-1009-73, 2-1010-73, 2-1011-73; 2-1012-73, 2-1013-73, 2-1014-73, 2-1015-73; 2-1016-73, 2-1017-73, 2-1018-73, 2-1019-73; 2-1020-73, 2-1021-73, 2-1022-73, 2-1023-73; 2-1024-73, 2-1025-73, 2-1026-73, 2-1027-73; 2-1028-73, 2-1029-73, 2-1030-73, 2-1031-73; 2-1032-73, 2-1033-73, 2-1034-73, 2-1035-73; 2-1036-73, 2-1037-73, 2-1038-73, 2-1039-73; 2-1040-73, 2-1041-73, 2-1042-73, 2-1043-73; 2-1044-73, 2-1045-73, 2-1046-73, 2-1047-73; 2-1048-73, 2-1049-73, 2-1050-73, 2-1051-73; 2-1052-73, 2-1053-73, 2-1054-73, 2-1055-73; 2-1056-73, 2-1057-73, 2-1058-73, 2-1059-73; 2-1060-73, 2-1061-73, 2-1062-73, 2-1063-73; 2-1064-73, 2-1065-73, 2-1066-73, 2-1067-73; 2-1068-73, 2-1069-73, 2-1070-73, 2-1071-73; 2-1072-73, 2-1073-73, 2-1074-73, 2-1075-73; 2-1076-73, 2-1077-73, 2-1078-73, 2-1079-73; 2-1080-73, 2-1081-73, 2-1082-73, 2-1083-73; 2-1084-73, 2-1085-73, 2-1086-73, 2-1087-73; 2-1088-73, 2-1089-73, 2-1090-73, 2-1091-73; 2-1092-73, 2-1093-73, 2-1094-73, 2-1095-73; 2-1096-73, 2-1097-73, 2-1098-73, 2-1099-73; 2-1100-73, 2-1101-73, 2-1102-73, 2-1103-73; 2-1104-73, 2-1105-73, 2-1106-73, 2-1107-73; 2-1108-73, 2-1109-73, 2-1110-73, 2-1111-73; 2-1112-73, 2-1113-73, 2-1114-73, 2-1115-73; 2-1116-73, 2-1117-73, 2-1118-73, 2-1119-73; 2-1120-73, 2-1121-73, 2-1122-73, 2-1123-73; 2-1124-73, 2-1125-73, 2-1126-73, 2-1127-73; 2-1128-73, 2-1129-73, 2-1130-73, 2-1131-73; 2-1132-73, 2-1133-73, 2-1134-73, 2-1135-73; 2-1136-73, 2-1137-73, 2-1138-73, 2-1139-73; 2-1140-73, 2-1141-73, 2-1142-73, 2-1143-73; 2-1144-73, 2-1145-73, 2-1146-73, 2-1147-73; 2-1148-73, 2-1149-73, 2-1150-73, 2-1151-73; 2-1152-73, 2-1153-73, 2-1154-73, 2-1155-73; 2-1156-73, 2-1157-73, 2-1158-73, 2-1159-73; 2-1160-73, 2-1161-73, 2-1162-73, 2-1163-73; 2-1164-73, 2-1165-73, 2-1166-73, 2-1167-73; 2-1168-73, 2-1169-73, 2-1170-73, 2-1171-73; 2-1172-73, 2-1173-73, 2-1174-73, 2-1175-73; 2-1176-73, 2-1177-73, 2-1178-73, 2-1179-73; 2-1180-73, 2-1181-73, 2-1182-73, 2-1183-73; 2-1184-73, 2-1185-73, 2-1186-73, 2-1187-73; 2-1188-73, 2-1189-73, 2-1190-73, 2-1191-73; 2-1192-73, 2-1193-73, 2-1194		

[illegible]